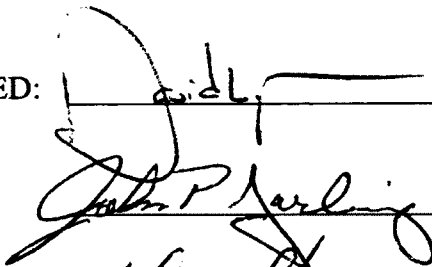# MICRO SCALE ANALYSIS OF FLUID FLOW AND DIFFUSION IN COARSE

GRAINED POROUS MEDIA

By

Walter J. Fourie
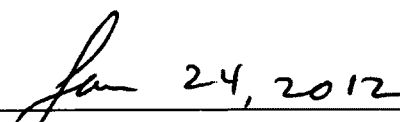
RECOMMENDED: _____

_____

_____

_____

APPROVED: _____
Dean, College of Engineering & Mines
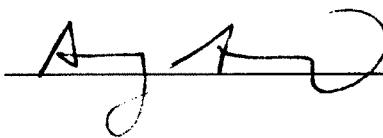
_____
Dean of the Graduate School

_____
Date

MICRO SCALE ANALYSIS OF FLUID FLOW AND DIFFUSION IN COARSE
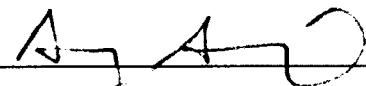
GRAINED POROUS MEDIA

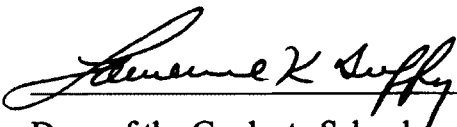A

THESIS

Presented to the Faculty

of the University of Alaska Fairbanks

in Partial Fulfillment of the Requirements

for the Degree of

DOCTOR OF PHILOSOPHY

By

Walter Johannes Fourie, M.Sc.

Fairbanks, Alaska

December 2011

UMI Number: 3528848

UMI

Dissertation Publishing

ProQuest

Abstract

X-ray computed tomography and finite element analysis were used to visualize the internal geometry of porous media and calculate the hydraulic conductivity and the diffusion of a dissolved species through the media. The results were compared to laboratory generated results. The calculated hydraulic conductivity showed good agreement with the laboratory results, over- predicting the laboratory results with only 12.5%. Comparison of the calculated results with the Kozeny-Carman equation showed that the Kozeny-Carman equation over-predicted the laboratory results between 62% and 740% depending on the formulation used. The tortuosity and specific surface area showed the highest correlation in predicting the difference between the Kozeny-Carman equation and the modeling results, while the porosity showed the greatest influence in determining the magnitude of the hydraulic conductivity as calculated by the Kozeny-Carman equation.

The calculation of the diffusion of potassium iodide through ceramic disks and sandstone showed accurate prediction of the concentration in the receiving cell for the length of the experiment (35 days) for one of the ceramic disks and the sandstone. The other ceramic disk showed accurate prediction up to 20 days, after which it deviated. The results from the study indicate that the diffusional tortuosity and the hydrodynamic tortuosity differ in magnitude, and that they can not be used interchangeably, since (1) the ceramic disks showed the closest prediction to the laboratory results when the diffusional tortuosity is used, rather than the hydrodynamic tortuosity, and when it enters the equation to the first power; and (2) the sandstone showed the closest prediction to the laboratory results when the diffusional tortuosity is used, and when it enters the equation to the second power.

Broadly speaking, the results from this study show that the micro scale analysis of porous media allows the accurate calculation of macro scale parameters.

For my Father

Table of Contents

List of Figures

List of Tables

Acknowledgements

I would like thank my advisor, Dave Barnes, and my committee members, John Zarling, Yuri Shur and Doug Goering, for their support during my residence in Alaska, and the years following my departure back to South Africa. Their guidance and input into my thesis were invaluable. Also, I would like to thank Filiep Samyn for his assistance with the statistical analyses presented in this thesis. The skills he taught me in data analysis will forever make me a better researcher than what I was.

Jennifer Benning completed the through-diffusion laboratory experiments and ran the Fortran model that used the parameters generated through the X-ray Computed Tomography and the Finite Element Analysis. She was instrumental in the formation of the ideas that led to the work presented in this thesis.

My mother sent me an email every single day of my sojourn in Alaska, and my dad made my Ph.D. pains seem trivial as he related his struggle. I owe both of you a great deal for your support.

This work was supported with funding from the Inland Northwest Research Alliance, the Institute of Northern Engineering, and the Water and Environmental Research Center. My studies would never have been completed if it was not for ample financial support from my father's bank account. My sincerest thanks.

And lastly, I would like to thank Alaska, the Great Land. I arrived at your borders a boy, but I left as a man.

Nomenclature

A	=	Area [m^2]
A_t	=	Cross sectional area of the burette [cm^2]
A_c	=	Cross sectional area of the soil sample [cm^2]
δ	=	Constrictivity [ ]
d_{10}	=	10 percent passing diameter [mm]
d_{50}	=	50 percent passing diameter [mm]
C	=	Concentration [kg/m^3]
C_o	=	Concentration at the boundary [kg/m^3]
C_b	=	Concentration of the bulk [kg/m^3]
D_i	=	Intrinsic diffusion coefficient [m^2/s]
D_m	=	Molecular diffusion coefficient [m^2/s]
F	=	Volume force [N/m^3]
η	=	Dynamic viscosity [Pa.s]
h	=	Head [m]
K	=	Hydraulic conductivity [cm/s]
k	=	Permeability [m^{-2}]
k_c	=	Mass transfer coefficient [m/s]
l	=	Length [m]
L	=	Length [m]
M_s	=	Specific surface area base on the solid volume [m^{-1}]
N	=	Mass flux [kg/m^2.s]
Q	=	Flow [m^3/s]
p	=	Pressure [Pa]
p_o	=	Pressure at the boundary [Pa]
ρ	=	Density [kg/m^3]
R	=	Reaction Rate [kg/m^3.s]
τ_d	=	Diffusive Tortuosity [ ]

τ_e = Electrical Tortuosity [ ]

τ_h = Hydrodynamic Tortuosity [ ]

ϕ_e = Effective Porosity [ ]

u = Velocity field [m/s]

1 Introduction

Several of the commonly used equations in general science are based on assumptions. These assumptions include constants that group together properties of physical, chemical or biological systems that can not be completely described. For example, the basis on which groundwater flow is calculated is derived from a 150-year old equation: Darcy's Law. Darcy's Law is essentially a phenomological law, in that Darcy observed the flow phenomenon through packed sand columns and then constructed his equations to fit those observations. His equation has three parts, the flux, which is measured, the gradient that is measured, and then the permeability, which was fitted to the observations. The equation is therefore empirical in nature. Scientists have accepted the *truth* of these equations, since they work well, and usually show to have some underpinnings of sound scientific principles. In the case of Darcy's Law, it was shown by Bear (1972) and later more rigorously by Ene (1990), that Darcy's Law can be derived from the Navier-Stokes equations. What has not been shown, is that when the flow through a porous medium is calculated by the Navier-Stokes equations, the result is the same as if the experiment was conducted in the laboratory. The same analogy is true for the diffusive flux of a species through a porous medium.

When Fick's Laws are applied to describe the diffusive flux of molecules across a porous medium, an intrinsic diffusion coefficient is introduced to account for the effects of the retardation of the species. The intrinsic diffusion coefficient takes into account the properties of the diffusing molecule, the solvent, and the porous medium. The complexity and inherent heterogeneity in the configuration of the pore space necessitates measurement of the intrinsic diffusion coefficient as a bulk parameter via laboratory experiments, the most common of which is known as the through-diffusion test (Garrels et al., 1949). The influence of the porous media's properties on diffusion is then assessed through comparison of the measured intrinsic diffusion coefficient to the known molecular free-water diffusion coefficient; a formation factor or geometric factor that

quantifies the ratio of these coefficients for a particular medium is often reported (Bradbury & Green, 1985; Skagius & Neretnieks, 1986).

Various aspects of the pore structure's nature, such as its tortuosity, constrictivity, and connectivity, will contribute to the formation factor, however, the typical laboratory test does not allow any distinction of these properties and thus there is no way to assess the relative importance of each. The influence of these porous media properties on the intrinsic diffusion coefficient and indeed their fundamental definitions, have been extensively studied, but there are far-ranging opinions as to the relationship between the different porous media properties themselves and the aforementioned properties and the intrinsic diffusion coefficient (e.g. Saripalli et al., 2002; Vervoort & Cattle, 2003). Some of this difficulty may arise from the historic derivation of the equations under certain conditions, such as gas-phase diffusion in an unconsolidated porous media, and the subsequent extrapolation of the derived relationships to different conditions, such as aqueous-phase diffusion in unconsolidated media. The applicability of such a translation is unclear. The lack of a clear definition has also been complicated by technological limitations that did not allow the analysis of a complicated pore network structure in three dimensions (Van Brakel & Heertjes, 1974).

The pore scale analysis of porous media to allow the calculation of the parameters that contribute to the samples' hydraulic conductivity and the diffusive ability, can now be done with a combination of x-ray computed tomography and finite element analysis. Each of these techniques, by itself, is not novel, but recent advances have allowed the combination of these techniques to facilitate pore scale analysis (Elliot et al., 2010). The properties of the porous medium, given an assumption of homogeneity, are intrinsic values that are independent of scale, and therefore the rapid determination of these parameters through computed tomography can be directly applied to volumes on a larger scale.

The objectives of this thesis are to

1. Quantify the relative influence of pore scale measured porous media properties on the lumped parameter, the hydraulic conductivity, found in Darcy's Law and the formation factor, found in Fick's Law.

2. Assess the appropriate use of empirical derivations of the hydraulic conductivity and formation factor when compared to laboratory generated results.

Improved understanding of the role of the pore-scale structure and the associated parameters: porosity, specific surface area, tortuosity, constrictivity, and connectivity, is beneficial to a wide range of applications, including: modeling the fate and transport of aqueous-phase contaminants through rock, sands, gravels, concrete, or brick; modeling the vapor-phase diffusive transport of pollutants through building materials; improving air quality by reducing building product emissions using barrier layers; and the improved understanding of the effects of fracking in the search of oil and gas.

2 Literature Survey

2.1 X-Ray Computed Tomography

2.1.1 Advent of X-ray CT

X-ray Computed Tomography had its origins in the medical sciences. G. Hounsfield, from EMI Ltd. in England developed the first commercial x-ray computed tomography system (Hounsfield, 1973), at which point it was known as Computed Assisted Tomography (and hence the colloquialism CAT-scan, was born). Although the system was designed and operational in the 70s, it took some 10 years before quantitative analyses were published (Rüegsegger et al., 1983; McBroom, et al., 1985). In complement to the non-destructive visualization of internal objects, mostly bone, the mathematics to describe the internal features also evolved (Cowin & Mehrabadi, 1989; Odgaard, 1997; Ulrich et al., 1999; Chiang et al., 2006) and has culminated in predictive modeling based on geometry (Shefelbine et al., 2005; Takada et al., 2006). Today, computed tomography finds ubiquitous application in hospitals and research facilities alike, for both qualitative and quantitative examinations.

2.1.2 Geosciences

In 1982, Petrovic et al. determined the bulk density of soils and in 1983 Hainsworth and Aylmore determined the moisture content of soils through x-ray computed tomography. Both of these studies looked at bulk (or macro scale) parameters. In the early years of investigations in the geosciences, the resolution of CAT scanners were in the order of millimeters. Hence, the object being examined could not be characterized by features of its internal objects, but only by a crude homogenization assumption of its interior. This phenomenon is called the *partial volume* effect. In Hainsworth and Aylmore's work, they found the moisture content by apportioning the increased adsorption of x-rays to the density difference between air and water. Wang et al. (1984) used the same method to determine oil saturations in rock. Imaging of specific internal objects was possible, as long as these objects were in the same order of magnitude as the scanning resolution. For

example, Warner et al. (1989) imaged macro pores in soils and Joschko et al. (1993) imaged earth worm burrow systems. It is however mathematically possible to image objects smaller than the native scanner resolution by using subtraction techniques (Withjack, 1988) and to image more than two phases (Wellington & Vinegar, 1987). However, these methods find limited application (Goldstein et al., 2007), due to the advent of micro tomography.

In 1999 Rosenberg et al. developed a method for the micro tomography of rocks. They imaged sandstone samples in sub 10 μm resolution, and also experimented with the use x-ray absorbing tracers (KBr). Carlson et al. (1999) employed a 420 kV scanner to characterize large rock specimens down to 20 micron resolution and Landis et al. (2000), used x-ray CT to investigate the fracturing of mortar. Landis et al. (1999) also investigated pore networks, and not only used visual data from the scan, but interpreted the data mathematically to find areas, volumes and connectivity. They did however indicate that the discretization caused by the imaging influenced the quality of the data.

2.2 Pore Scale Measurements

In the previous three decades, pore scale visualization and measurements were chiefly limited to the method of serial sectioning (DeHoff et al., 1972; Macdonald et al., 1986; Moran, 1994; Vogel, 1997). In this method, the pore space of the sample is infiltrated with a resin, and then the whole sample is ground away section by section and photographed. The process is very labor intensive and suffers from mechanical obstacles such as positioning, polishing and etching, and then the subsequent hurdle of digitization. Other methods such as stereology (Ringrose-Voase, 1996) and infiltration with dyes (Mooney & Morris, 2004) have also been used.

The limitation of Computed Tomography in the quantification of pore scale measurements is twofold: (1) Resolution limit of the instrument versus the pore diameter, and (2) Strength of the instrument (kV) versus the size and density of the sample.

These limitations have resulted in the majority of publications that address "pore scale" measurements, only do so from a macro perspective. Pierret et al. (2002) analyzed macro pores (isotropic analysis at 400 x 400μm), Gherboudj et al. (2007) studied inclusion in river ice (anisotropic analysis at 100 x 500μm) and Ketcham & Iturrino (2005) looked at effective porosities (isotropic analysis at 57.8 x 57.8μm). A common problem in the studies mentioned above is the *partial volume effect*. Figure 2.1 shows two theoretical particles separated by pore space. In (a) are the two particles as they are in real life, separated by 20 "units". If a scanner is used that can only scan at 10 "unit" resolution, the particles can still be seen to have space between them. However, as shown in (c), when a scanner is used that can only resolve at a 20 "unit" resolution, the space between the particles now has a grey value. This is caused by the averaging of black and white pixel values between the particles. At 100 "unit" resolution all semblance of spherical particles and the space between them are lost.

(a) Actual particles

(b) Particles pixelated x10

(c) Particles pixelated x20

(d) Particles pixelated x100
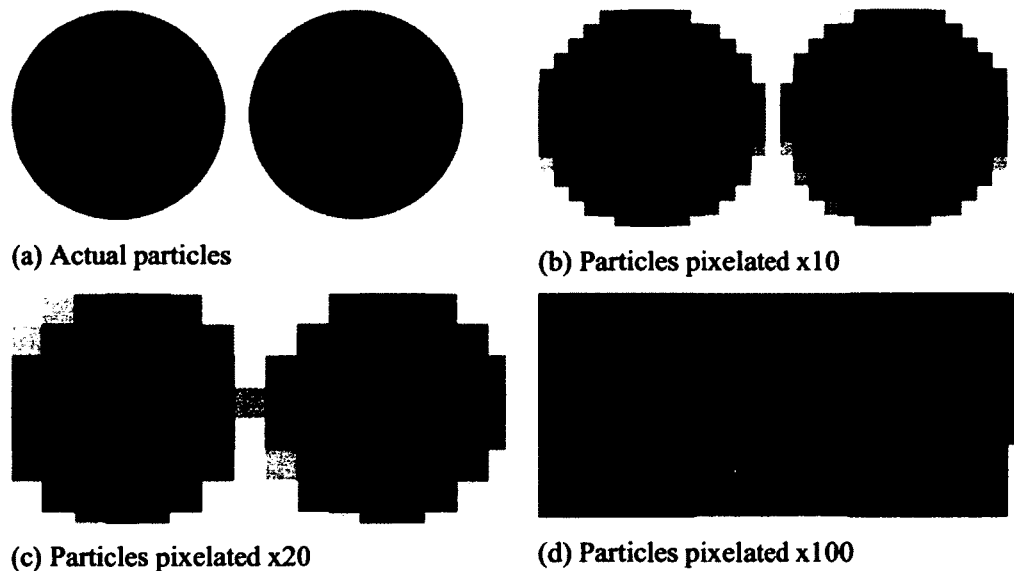
Figure 2.1: Example of how scanner resolution dictates the quality of the final analysis through the partial volume effect.

To extrapolate, if the scanner has a minimum resolution of e.g. 20μm, but the features in the pore space are 20μm in size and less, the scanner will not be able to resolve these features, or will only be able to resolve them partially. From a statistical point of view, the following analysis can be made. If the scanner has a resolution of 20μm, and the pore space has a mean of 100μm and a standard deviation of 40μm, the scanner will not be able to resolve around 2.275% of the pore space. This analysis is shown graphically in Figure 2.2, and assumes a normal distribution of the pore space.
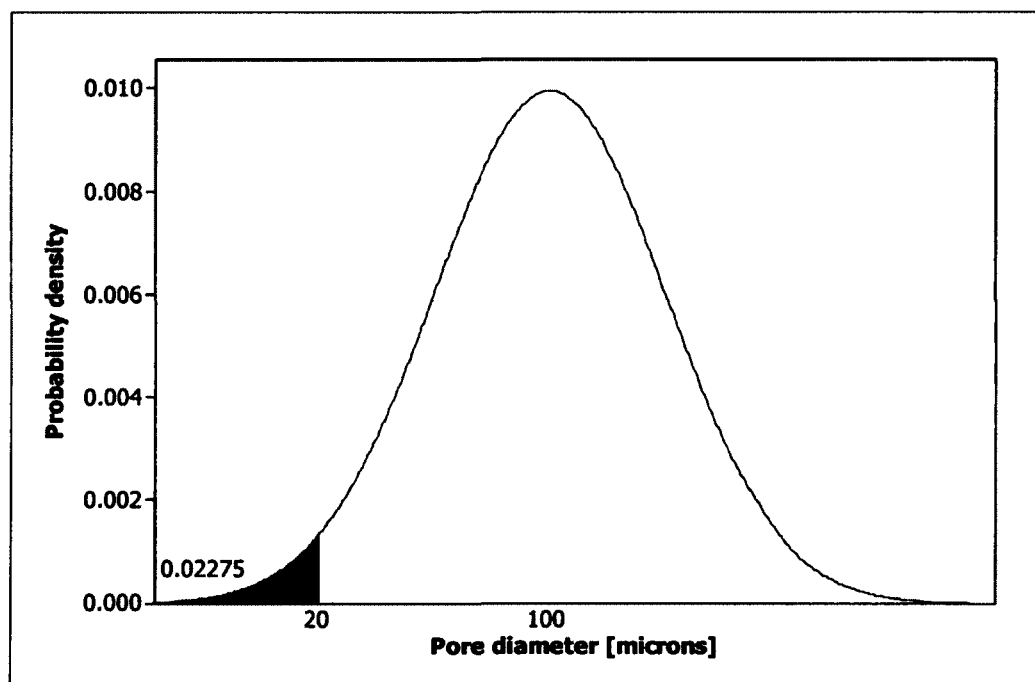
Figure 2.2: Probability density function showing the hypothetical intersection of the scanner resolution and the pore size distribution.

Current micro tomographic instruments have a minimum resolution of around 800nm. Thus, to achieve an acceptable error of around 1%, the mean pore diameter will have to be 5μm. This is illustrated in Figure 2.3.
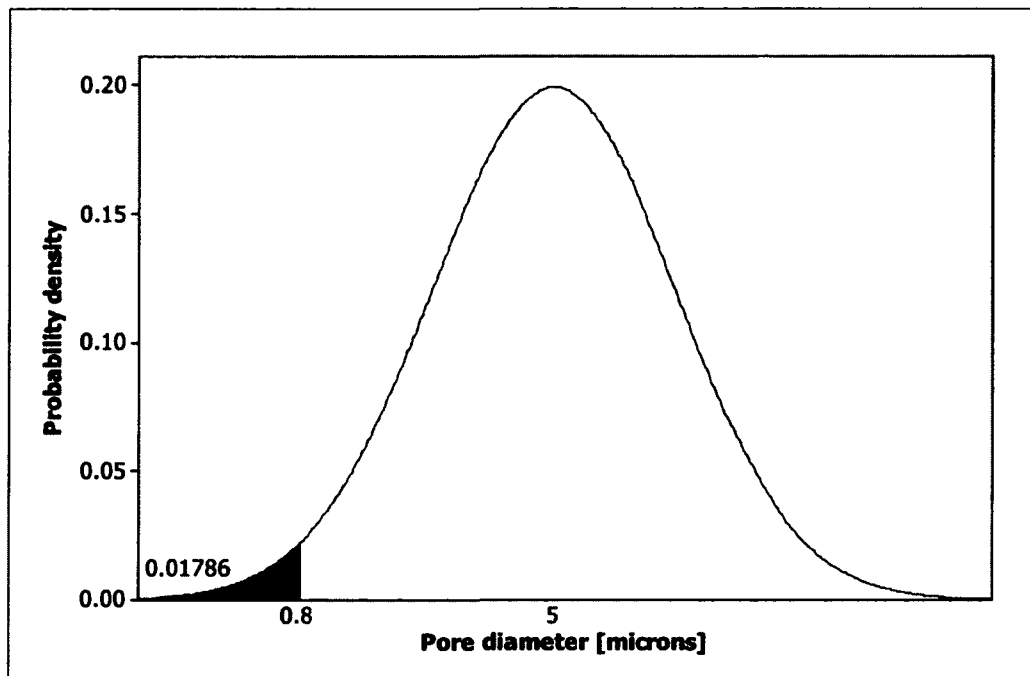
Figure 2.3: Probability density function illustrating the limitation of current technology with regards to the resolving small pore spaces.

Rosenberg et al. (1999) noted that the limitation of micro tomography in the partial volume effect is just as valid now as it was when medical scanners were first applied to the geosciences. If we assume that clayey soil has a mean pore size of 0.5 μm (Diamond, 1970), a standard deviation of 0.2 μm and it is necessary to resolve at least 95% of the pore space, it would require a scanner which can resolve down to 0.171 μm (Figure 2.4).
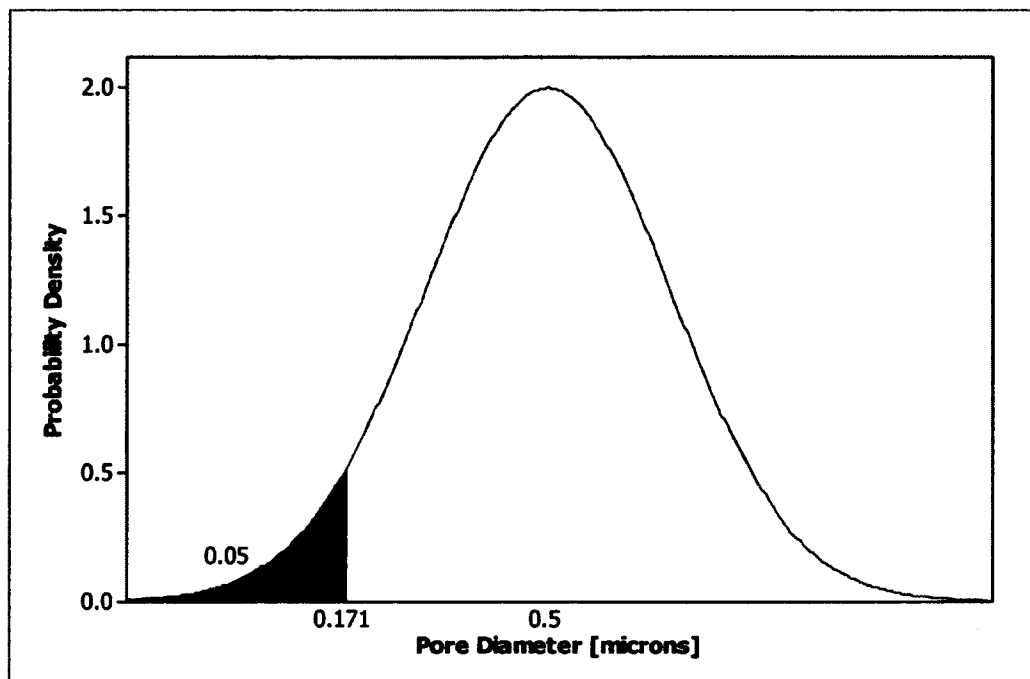
Figure 2.4: Probability density function showing the resolution necessary to resolve 95% of a clay soil.

The calculated minimum resolution of a scanner is an absolutely best case scenario, and in practice, especially with heterogeneous samples, the resolution needs to be one order of magnitude higher than the minimum calculated. As an example, Figure 2.5 shows a cross section of a soil sample taken from Casey Station in Antarctica, and Figure 2.6 shows the particle size distribution.
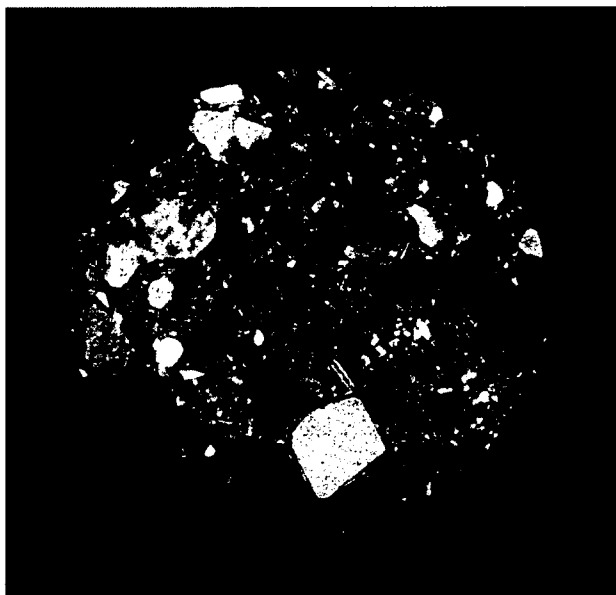
Figure 2.5: Cross section of heterogeneous soil from Case Station in Antarctica.
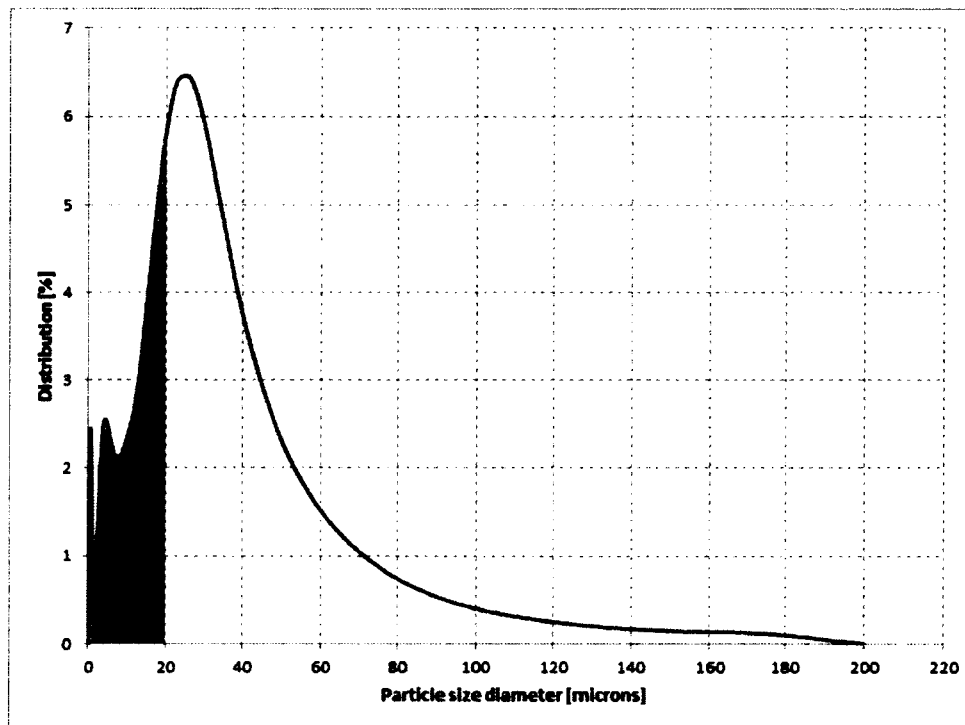
Figure 2.6: Particle size distribution of heterogeneous soil from Casey Station in Antarctic. Area shaded in red is 25% of cumulative size distribution.

For a scanner with a two micron resolution, near 99% of the particles can be resolved. However, due to the heterogeneity of the sample, an additional order of magnitude in resolution is required to accurately resolve each individual particle. Figure 2.7 explains this concept. Four particles are shown, two particles with 100 "unit" diameter and two particles with a 10 "unit" diameter. Three of the particles are separated by a 10 "unit" space, while the 4th is further away. If a scan is taken of the particles with a scanner that can resolve at a 10 "unit" resolution, the scan in Figure 2.7 (b) would result. The 100 "unit" particles can easily be resolved. The shape of the separated particle may be obscure, but the scan does show that *something* is there. However, the small 10 "unit" particle next to the 100 "unit" particle presents a problem. Is the small particle a particle on its own, or is attached to the large particle? The scan can not determine that as the

scan was done at the same order of magnitude as the small particle size. Thus, as a rule of thumb, in heterogeneous samples an additional order of magnitude in the scanning resolution is required to resolve objects.

(a) Actual particles   (b) Particles pixelated at x10
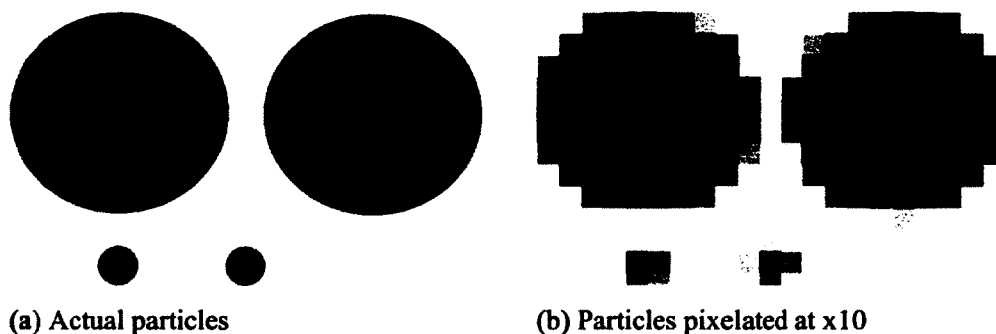
Figure 2.7: Particles showing the effect of heterogeneity on scanning resolution.

Therefore, in the case of the Case soil, it is as if the scanner could only scan to 20 micron resolution, which would only be able to resolve 75% of the sample.

This limitation in practical resolution and its effect on the choice of sample in this study is further explained in Section 3.1.2.

2.2.1 Hydraulic Conductivity

In 1856 Henry Darcy conducted research on fluid flow through sand columns and his results became the primary equations by which we calculate groundwater flow today (Darcy, 1856; Charbenau, 1990; Fetter, 2001; Fitts, 2002). Equation (2.1) shows Darcy's Law.

$$Q = KA\frac{dh}{dl} \qquad (2.1)$$

with Q representing the volumetric flow rate [m^3/s], K the hydraulic conductivity [m/s], A the cross sectional area [m^2], h the pressure head difference [m] and l [m] the sample

length. Darcy's Law has been shown to have an analytic foundation, in that it can be derived from the Navier-Stokes equations (Bear, 1972; Ene, 1990). Thus, even at the pore scale, it should be possible to define groundwater flow through the Navier-Stokes equations. To prove that the prediction of flow by Darcy's Law is comparable to the rigorous calculation of flow by the Navier-Stokes equation, it is necessary to apply the Navier-Stokes equation to a true-to-life three dimensional space. In hydrology that three dimensional space is the pore space in a soil through which the groundwater flows.

In Darcy's Law, the hydraulic conductivity is in essence an empirical parameter that relates the pressure drop in a soil to the flow rate through it. The magnitude of the hydraulic conductivity is influenced by numerous parameters e.g. the grain size distribution, particle shape and porosity, and numerous models have been developed to predict the hydraulic conductivity based on these parameters (Agyare et al., 2007; Carrier, 2003; Chakraborty et al., 2006; Chapuis, 2004; Cronican & Gribb, 2004; Mbonimpa et al., 2002; Millington & Quirk, 1961; Regalado & Muñoz-Carpena, 2004; Sperry & Peirce 1995). These models are predictive in nature in that they measure the related parameters, and predict the hydraulic conductivity. The current study directly calculates the hydraulic conductivity from flow through porous media.

2.2.2 Diffusion

In the prediction of the diffusion of a species through a consolidated porous medium, the intrinsic diffusion coefficient is dependent on the molecular, or free-water, diffusion coefficient of that species and the intrinsic properties of the porous medium. The fundamental definitions and relative influence of these properties on the intrinsic diffusion coefficient have been studied for the last 80 years, resulting in varied opinions as to their values and correct applications. In 1955, Wheeler proposed that the intrinsic diffusion coefficient (D_i) is related to the molecular diffusion coefficient (D_m) by the ratio of effective porosity (φ_e) to tortuosity squared (τ_d). Note that in this paper, the subscripts for the tortuosity will distinguish between the diffusive tortuosity (τ_d) and hydrodynamic

tortuosity (τ_h) to avoid confusion. The diffusive tortuosity is defined when the controlling mechanism for transport of a molecule is diffusion and the hydrodynamic tortuosity is defined when transport is controlled by advection.

$$D_i = D_m \frac{\phi_e}{\tau_d^2}$$
(2.2)

The tortuosity is defined as the ratio of the effective length that a particle has to travel through the porous medium, L_e, to the length of the porous medium, L:

$$\tau_d = \frac{L_e}{L}$$
(2.3)

Van Brakel & Heertjes (1974) expanded the description of the relationship between the porous media properties (the formation factor) by including the constrictivity, δ, into the equation, where the constrictivity is empirically defined on the basis of the ratio between the largest and the smallest pore size (other references base the empirically derived constrictivity on the basis of the molecule diameter to pore size ratio). This equation was derived for gas diffusing through an unconsolidated porous medium, but it is frequently referenced for work in aqueous phase diffusion in consolidated porous media (e.g. Bradbury & Green, 1985). In particular, the derivation of the tortuosity entering the relationship to the second power was based on the geometry of a homogeneous unconsolidated media.

$$D_i = D_m \frac{\phi_e \delta}{\tau_d^2}$$
(2.4)

This definition of the formation factor is in contrast to that proposed by Satterfield (1970), where the tortuosity enters the equation to the first power, and the effect of constrictivity is lumped with the tortuosity:

$$D_i = D_m \frac{\phi_e}{\tau_d} \tag{2.5}$$

Some current textbooks perpetuate this equation, though they acknowledge the difference between tortuosity and constrictivity, δ, (e.g. Fogler, 2005):

$$D_i = D_m \frac{\phi_e \delta}{\tau_d} \tag{2.6}$$

The fact that the tortuosity of a porous medium can slow the movement of a fluid or species through the medium was first acknowledged by Kozeny in 1927. Kozeny related the flow through a porous medium to the pressure drop, as a function of the porous medium's properties with the tortuosity entering the equation to the first power. Carman (1937) remarked that this interpretation is incorrect, given Kozeny's assumptions, and that the tortuosity should enter the equation squared. He derived his equation for unconsolidated media. From there, the well known Kozeny-Carman equation, which is still used ubiquitously today to estimate a porous medium's permeability, k (e.g. Bear, 1972) is:

$$k = c_o \frac{\phi_e^3}{\tau_h^2 M_s^2 (1 - \phi_e)^2} \tag{2.7}$$

where τ_h is the hydrodynamic tortuosity, M_s is the specific surface area and c_o is a shape factor. Epstein (1989) showed through derivation that when these relationships are based on the capillary tube model, the tortuosity, whether it is τ_h or τ_d, should enter the equation squared. The squared term is generated by the increased path length as well as the

increased interstitial axial velocity/diffusional flux. This was contradicted with work done by Winsauer et al. (1952), where he showed through experimentation that

$$D_i = D_m \frac{\phi_e}{\tau_e^{1.67}} \tag{2.8}$$

where τ_e is the electrical tortuosity. The electrical tortuosity is the path taken by electrons as it passes through a saturated porous medium. Winsauer et al.'s work was conducted on consolidated porous media saturated in brine. In the literature, little distinction is made between the different tortuosities. For example Saripalli et al. (2002), when examining the intrinsic diffusion coefficient, references Carman (1956) for Equation (2.2), even though Carman's work is based on the hydrodynamic tortuosity. The difference between the tortuosities, and their possible relationship, is explained from a theoretical point of view by Clennell (1997). Clennell notes that the fundamental equations of diffusion and hydrodynamic flow are different in form. In hydrodynamic flow viscous drag causes the flow to decrease near the pore walls, while with the diffusional Laplace equation, there is no gradient imposed by the pore walls as a boundary. Thus the tortuous path of a fluid particle driven by a pressure difference, and that of a dissolved species, can be expected to be different.

In summary, there has been great variability and hence, uncertainty, as to how the tortuosity and other pore scale parameters are defined and how they should be included in the calculation of the intrinsic diffusion coefficient and the hydraulic conductivity. The experimental justification of much of the foregone work in diffusion has been based on empirical relationships, mostly because the inherent complexity of pore scale mechanisms and measurements in both diffusion and advection has been beyond the technological capability of science.

3 Experimental Procedure

3.1 X-Ray Computed Tomography

3.1.1 Image Acquisition

In x-ray computed tomography the internal structure of an object is imaged non-destructively. The object being studied is placed in front of an x-ray source, and successive *shadow projections* are recorded as the object is rotated. This procedure is schematically shown in Figure 3.1. The x-ray source emits the x-rays for a pre-determined amount of time, and the intensity of the x-rays passing through the object is recorded by the detector and digitized. The detector, an x-ray CCD camera, records the x-ray absorption isotropically with pixel sizes from 0.9 – 35 μm. The recorded intensity is a function of the physical and chemical characteristics of the object being examined, and can also be modified by placing x-ray absorbing filters in front of the object. Such filters are particularly necessary when examining high density materials. In such a case the low energy x-rays are preferentially absorbed by the material surface and the high energy x-ray pass through the sample unimpeded. This procedure reduces the amount of information that can be gleaned from the study. However, with the addition of a filter, part of the x-ray spectrum is removed, reducing the amount of *beam hardening* (see Section 3.1.4.3), but also increasing the acquisition time as the exposure time needs to be increased to compensate for the decreased amount of detectable photons.
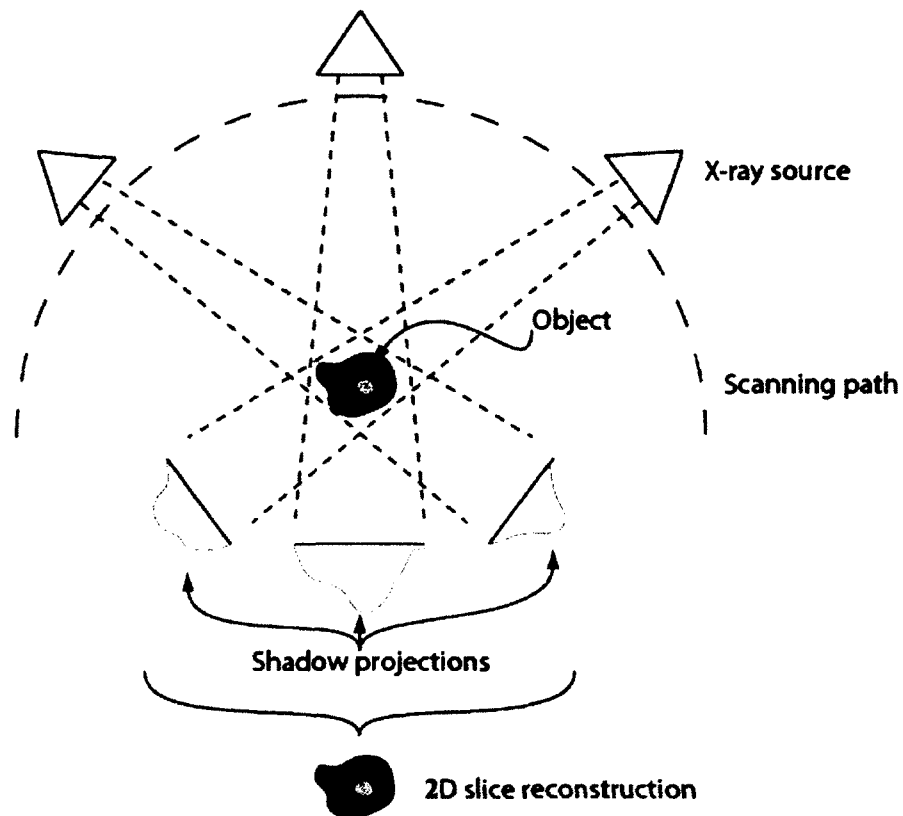
Figure 3.1: An object is rotated and successive shadow projections are captured in order to produce a three dimensional reconstruction.

3.1.2   Material Selection

3.1.2.1   Size

The size of the object being examined is an important parameter in x-ray computed tomography. From an acquisition perspective, the object being examined should be entirely within the field of view, and in the case of this study, the field of view should include the entire *Region of Interest*. A general rule of thumb is also that the scanning resolution should be one order of magnitude higher than the feature of the object to be resolved. For example, if it is necessary to detect pore space inside a sample that is

approximately 20 μm in diameter, the scanning resolution should about 2 μm. Since the field of view is (for the SkyScan 1172), at its highest magnification, 4000 pixels across, the sample can only be 8 mm wide. (2 μm x 4000 = 8 mm). This limits the size of the particles used, as it is necessary to obtain a *Representative Elementary Volume* in the scan. For the purpose of the hydraulic conductivity test it was found that particles with a mean diameter between 0.5 and 1.5 mm would be suitable for scanning. If smaller particles were used, the particle size distribution has a tail end that can not be adequately resolved. These particles were also chosen for possible future work in the examination of pendular rings in unsaturated media. For consolidated media the mean pore diameter should be above 20 μm, as the scanning resolution was kept to above 2 μm.

3.1.2.2 X-ray Absorption

The material's absorption of x-rays also plays an important role in determining if the material will be suitable for the experiment. Several unconsolidated media were tested, including glass, polymethylmethacrylate (PMMA), polystyrene, quartz sand, mullite, zeolite, activated carbon and zirconium. All these particles were available in an appropriate mean diameter. The consolidated media tested included natural sand stone and sintered aluminum oxide porous disks.

In testing of the unconsolidated media it became evident that the vibration of the scanner translated to the particles, and since there is no cohesion to hold them together, the particles vibrated independently and resulted in poor reconstructions. Figure 3.2 shows a reconstruction of dry sand particles. The vibration of the particles is evident.
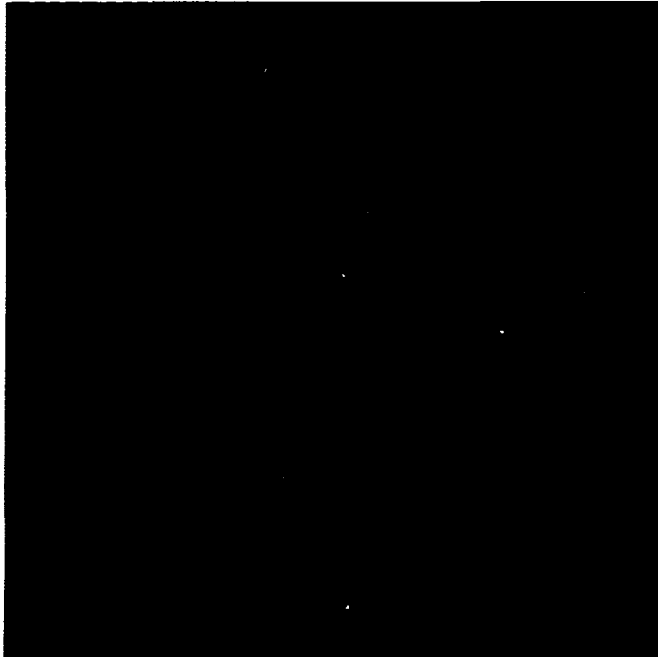
Figure 3.2: The dry sand particles vibrate as there is no cohesion to bind them together. The vibration can be seen as shadow images around the particles borders, making the boundaries not distinct.

The solution to this was to introduce water into the sample. The moisture had to be present in residual amounts, so that the forces of the pendular rings hold the particles together. If too much water is added and the particles are completely surrounded, there are no forces keeping them together, and the particles would once again be able to vibrate. However, the addition of water poses a new problem, as an additional phase is introduced. Figure 3.3 shows the reconstructions of PMMA and sand with residual moisture present.
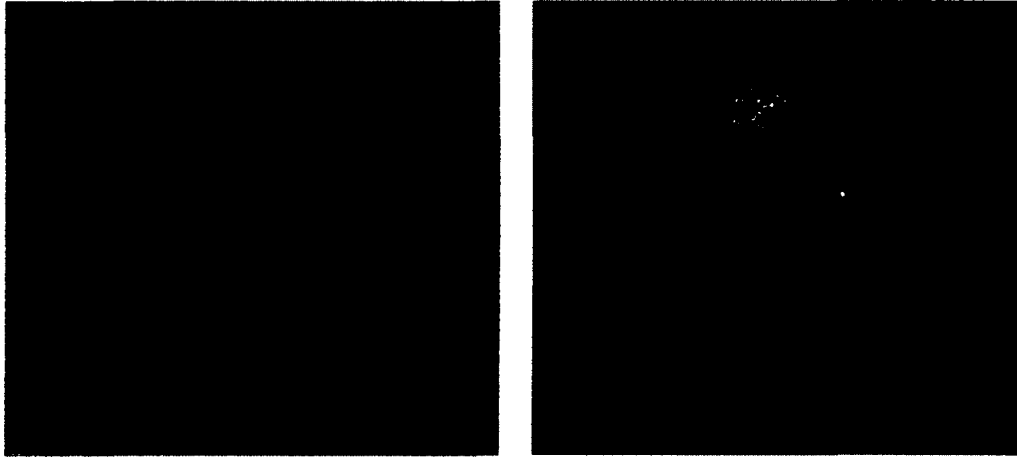
Figure 3.3: Reconstructions of PMMA and sand with residual amounts of moisture present. In the spherical PMMA reconstruction the residual amounts of water are represented by the blue shaded area, and in the sand reconstruction the water is shown by the bright orange areas between the blue sand particles.

In both cases there is a clear distinction between the three phases, solid, air and water. The difference is the order that these three phases absorb the x rays. In the case of the PMMA, the water absorbs the most x-rays, then the PMMA and lastly the air. In the case of the sand, the sand absorbs the most, then the water and lastly the air. This poses a problem with segmentation. In the case of the PMMA, it is not a straight forward procedure to extract the pore space (the air plus the water), since the PMMA has an absorption band that lays in between these two. Figure 3.4 further explains this problem.
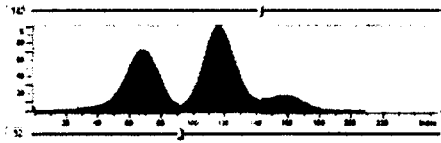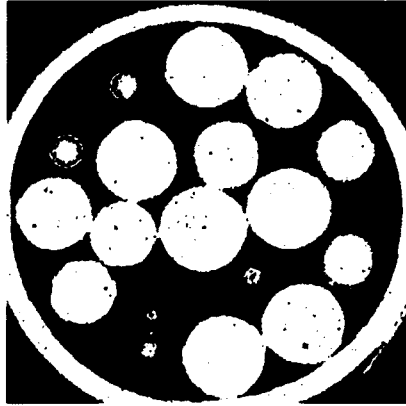
(a) PMMA reconstruction with PMMA highlighted
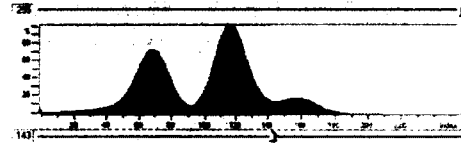
(b) PMMA reconstruction with water highlighted
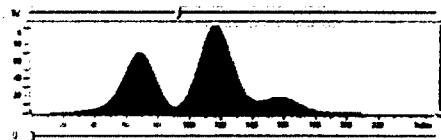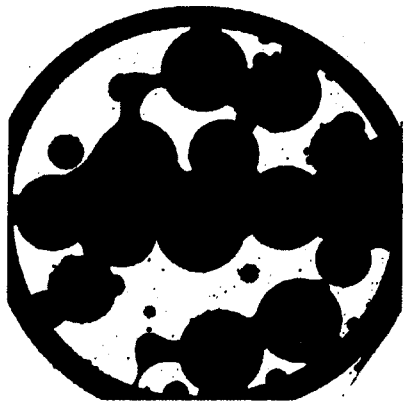
(c) PMMA reconstruction with air highlighted
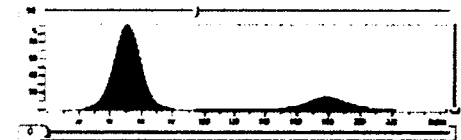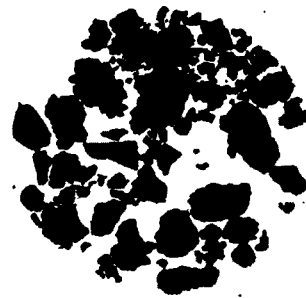
(d) Sand reconstruction with pore space highlighted

Figure 3.4: Reconstructions and histograms of PMMA and sand with residual water.

In Figure 3.4 (a) the reconstruction of the PMMA particles are shown together with the histogram showing the distribution of the grey values in the image. Note that the histogram has three peaks, one each for the air, water and PMMA. Figure 3.4 (b) and (c) show the reconstruction of the water and the air. Note that the adsorption of the water lies to the right of the PMMA adsorption and the air lies to the left. The pore space is comprised of the combination of the air and water, and because they are separated by the adsorption band of the PMMA, there is no easy way to combine the two to get a reconstruction of the entire pore space. In contrast, Figure 3.4 (d) shows the reconstruction of the air and sand, with the air highlighted. The histogram has only two peaks, one for the air and water, and one for the sand. Thus it is a lot easier to create a reconstruction of the pore space.

Another problem is that the PMMA has a density close to water (~1.2 g/cm^3) and exhibits beam hardening on the edges of the particles (see Section 3.1.4.3), which, when reconstructed, shows the same absorption as the water. This is illustrated in Figure 3.5. When a three dimensional model is reconstructed from the image on the right in Figure 3.5, the edges of the pendular water will present themselves as part of the PMMA particles, which will obscure the true particles.

Figure 3.5: Reconstruction of PMMA particles with moisture present. The beam hardening at the edges of the particles and pendular rings, and noise inside the particles, show the same absorption strength as the water and renders the reconstruction useless from a computational point of view.

On the other hand, the sand particles have a large enough difference in adsorption from the water not to exhibit this problem. It is however preferable to have spherical particles from a purely geometry complexity point of view. Mullite and zirconium are grinding aids that are more or less spherical. The zirconium is very dense and was not useable, but the mullite showed promise. Very dense materials absorb all the x-rays and causes excessive artefacts and shadow images. The shadow projection and reconstruction of mullite particles with water is shown in Figure 3.6. The high absorption of the mullite did however cause phantom images that obscured the pendular rings.

Figure 3.6: Shadow projection and reconstruction of mullite and residual water.
The pendular ring is visible in the shadow projection, but in the reconstruction the
phantom image between the two mullite particles obscures the pendular ring.

It was deemed more important to have high quality reconstructions than simple
geometries and therefore it was decided to use the sand in all the unconsolidated media
experiments. With regards to the consolidated media, the sandstone and aluminum oxide
disks showed very good contrast with air and no other alternatives were examined. It is
also important that the container for the sample adsorbs as little as possible of the x-rays.
Thin-walled plastic tubes worked very well, as well as clear adhesive tape wrapped
around the sample. This stabilized the sample very well to keep it in one position during
the scan.

3.1.3 Operating Parameters

The operating parameters for the x-ray scanner include the camera pixel size, the object
stage position and the filter being used. These three parameters are linked through the
image resolution that can be obtained and the exposure time. The interaction matrix for
these parameters is shown in Table 3.1. Each of these parameters will be discussed in
detail in the following sections.

Table 3.1: Default camera exposure matrix.

Camera Position	Pixel Size	Camera Exposure [ms]		
		No Filter	0.5mm Al	Al + Cu
far	small	1767	4712	7068
far	medium	590	1475	2360
far	large	79	316	1264
middle	small	1178	4123	5301
middle	medium	295	885	1475
middle	large	79	316	474
near	small	1178	1767	5301
near	medium	147	2950	2950
near	large	69	158	316

The image resolution that can be obtained depend on the position of the camera, and the camera pixel size selected.

3.1.3.1 Camera Pixel Size

The 10MP camera in the SkyScan 1172 is capable of obtaining an image of 4000 x 2300 (4k) pixels. When 2 x 2 pixels are binned together (an average value for the 4 pixels are taken), the exposure time required decreases, but so does the image resolution that can be obtained. The camera then records a shadow image of 2000 x 1150 (2k). When 4 x 4 pixels are binned together, the image resolution decreases to 1000 x 575 (1k). Transmission profiles of the three different setting are shown in Figure 3.7, together with reconstructions in Figure 3.8. In the transmission profile the absorption of the shadow image is shown by the orange line running from left to right. To get adequate contrast in the final reconstruction, it is preferred to have maximum absorption of 80% and a

minimum absorption of 20%. The smaller the difference between the minimum and the maximum, the more difficult it will be to segment the reconstructed 2D image.

Porous medium transmission profile at 1k resolution

Figure 3.7: Transmission profiles at 1k, 2k, and 4k camera resolution. The pixelation difference in the transmission profiles aren't readily discerned on printed media, but the effect on the reconstruction is apparent, as shown in Figure 3.8.

Porous medium transmission profile at 2k resolution
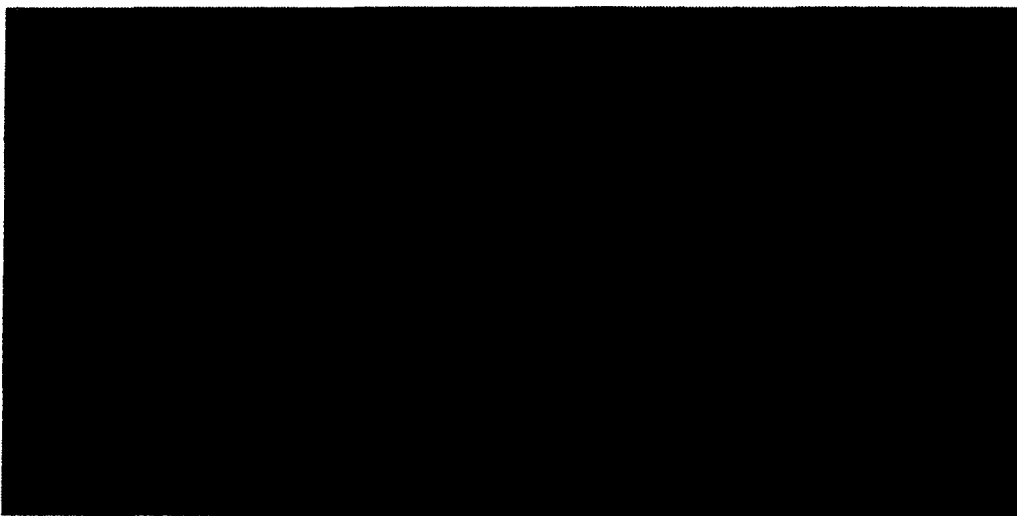
Porous medium transmission profile at 4k resolution

Figure 3.7 continued: Transmission profiles at 1k, 2k, and 4k camera resolution. The pixelation difference in the transmission profiles aren't readily discerned on printed media, but the effect on the reconstruction is apparent, as shown in Figure 3.8.
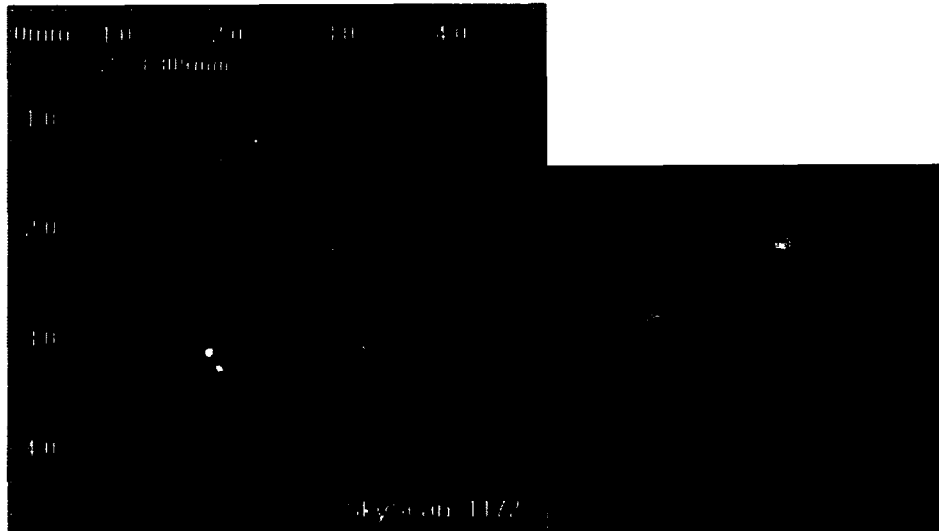
Reconstruction of a porous medium at 1k resolution

Reconstruction of a porous medium at 2k resolution

Figure 3.8: Reconstructions from a dataset sampled at 1k, 2k and 4k resolution.
The expanded area on the right of each figure shows a marked increase in quality.

Reconstruction of a porous medium at 4k resolution

Figure 3.8 continued: Reconstructions from a dataset sampled at 1k, 2k and 4k resolution. The expanded area on the right of each figure shows a marked increase in quality.

3.1.3.2 Object Stage Position

The sample in the scanner is positioned on a pedestal, termed the *stage*. The sample container is fixed onto the stage with putty or adhesive to immobilize the sample during the scan. The stage moves closer and further away from the detector as the resolution is changed by the user. The object stage position is interlinked with the resolution that can be obtained, as shown in Table 3.1 and examples are shown in Figure 3.9. The closer the stage is to the detector, the greater resolution that can be obtained, but the smaller the field of view. There is therefore a trade-off in the quality and the quantity of information that can be obtained. For this study, the quality of the information was deemed most important and the "near" stage position was selected. In Figure 3.9 the over-saturation of the stage in the "near" position is apparent. Over-saturation can harm the detector and steps need to be taken to avoid this. The easiest way is to decrease the energy of the x-rays, however, doing so also decreases the information returned as the contrast between phases in the sample may become obscured.

Transmission profile with the object stage in the far position

Transmission profile with the object stage in the middle position

Figure 3.9: The three object stage position. The over saturation in the near position is due to the default exposure time in this position. Over saturation should be avoided since it can damage the detector, and decreases the amount of contrast in the reconstruction.

Line 1040 (min=28.2%, max=100.0%, av=88.9%)
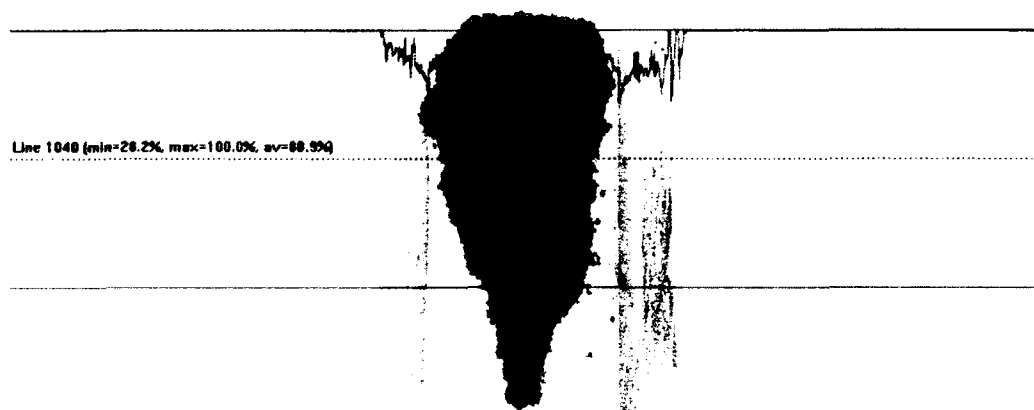
Transmission profile with the object stage in the near position

Figure 3.9 continued: The three object stage position. The over saturation in the near position is due to the default exposure time in this position. Over saturation should be avoided since it can damage the detector, and decreases the amount of contrast in the reconstruction.

3.1.3.3 Filters

The ability to filter low energy x-rays from the scan, greatly enhances the ability to distinguish features from the object. The SkyScan 1172 comes equipped with an Aluminum filter and a mixed Aluminum-Copper filter. If the object being examined is highly absorbent, it might not be possible to find the right contrast to realize internal features. This inability is the case with very dense materials such as metals, or high density rock. The porous material in Figure 3.10 (a) shows good contrast with the background air, but as the background level is at saturation, it is advisable to either decrease the energy of the x-rays, or apply a filter. This will decrease the chance of damaging the detector.

Line 1040 (min=28.2%, max=100.0%, av=88.9%)
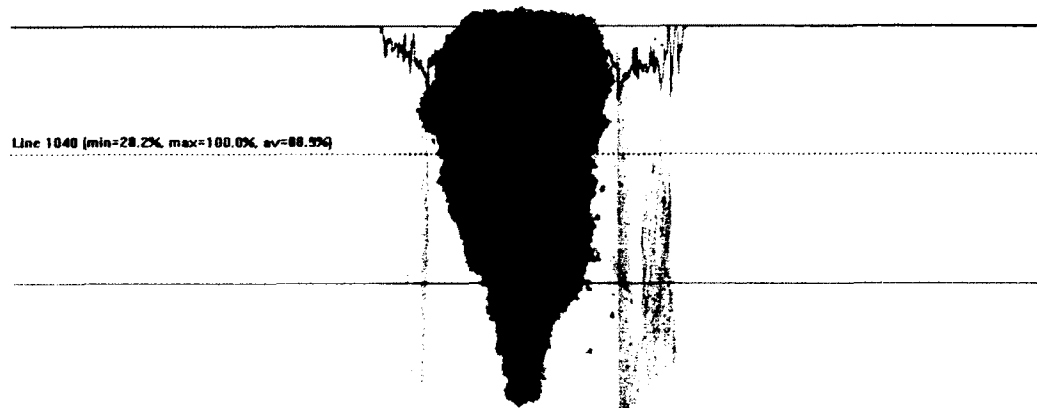
(a) Transmission profile with no filter

(b) Transmission profile with the aluminum filter

Figure 3.10: Transmission profiles with no filter, aluminum filter, and the mixed aluminum-copper filter. There is almost no difference in the absorption between the minimum and maximum values for the aluminum-copper filter, and hence segmentation of the reconstructed image will prove to be very difficult.
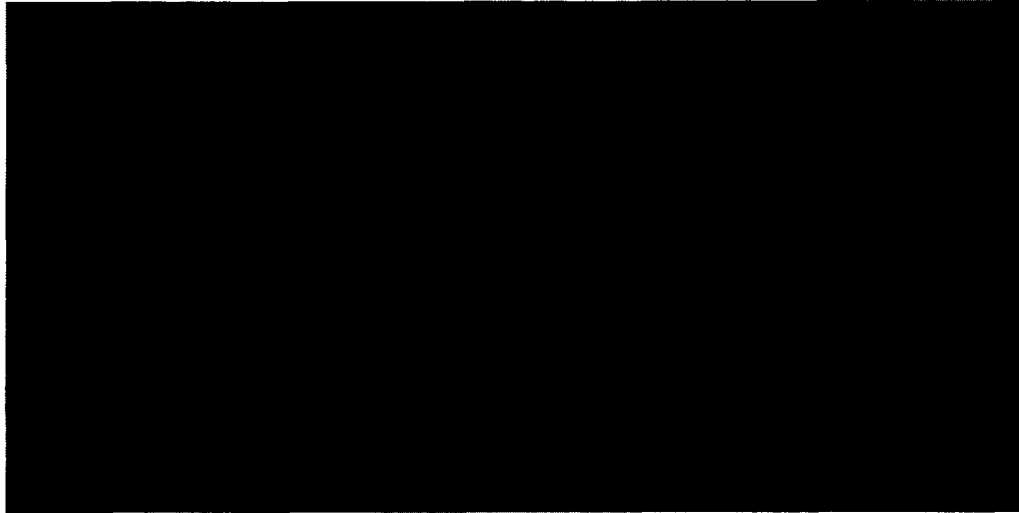
(c) Transmission profile with the aluminum-copper filter

Figure 3.10 continued: Transmission profiles with no filter, aluminum filter, and the mixed aluminum-copper filter. There is almost no difference in the absorption between the minimum and maximum values for the aluminum-copper filter, and hence segmentation of the reconstructed image will prove to be very difficult.

From Figure 3.10, it is apparent that the shadow image becomes darker with the application of a more dense filter. The x-ray absorption of the Al-Cu filter almost completely masks the object. For this study the material selection was such that the 0.5 mm Aluminum filter was required. In some cases the sample was small enough not to use the filter, and this drastically decreased the scanning time.

3.1.3.4   Image Averaging

At each rotation step, several shadow projections can be recorded and averaged to create a composite image of higher quality. Each exposure to the x-ray source takes the same amount of time, thus if a six fold average is taken, the scan will take 6 times longer. Figure 3.11 shows a reconstruction of the porous medium with no averaging, and with 6 times averaging. The image quality is much more homogeneous in the averaged sample. Variation in apparent densities of the object make segmentation difficult, so it is

important to start the segmentation process from as homogeneous reconstruction as possible. This variation can be seen as noise in the sample, and the less noise, the better the reconstruction.

Reconstruction with no averaging

Figure 3.11: Reconstruction of a porous medium with and without averaging applied. In the reconstruction with averaging, the image appears more homogeneous, which indicates that there is less noise. This will aid segmentation of the reconstructed slice.

Reconstruction with averaging

Figure 3.11 continued: Reconstruction of a porous medium with and without averaging applied. In the reconstruction with averaging, the image appears more homogeneous, which indicates that there is less noise. This will aid segmentation of the reconstructed slice.

In Figure 3.11 it is apparent that the reconstruction with averaging appears a lot more homogeneous than the reconstruction without averaging, i.e. with averaging the outlying pixels (very dark, and very bright) are brought towards the norm of the surrounding pixels. For this study the averaging was kept between 3 and 7, depending on the size and material of the sample.

3.1.3.5 Object Rotation

Two general options exist when it comes to object rotation. The object can be rotated through a full 360 degrees, or only through 180 degrees. In both of these options the step size is specified by how many degrees each rotation step incurs. When the object moves only through 180 degrees, the information captured from the scan is not only less than the

360 degree option, but the quality of the information also decreases, as the x-rays are absorbed through the sample. In the 180 degree option, the "back" of the sample is reconstructed from extrapolated data.

Figure 3.12 shows the reconstruction of a porous medium at 180 and 360 degree rotation. The 360 degree rotation reconstruction shows a lot less variation in the apparent density of the medium, which makes segmentation easier. As with averaging, the less noise in the sample, the better the reconstruction.

Reconstruction at 180 degree rotation

Figure 3.12: Reconstruction at 180 and 360 degree rotation. Rotating the sample through the full 360 degrees, decreases the amount of noise in the sample and eases future segmentation and reconstruction.

Reconstruction at 360 degree rotation

Figure 3.12: Reconstruction at 180 and 360 degree rotation. Rotating the sample through the full 360 degrees, decreases the amount of noise in the sample and eases future segmentation and reconstruction.

For this study 360 degree rotation was used through out. The quality of the initial data is very important for the subsequent steps towards finite element modeling.

3.1.4 Reconstruction

3.1.4.1 Alignment

Once all the shadow images have been collected, the slice reconstructions have to be aligned to form a coherent reconstructed image. Since the object being examined is not precisely centered, the user has to manually adjust for any discrepancies in the alignment. The reconstruction software does however provide assistance and an initial guess of the alignment. The correct alignment of the images is paramount in creating a successful reconstruction and is also the first indication if the reconstruction can be successful. For instance, if the sample moved from its position during the scan, the images will not be

able to align, and the scan will have to be redone. In samples where the internal cohesion is not strong, for example dry sand particles, vibration may cause the particles to move slightly, which will cause misalignment of the final slice images.

Figure 3.13 shows three reconstructed images, one perfectly aligned, one with one degree misalignment, and the last with 2 degrees misalignment. The decrease in quality of the final reconstructed image is apparent with an increase in misalignment.

Slice with reconstruction in perfect alignment

Figure 3.13: Reconstruction showing the effect of misalignment. In the enlarged figures on the right, the misalignment can be seen as an unfocused haze at the particle edges. This decreases the quality of the scan, and hence influences the final reconstruction.

Slice with reconstruction at 1 degree misalignment

Slice with reconstruction at 2 degrees misalignment

Figure 3.13 continued: Reconstruction showing the effect of misalignment. In the enlarged figures on the right, the misalignment can be seen as an unfocused haze at the particle edges. This decreases the quality of the scan, and hence influences the final reconstruction.

3.1.4.2 Smoothing

Smoothing of the reconstructed images allow for a more homogeneous apparent density of the internal structure. Excessive smoothing can however blur the boundaries between the porous medium and the pore space, which would negatively affect the accuracy of the final reconstruction. Figure 3.14 shows 3 images with incremental amounts of smoothing applied. The excessive amount of smoothing applied in the final image will negatively impact on any future calculations.
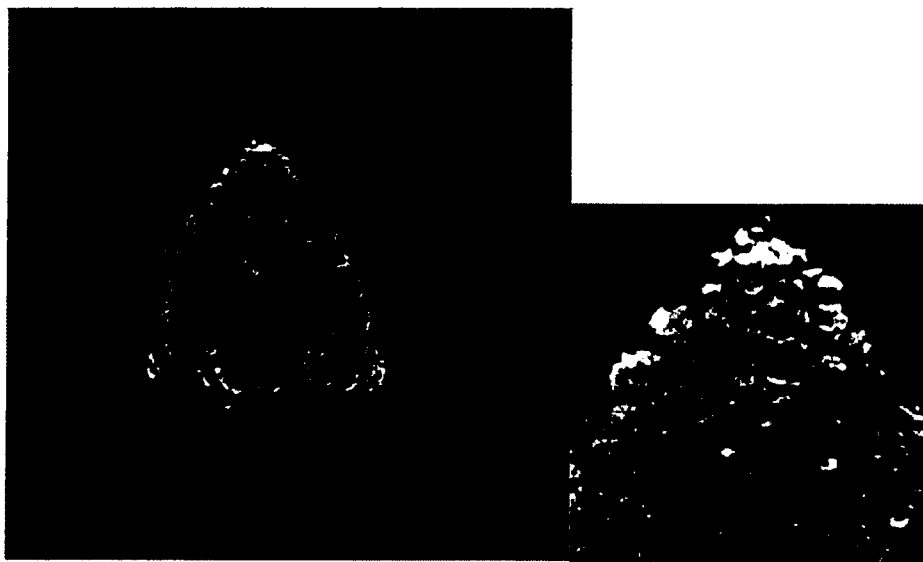
Reconstruction with no smoothing

Figure 3.14: Reconstructions showing the effect of smoothing. In the figures on the right, the smoothing can be seen as it decreases the sharpness of the image. Smoothing can be used to eliminate noise, but too much smoothing will negatively impact the quality of the scan.

Reconstruction with 4 degrees of smoothing

Reconstruction with 8 degrees of smoothing

Figure 3.14 continued: Reconstructions showing the effect of smoothing. In the figures on the right, the smoothing can be seen as it decreases the sharpness of the image. Smoothing can be used to eliminate noise, but too much smoothing will negatively impact the quality of the scan.

3.1.4.3 Beam Hardening

An x-ray source emits photons with a range of energies. Those photons with lower energies are more easily attenuated than the high energy photons, leading to the phenomena that there is not a linear relationship between the size of a sample and the amount of energy absorbed (Brooks & Chiro, 1976). Thus the average specific energy of the photons passing through a thick section of a sample will be higher ("harder") than that passing through a thin section. Or putting it another way, the relative amount of energy absorbed by a thin section, will be more than that for a thick section. Visually, it seems as if there is a thin layer of highly dense material on the outside of the sample (where the low energy photons are absorbed), and then as if the density of the sample decreases towards the center of the sample. This phenomenon is termed *beam hardening*. The beam hardening effect can be somewhat accounted for with image transformation, but it is a manual process controlled by the user. The beam hardening effect and its compensation are shown in Figure 3.15.

Reconstruction with no beam hardening

Figure 3.15: Reconstructions showing the effect of beam hardening. The change in apparent density towards the center of the sample is negated by adjusting for the beam hardening effect.

Reconstruction with 50% beam hardening
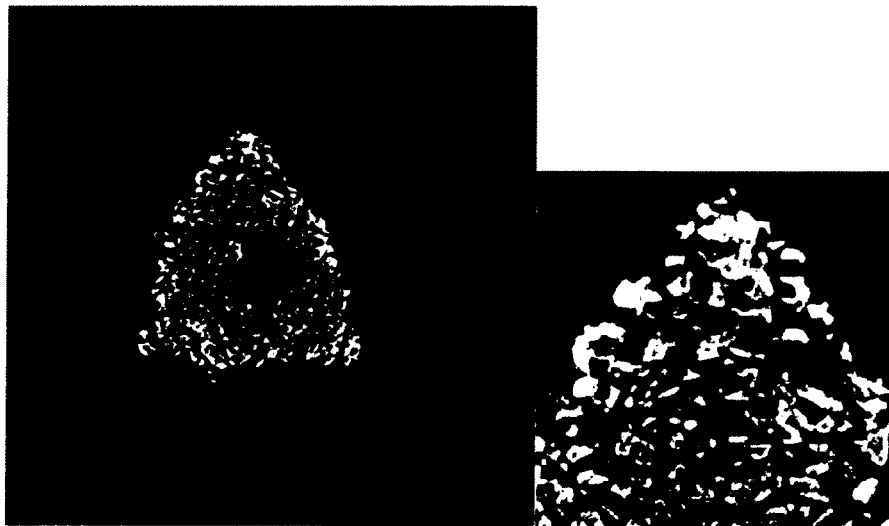
Reconstruction with 100% beam hardening

Figure 3.15 continued: Reconstructions showing the effect of beam hardening. The change in apparent density towards the center of the sample is negated by adjusting for the beam hardening effect.

With a high level of beam hardening correction, the outer parts of the sample become completely saturated (notice all the edges are white and not shades of grey). Thus any information that would have been available with regards to the variation in density is completely lost. In this study the beam hardening correction was adjusted in each scan to the appropriate level, enough compensation to decrease artefacts, but not too much to significantly decrease the usability of the data.

3.2 Model Preparation

The two dimensional reconstructions created through x-ray imaging must be converted to a three dimensional model in order for finite element analysis to be applied. It is also in this step of the process that the final spatial dimensions of the model are determined. The spatial extent is termed the *Region of Interest* (ROI). This region of interest must be equivalent to the *Representative Elementary Volume* (REV) for the model to be of significance.

3.2.1 Region of Interest

The region of interest is the three dimensional extent from which the three dimensional reconstructed model will be created. In Figure 3.16 a cross section and a shadow image from a scan conducted on wetted sand grains is shown.
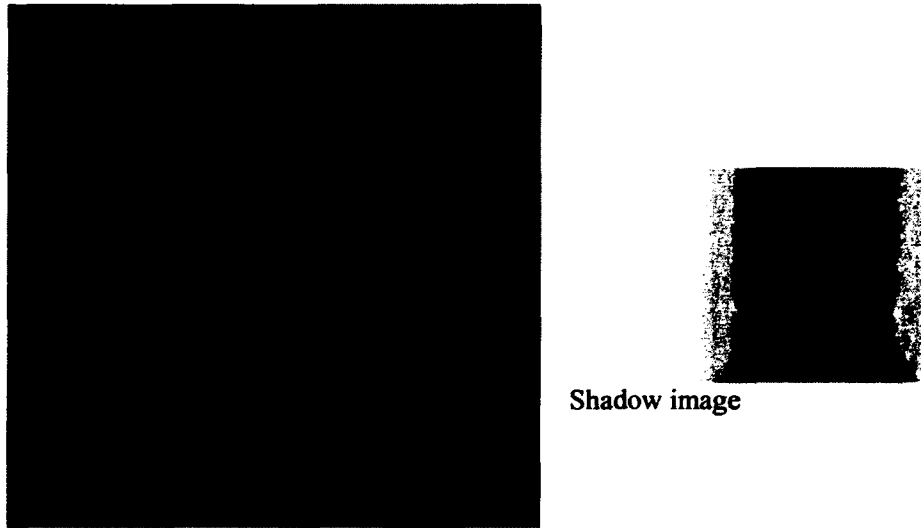
Shadow image

Cross section

Figure 3.16: Cross section and shadow image of wetted sand grains

In the scanning process, it frequently occurs that the region in which one is interested cannot be isolated. A lot of unnecessary information is included in the scan, as is illustrated with the inclusion of the area outside the tube in Figure 3.16. To negate carrying forward the unwanted information, a region of interest is created from which only the necessary information is extracted. In Figure 3.17 the same cross section is shown but with the region of interest highlighted.

Slice view with the region of interest
highlighted

Extracted region of interest
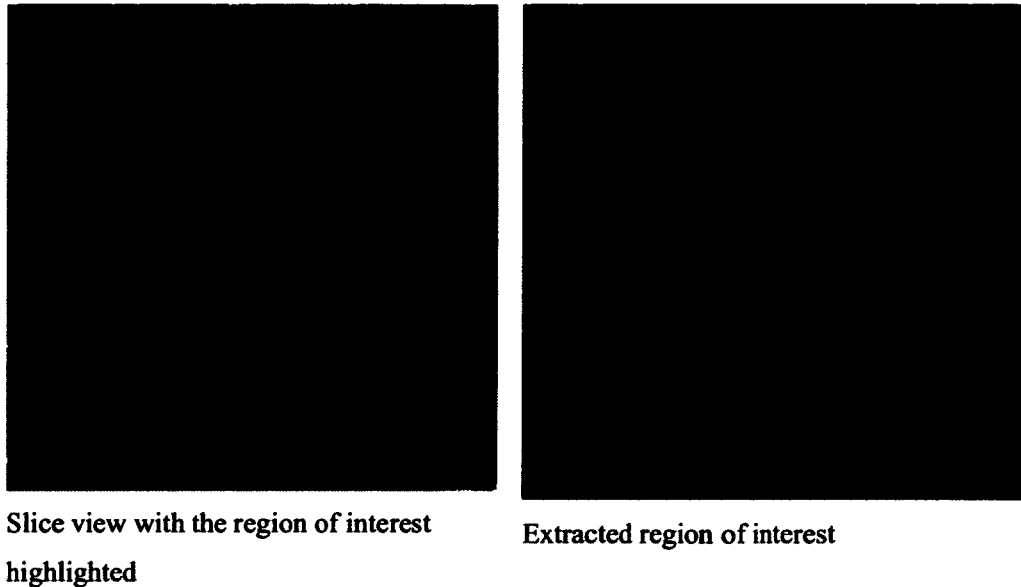
Figure 3.17: Slice reconstruction highlighting the extraction of the region of interest.

In this case the ROI would be a cylinder of particles and hence an ROI is created that only includes these particles. This ROI is then extracted from the original scan and saved as a new stack of slices. Even though an ROI can take any three dimensional form, the slices are always saved in the standard rectangle. The negative area thus created (seen as the black area in Figure 3.17), contains no useful information, and is negligible from a computational point of view. Creating an ROI has three very important advantages:

- There is no reduction in the *quality* of the information being processed,
- The *quantity* of information is reduced, thus the computational load is decreased,
- Information that may hinder visual inspection of the three dimensional model can be removed ahead of reconstruction.

Once the ROI has been selected the image is segmented to delineate the area which should be included in the three dimensional reconstruction.

3.2.2 Segmentation

The segmentation of an image is the process of selecting pixels which will be included in the three dimensional reconstruction. The most basic form of segmentation is *threshold analysis*. In this process the grey values of each pixel, which range from 0 to 255, determine if the pixel will be included in the model. Note that "grey value" does not mean that the image is necessarily comprised of only grey pixels. A host of color maps can be applied to an image to better visually gauge the segmentation boundaries. In Figure 3.18 three different color maps are applied to scan conducted on zeolites containing a non aqueous phase liquid (NAPL). The ease in identifying the NAPL between the particles between the three images is quite apparent. In the image to the left, the NAPL stands out as yellow pendular rings between the blue particles. In the center image the NAPL is faintly visible as light grey pendular ring between the particles, and in the image to the right, the NAPL is not visible at all. Since segmentation is a subjective process, the choice of color map is important.

Figure 3.18: Different color maps can be applied to visually aid in the segmentation process.

3.2.2.1 Threshold Analysis

In the basic form of threshold analysis the image is segmented into two regions, that region which should be included in the 3D reconstruction and that region which should be discarded. There is little intelligence in such an application and erroneous

measurements can result from not carefully analyzing the post processing data. A sample of coarse sand with interstitial water is shown in Figure 3.19. As an example, the final application of this particular scan will be to determine its saturated hydraulic conductivity. To determine the saturated hydraulic conductivity of the sand it is necessary to isolate the air from the image and extract it for further use. The histogram in Figure 3.20 is divided in 256 bins, representing the grey values of the scan. The 0-value is black (no x-ray attenuation), 255-value is white (complete x-ray attenuation) and a linear grey scale lies in between. In the histogram two "humps" are evident. The first hump lying between 1 and 15, is the pixel range (the grey values) attributed to the air. The air will attenuate less x-rays (essentially only noise) and is therefore closer to the 0 point. The second hump can be attributed to the sand particles. Water can not readily be distinguished with this thresholding method.

(a) Slice reconstruction   (b) Thresholded image   (c) De-speckled image
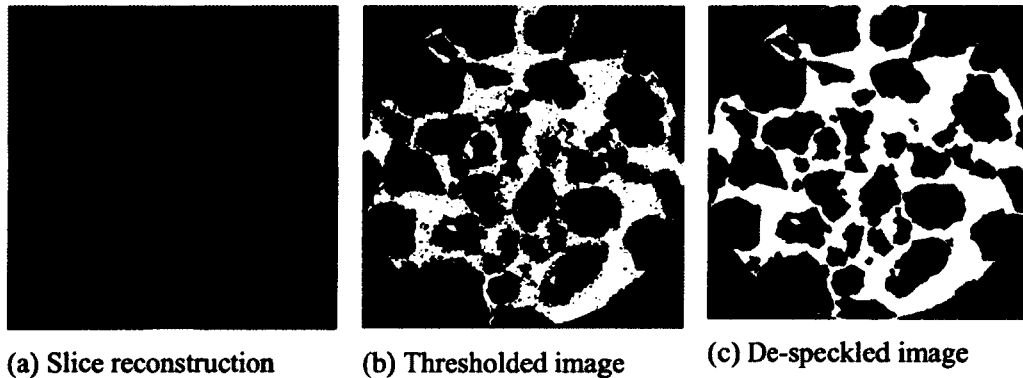
Figure 3.19: A reconstructed slice with thresholding and de-speckling applied.
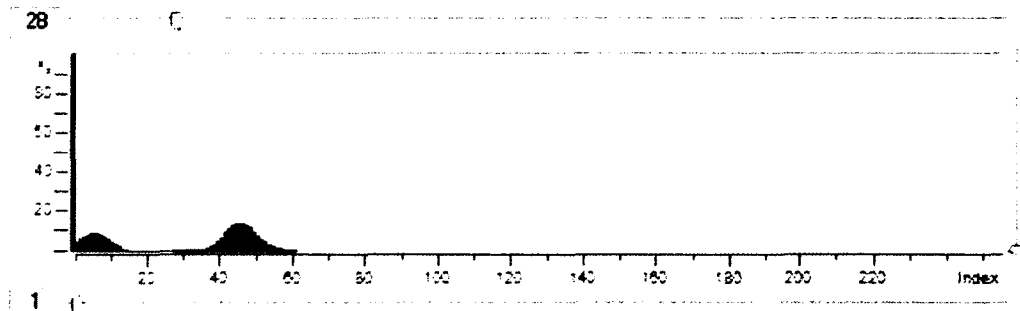
Figure 3.20: Histogram showing the distribution of grey values in the image.

In Figure 3.20 the pixels between 1 and 28 (inclusive) are selected to be part of the final model. If the white area is analyzed numerically, a perimeter to area ratio of 0.06 μm^{-1} is found. This value is useful in predicting the saturated hydraulic conductivity in one of the incarnations of the Kozeny-Carman equation and can be likened to the specific area of a three dimensional sample. Visually, however, the image appears speckled and this is due to the noise in the original scan. One way that this phenomenon can be alleviated is through de-speckling of the image. Software algorithms allow for negative space (the black areas) which is completely surrounded positive space (the white areas) to be changed to positive space. This can be done in two and three dimensions, though it tends to be computationally very expensive. The resulting image of such an exercise is shown in Figure 3.19 (c). A numerical analysis of this image shows a perimeter to area ratio of 0.02 μm^{-1}, three times less than the original image. Moreover, if a three dimensional volume were to be constructed of the original image, the resulting model would be orders of magnitude larger in size due to the additional surface area created by the noise.

The sample in Figure 3.19 contained three distinct phases, air, water and solid sand grains. However in the segmentation process, the aqueous phase was lost in the noise. It is very important to note that if the original x-ray scan is not conducted at settings that promote the separation of the phases from one another, no amount of post processing will allow the segmentation to be completed successfully. In Figure 3.21 a reconstruction is

shown of zeolite particles entrained with and an aqueous phase and a non-aqueous phase. Thus in this scan four separate phase could be detected, through the careful selection of the scanner settings.
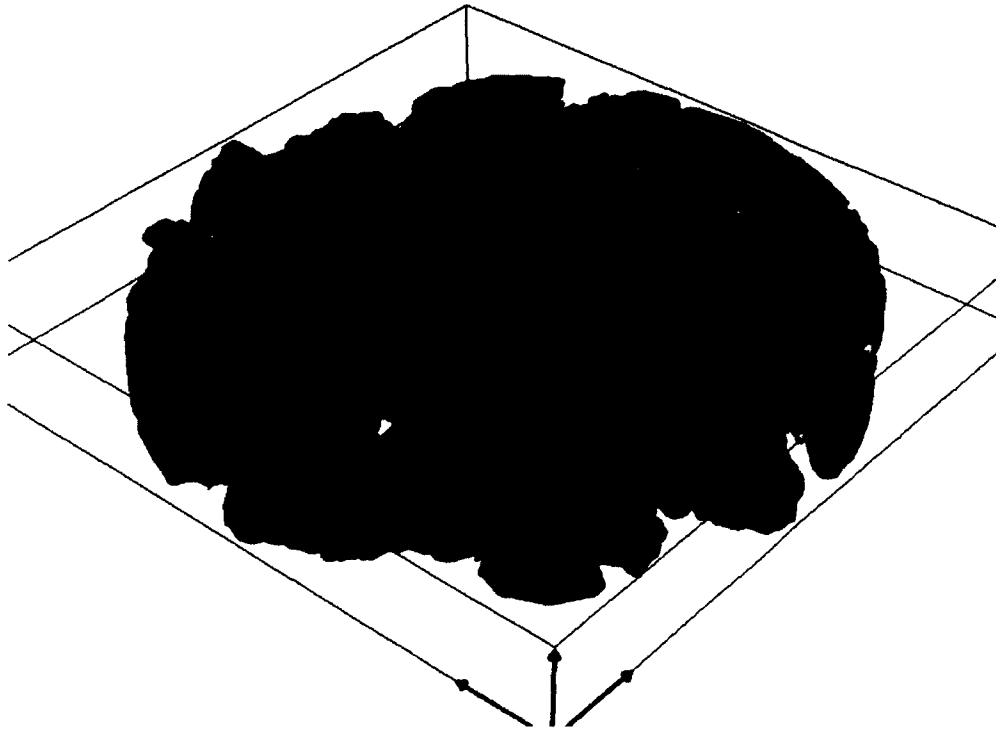
Figure 3.21: Reconstruction of zeolite containing four phases: zeolite, air, water and a NAPL. The brown areas are the zeolite, blue areas are water and yellow areas are the NAPL. The air is transparent.

3.2.2.2 Smoothing

The preferred noise reduction methodology used throughout the study is Recursive Gaussian Smoothing. In this methodology the grey value of a pixel is evaluated against those around it, and then adjusted according to a Gaussian distribution. The spatial sigma

(how far in mm should the smoothing be effective) is a variable that can be adjusted in all three the spatial directions. This is useful when the original scan does not have the same resolution in all three directions. Figure 3.22 is a zeolite infiltrated with NAPL. In the first segmentation only basic thresholding is applied and the noise in the resulting image is apparent. After smoothing, the image is much more homogeneous. This methodology is superior to the aforementioned despeckling methodology in that real features, such as the macro pores in the zeolite, will not incorrectly be erased. Each of the colored areas in Figure 3.22, which correspond to different threshold values, is termed a *mask*. Each mask can be separately manipulated and extracted depending on which region will be carried forward for finite element modeling.

| Slice reconstruction | Thresholded image | Smoothed image |
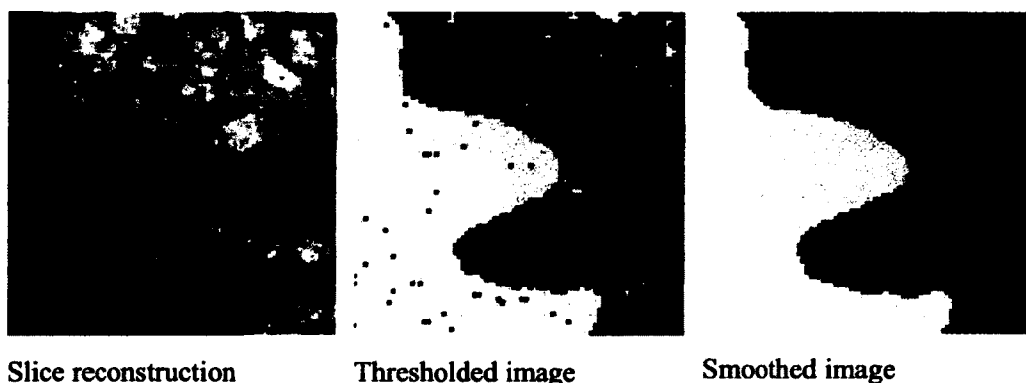
Figure 3.22: Post-reconstruction smoothing is necessary to obtain a useable model.

3.2.2.3 Floodfill

The floodfill methodology is the preferred segmentation method prevailing in this study. When investigating advection and diffusion at the pore scale, it is important to only consider that pore space which actively contributes to the transport mechanism. In any porous media, pore space exists that is either not connected to any other pores, or do not stretch between the boundaries of the selected Representative Elementary Volume. The inclusions, or dead end pores, should be subtracted from the porosity of the porous media in calculations. This is then termed the *effective porosity*. The floodfill algorithm enables

the selection of the effective porosity quickly and efficiently. Seed points are selected on the boundary of the REV and only pixels that are connected to these seed points will be included in the final model. In such a fashion, those internal pore spaces which are not connected to the boundary will not be included in the model, as well as the pores that do not stretch the entire length of the REV. Figure 3.23 is a reconstruction of the pore space inside a sandstone sample. The additional pore space that would have been include had the floodfill methodology not been used, is evident.
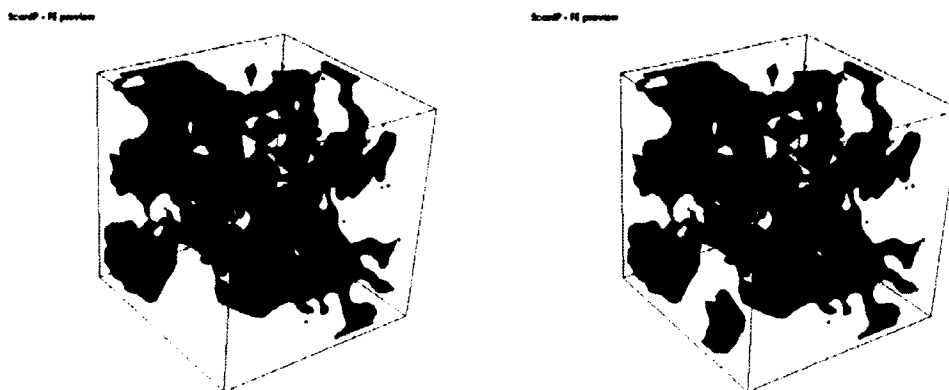
Reconstruction with the floodfill algorithm   Reconstruction with regular segmentation

Figure 3.23: Reconstruction showing the advantage of using the floodfill algorithm. Note the additional pore space in the bottom left hand corner that would have been included in the regular segmentation. It is however possible that, after resampling, additional unconnected pore space will appear, as is present in this reconstruction with the small area at the top/back of the reconstruction.

3.2.2.4 Resampling

The resampling of an image is crucial in obtaining a model that is computationally not too expensive. In the resampling of an image, the pixels are averaged in relation to its neighbors, and hence information about the image is irretrievably lost. Figure 3.24 shows the reconstructed pore space (the porosity) in a ceramic disk at the original resolution,

2.24 μm, at 3.78 μm (60% of the original) and 11.2 μm (20% of the original). The degradation in the reconstruction quality is evident. Figure 3.25 shows the reduction in the estimated number of finite elements needed to mesh each of the volumes as well as the reduction in physical volume (the porosity). The reduction in the porosity can be taken as a measure of the information lost in the model, due to the averaging of pixels in the resampling.

Reconstruction a 2.24 μm   Resampled image at   Resampled image at 11.2
                            3.78μm   μm
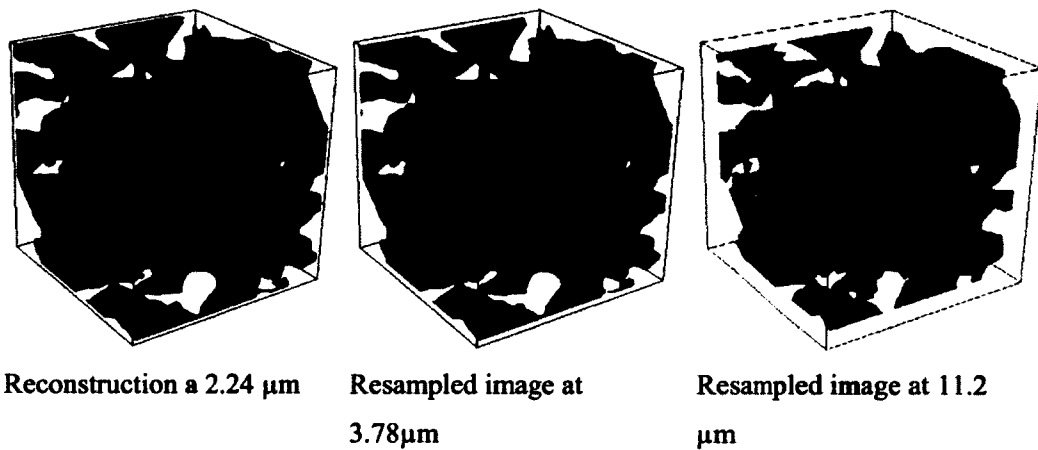
Figure 3.24: Resampling of a dataset is necessary to obtain a model that is computationally inexpensive. Resampling does however decrease the quality of the model.
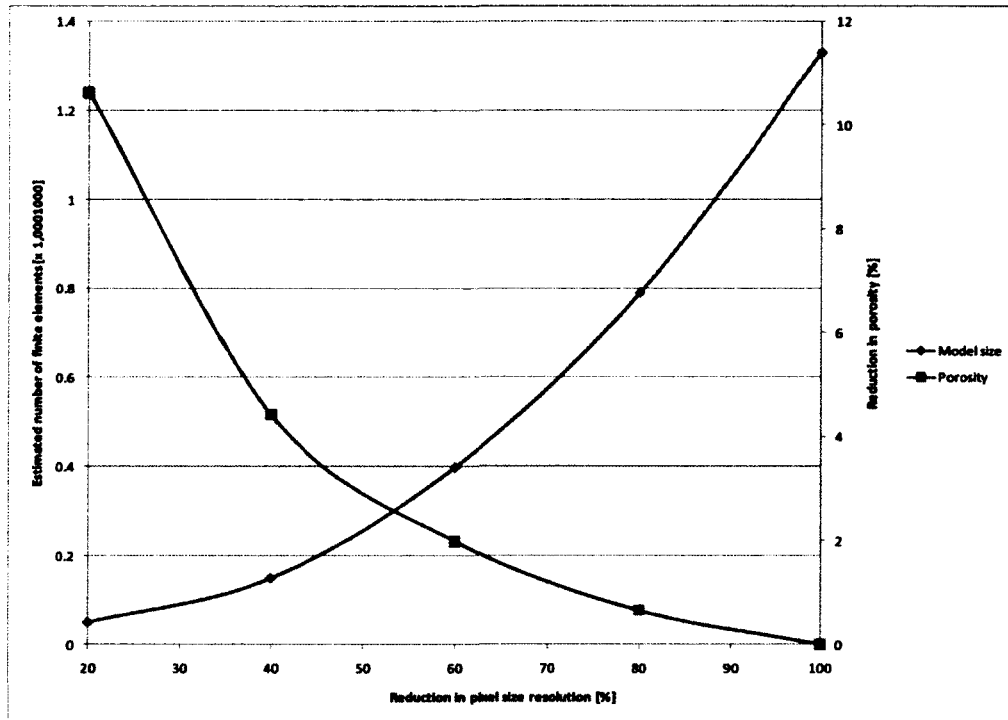
Figure 3.25: Relationship between pixel size and the model size and porosity.

At a 60% reduction from the original pixel size resolution, the estimated number of finite elements decreases from 1.3 million to around 350,000, at the same time the porosity decreases less than 2%. At the current technological limits anything below 600,000 elements can be modeled in a reasonable amount of time, provided that the model surfaces are not overly complicated.

3.2.3 3D Reconstruction

Throughout the model preparation, it is important to note that the spatial characteristics of the sample are always preserved. At the scanning stage each pixel is linked to a spatial extent, (the *resolution*), and that resolution is adjusted accordingly when the two dimensional images are resampled. Once all the necessary masks have been demarcated,

the three dimensional reconstruction can be rendered by virtually stacking all the x-y oriented two dimensional images on top of one another in the z-direction (Figure 3.26). As each x-y oriented pixel is extruded into the z-direction, the resulting object is termed a *voxel*. A surface is then created, linking all the perimeters of a mask. The enclosed surface can then be exported as a volume, depending on the file format requirements. In the case of reconstruction software used, ScanIP, a volume is created which is meshed in ScanFe before it is imported into Comsol.

Three dimensional reconstruction sliced vertically to view internal structures

Stack of slice images

Figure 3.26: Slice images are stacked on top of each other to form a three dimensional image.

3.3 Finite Element Analysis

3.3.1 The Finite Element Method

The finite element method found its origins in 1941 with Hrennikoff and 1943 with Courant were they explored the uses of lattices and triangles to solve a structural domain. The first use of the finite element to solve complex geometries for application in industry

was shown by Turner et al. (1956), and Clough (1990) gives a good background as to the development of this method in their work at Boeing during the early 1950s. The term "Finite Element" was first used by Clough (1965). The application of the finite element method to flow problems, rather than structural stiffness and deflection problems, were shown by Zienkiewicz & Cheung (1965) and De Vries & Norrie (1971). Solutions to the incompressible Navier-Stokes equations were published Taylor & Hood (1973), Smith & Brebbia (1975) and Brooks & Hughes (1982). The formulation used by Comsol, and hence in this study, was developed by Hauke & Hughes (1994).

Aqueous diffusion problems in finite element analysis are mostly found in its application of the advection-diffusion formulation of contaminant transport. Heinrich et al. (1977) describes such transport, Chock (1978) applies it pollutant dispersions near roadways and Douglas & Russell (1982) describes the finite element model when diffusion is not the dominant term in transport. The advent of personal computers allowed more complex problems to be solved and several software packages, specifically geared toward hydrogeology and aqueous contaminant transport appeared. SUTRA was developed by the United States Geological Survey (Voss, 1984) and the most current release was updated in September 2010. FEFLOW was developed by Diersch in 1979 and the first publication citing FEFLOW as the software used was published in 1988 (Diersch, 1988). FEFLOW version 6 was updated in June 2010. Hydrus was developed by Šimůnek et al. (1992) and was last updated in February 2010. All these packages, including Comsol described in the next section, allow two and three dimensional analysis of diffusion processes.

3.3.2 Comsol Multiphysics

Comsol Multiphysics is a software package that uses the finite element method to solve partial differential equations. The software uses a graphical user interface, although a command line script is available for specialized problems. The script uses the Matlab

syntax, as Comsol was originally an add-on for Matlab. Previous to 2004, the software
was marketed as Femlab.

The software is currently available across all the major platforms in both 32-bit and 64-
bit versions. Several major upgrades to the software occurred in the period of the study
and the impact of these changes will be discussed in the appropriate sections.

The mathematics shown in this dissertation is all based on the implementation of the
partial differential equation as used in Comsol. Each equation set has its own
implementation module, which in Comsol is called an *Application Mode*. This
dissertation will follow the nomenclature as used in Comsol closely, as to aid the reader
in reproducing the experiments if need be.

3.3.3 Governing equations

3.3.3.1 The Navier-Stokes Application Mode

Fluid dynamics in Comsol is modeled through the Navier-Stokes equations. Allowance is
made only for incompressible fluids, however in this study the assumption that the fluid
is incompressible is quite valid. An additional Application Mode, the Chemical
Engineering Module, allows for a less generalized application, which could include
weakly compressible fluids, turbulence models etc. Equation (3.1), the momentum
transport equation, and Equation (3.2), the continuity equation, show the generalized
Navier-Stokes equations used for the study.

$$\rho \frac{\partial u}{\partial t} - \nabla \cdot \left[\eta \left(\nabla u + (\nabla u)^T \right) \right] + \rho (u \cdot \nabla) u + \nabla p = F \qquad (3.1)$$

$$\nabla \cdot u = 0 \qquad (3.2)$$

Where **u** is the velocity field [m/s],

t is the time [s],

η is the dynamic viscosity [Pa.s],

ρ is the density [kg/m^3],

p is the pressure [Pa], and

F is the volume force, such as gravity [N/m^3].

The velocity field **u** is comprised of the velocity in the 3 primary directions, x, y and z, and are named u, v and w. Together with p, the pressure, these 4 variables form the dependent variables from which a solution is computed. The default Lagrange – P$_2$P$_1$ elements were used.

3.3.3.2 The Diffusion Application Mode

The diffusion application mode is an elementary application of Fick's Law, shown in Equation (3.3):

$$\delta_{ts}\frac{\partial c}{\partial t} + \nabla \cdot (-D\nabla C) = R \qquad (3.3)$$

Where δ_{ts} is a time-scaling coefficient,

D is the diffusion coefficient [m^2/s],

C is the concentration [kg/m^3], and

R is the reaction rate [kg/m^3.s].

In this application mode the concentration is the only dependent variable and the default Lagrange – Quadratic elements were used for the simulation.

3.3.4 Boundary Conditions

3.3.4.1 The Navier-Stokes Application Mode

The boundary conditions are necessary to define the flow through the porous medium. The flow simulations were conducted in all three axial directions and the boundary conditions were changed in the appropriate manner to reflect the desired change in flow direction. Figure 3.27 shows the four classes of boundary conditions used, and Figure 3.28 shows the reconstructed pore volume from which these boundaries were determined, to aid the reader in the visualization of these boundaries. For flow in the z-direction the boundary conditions used are shown in Table 3.2.
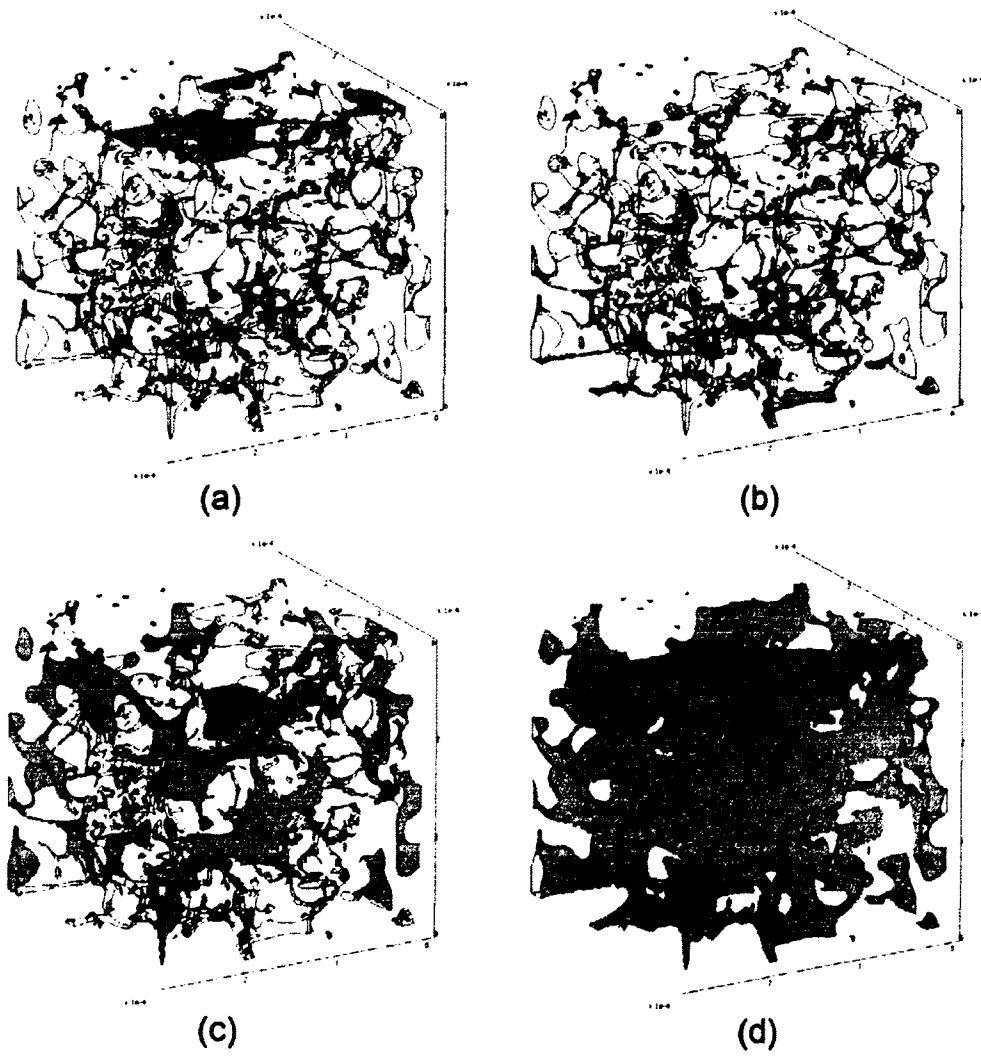
Figure 3.27: The four boundary classes used in the model (a) Inlet, (b) Outlet, (c) Representative elementary volume boundaries, and (4) Porous medium.
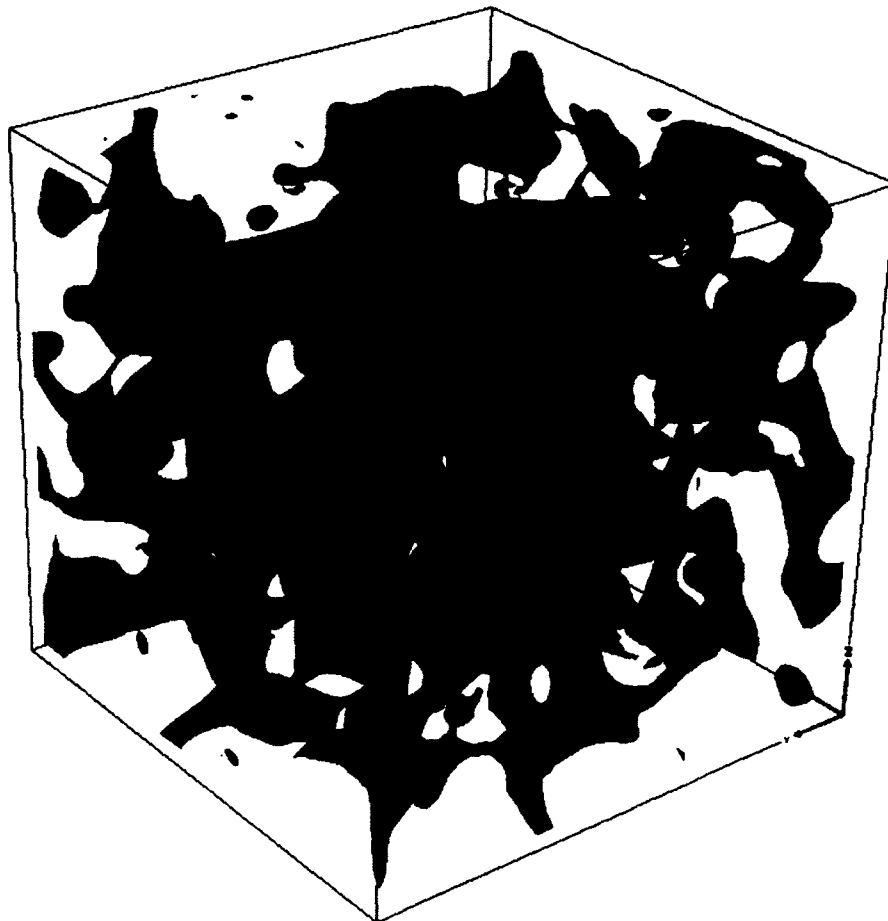
Figure 3.28: The reconstructed pore volume from which the pore boundaries in Figure 3.27 were determined.

Table 3.2: Boundary conditions for the flow simulation.

Boundary	Boundary Condition	Value	Equation
Inlet	Pressure	$p_0 = 0.01$	$\left[-p\mathbf{I} + \eta\left(\nabla\mathbf{u} + (\nabla\mathbf{u})^T\right)\right]\mathbf{n} = -p_0\mathbf{n}$
Outlet	Pressure	$p_0 = 0.001$	$\left[-p\mathbf{I} + \eta\left(\nabla\mathbf{u} + (\nabla\mathbf{u})^T\right)\right]\mathbf{n} = -p_0\mathbf{n}$
Porous media	No slip	$\mathbf{u} = 0$	
REV	Slip/Symmetry		$\mathbf{n}\cdot\mathbf{u} = 0$, $\mathbf{t}\cdot\left[-p\mathbf{I} + \eta\left(\nabla\mathbf{u} + (\nabla\mathbf{u})^T\right)\right]\mathbf{n} = 0$

The inlet and outlet pressures were chosen to induce a flow that would result in a pore Reynolds number < 1. This will ensure that laminar conditions prevail and that the assumptions of Darcy's Law remain valid. The no slip condition on the porous media boundary is a standard condition for flow over a solid boundary. On the boundaries were fluid flow occurs, a slip/symmetry boundary was chosen to ensure that flow continues in the desired flow direction.

3.3.4.2 The Diffusion Application Mode

As with the flow simulations, the diffusion simulations require boundary conditions to define the diffusion process. The same classes of boundary conditions are used (Figure 3.27) and the specific application is shown in Table 3.3

Table 3.3: Boundary conditions for the diffusion simulation.

Boundary	Boundary Condition	Value	Equation
Inlet	Concentration	$C_0 = 3.27 \times 10^{-3}$	$C = C_0$
Outlet	Flux	$k_c = 5$	$-n \cdot N = N_0 + k_c(C_b - C)$, $N = -D\nabla C$
Porous media	Insulation/Symmetry		$n \cdot N = 0$, $N = -D\nabla C$
REV	Insulation/Symmetry		$n \cdot N = 0$, $N = -D\nabla C$

The inlet boundary concentration was set at the same concentration as the concentration of iodide in the source cell (see section 3.5). The outlet boundary was set at a high mass transfer coefficient to simulate the large receiving cell and that there will be no backwards osmotic pressure. Thus all the iodide molecules arriving at the outlet will be removed at a very high rate. The boundaries of the porous media and the *Representative Elementary Volume* were stipulated as insulation/symmetry to simulate the conservative nature of the iodide tracer.

3.3.5 Importation of a Three Dimensional Object

As mentioned previously, stereolithographic files (.stl) are the most common form of three dimensional objects described by a surface. On importation of these files, Comsol attempts to group the triangular mesh of the .stl surface into faces, which can then contain boundary conditions for a simulation. The grouping of the .stl mesh elements are primarily achieved by analyzing the angle between neighboring elements. Thus, for instance, a planar surface can be identified as the neighboring elements having a zero degree tilt between the elements. The elements should also be of sufficient quality (e.g. height to base ratio) to facilitate the conversion from the triangular mesh to a face. The

.stl files created from visualization software (e.g. CTAn, ScanIP), generally do not have surface mesh elements which are of a high quality. Third party software (e.g. Mimics from Materialise) is required to increase the quality of the elements. If Comsol is not able to create faces from the entire mesh, an error message is displayed that the importation was not entirely successful. Comsol is also able to import solid models (e.g. IGES and STEP) which are slightly superior to surface models, as well as volume mesh models (e.g. SFE from Simpleware).

3.3.6 Mesh Generation

3.3.6.1 Mesh Generation from Surface Models

Comsol Multiphysics has the ability to import three dimensional models that describe an object's surface. If the object can be successfully described in the Comsol environment the object may be meshed and solved. Table 3.4 shows the default mesh statistics of a small subsection (see Figure 3.29) from a typical three dimensional reconstruction. The mesh statistics of the .stl file is compared to the mesh statistics of the same volume meshed by Simpleware ScanFE.

Table 3.4: A comparison of the mesh properties between a model made from a stereolithographic file and a mesh made by ScanFE.

Property	Stereolithographic Mesh	ScanFE Mesh
Number of Elements	4167	2095
Degrees of Freedom	22951	12300
Minimum Element Quality	0.0325	0.0802
Element Volume Ratio	2.41×10^{-6}	0.0085
Faces formed by Comsol	69	11
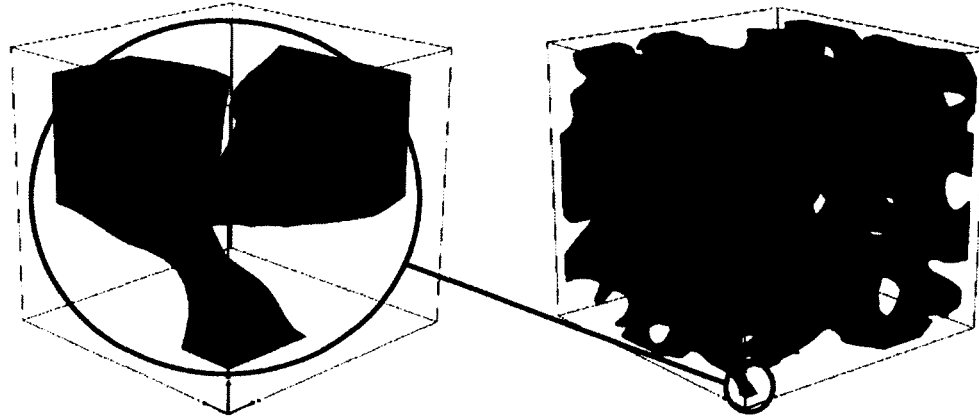
Figure 3.29: Maximum size of a mesh generated from an .stl file compared to a typical 3D reconstruction used in the study.

Comsol does have the capability to optimize the mesh created from the .stl file, however the additional gain in mesh quality and size is negligible. The reconstruction shown in Figure 3.29 shows the maximum size of a successful .stl importation in comparison to the typical size of a flow or diffusion simulation. The values shown in Table 3.4 also reflect the problems associated with meshing a surface model. Dramatic increases in the number elements used and the associated degrees of freedom are apparent, as well as inferior element quality and element volume ratio. The higher the element quality (essentially a ratio of the volume over the sum of the edge lengths), the greater the possibility that the mesh will not negatively affect the outcome of the simulation. Comsol states that the minimum element quality should be preferably above 0.1. The volume ratio is the minimum element volume divided by the maximum element volume.

3.3.6.2 Mesh Generation in Third Party Software

The software ScanFE from Simpleware was used to generate the final element mesh for this study (Fourie et al., 2007). The reconstructed volume is meshed based on an orthotropic grid intersected by interfaces defining the boundaries. In effect a base

Cartesian mesh of the whole volume, defined by the sampling rate, is tetrahedralised at boundary interfaces, based on cutting planes defined by interpolation points. Smooth boundaries are obtained by adjusting the interpolation points in one, or a combination, of two ways: by setting points to reflect partial volumes or by applying a multiple material anti-aliasing scheme. The process results in either a mixed tetrahedral/hexahedral mesh or a pure tetrahedral mesh and incorporates an adaptive meshing scheme.

The adaptive meshing scheme preserves the topology but reduces the mesh density where possible towards the interior of the mesh by agglomerating hexahedra into larger hexahedra and generating transitional tetrahedra. The approach is fully automated and creates smooth meshes with low element. The approach adopted allows for an arbitrary number of different volumes to be meshed. As neighboring sub-domains share a common cutting surface, this ensures a node to node correspondence at the boundaries between different meshed volumes, thus trivially satisfying the geometrical constraints at the boundary.

ScanFE exports the mesh as an .mphtxt file which is a text file containing information on the nodes and elements. It also contains information on which boundary elements should be combined to form a boundary or face. Initial versions of ScanFE incorrectly grouped the boundary elements and manual editing of this text file had to be done to ensure useful operation. In the .mphtxt the boundary information starts with the line:

tri domains – number of elements

and ends with the line:

tri domains end

The values in between these two lines of code determine to which boundary an element is grouped to. If the grouping of the boundaries is incorrect, these lines can be replaced by:

.

```
# tri domains – number of elements
0
# tri domains begin
# tri domains end
```

This will force Comsol to determine the boundary groupings based on angle of the neighboring elements. Each file typically contains more 1,000,000 lines of code and hence this procedure was not optimal. However, subsequent releases of ScanFE corrected the problem.

The export of more than one sub-domain is supported, though it was not used regularly in this study. For visualization purposes it was necessary at times to create and import separate sub-domains for the void space and for the porous medium. An example is shown in Figure 3.30. This procedure is however computationally expensive, due to the large increase in number of elements.
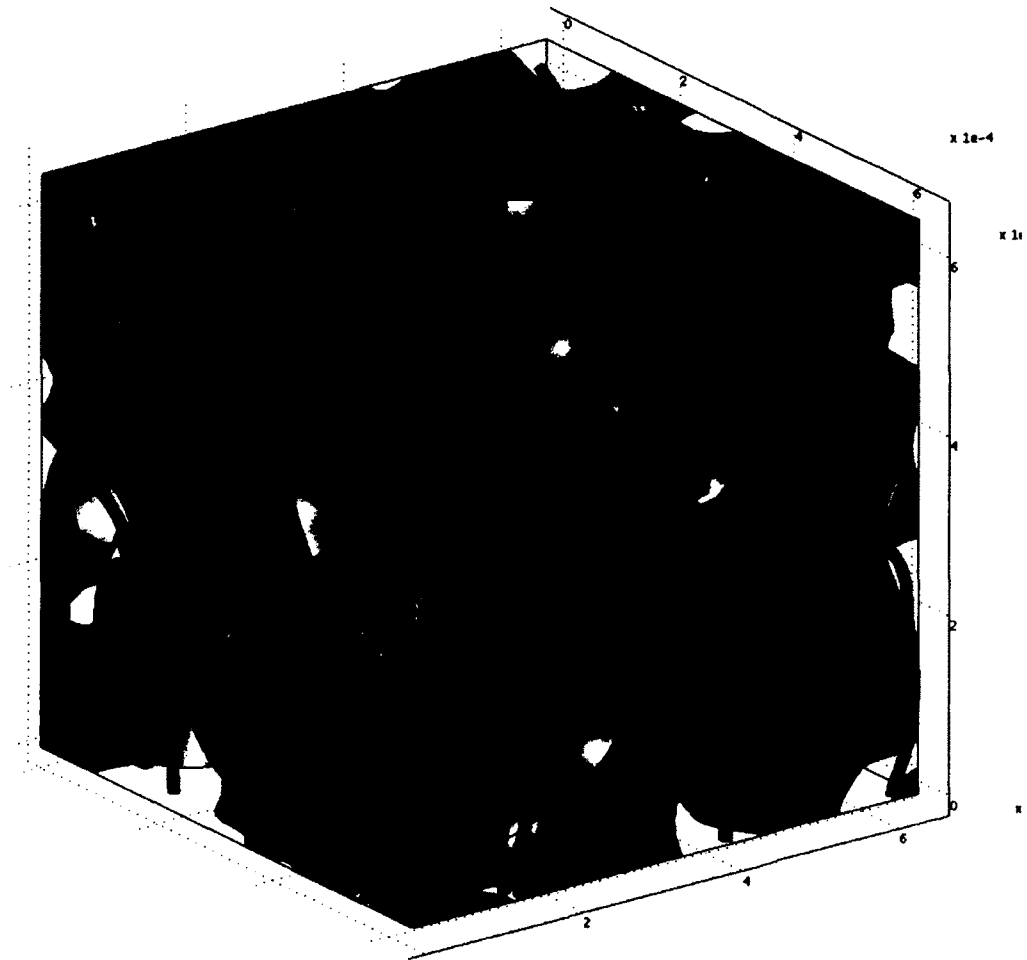
Figure 3.30: Particle trace through the large pored ceramic disk. The gray area is the consolidated particles and the blue tubes represent the diffusional paths as calculated through a particle trace operation. In this simulation both void space and the porous medium was imported as separated sub-domains. This enables the visualization of both the particle trace and the solid porous medium.

the porous medium was imported as separated sub-domains. This enables the visualization of both the particle trace and the solid porous medium.

Comsol only accepts the importation of an all tetrahedra mesh. Thus even though ScanFE is capable of generating a mixed hex-tet mesh, which could possible reduce the number of elements, this option is not available. The exported mesh also only consists of linear elements, though the order of the elements can be adjusted once importation is completed.

3.4 Laboratory Experiments

3.4.1 Hydraulic Conductivity

The hydraulic conductivity of the samples was measured through the falling head test procedure as laid out in the ASTM (2006). In this case the falling head method is preferred to the constant head method as the experimental setup is easier. The accuracy of the falling head procedure for coarser grained soils will not be compromised as long as sufficient head is available. In this regard the hydraulic conductivity measurements were collected for repeated soil packings and repeat measurements were taken on each separately packed soil. The final head reading was taken before the head reached zero.

The hydraulic conductivity is then determined through Equation (3.4).

$$K = \frac{A_t L}{A_c t} \ln \frac{h_0}{h}$$ (3.4)

Where K   =   Hydraulic conductivity [cm/s]

L   =   Sample length [cm]

h_0 =   initial head in the burette [cm]

h   =   final head in the burette [cm]

t   =   time taken to reach final head [t]

A_t =   Cross sectional area of the burette [cm^2]

A_c =   Cross sectional area of the soil sample [cm^2]

3.4.2 Through-diffusion

Through-diffusion tests were conducted on the consolidated porous media. The porous disks used were all 10 cm in diameter and varied between 6.6 and 12.7 mm thick. Iodide, as potassium iodide (KI), was used as the conservative tracer. The disks were placed between two cells, Figure 3.31, the source cell containing the conservative tracer and the receiving cell containing an equal density balance of potassium nitrate. The iodide concentrations in the receiving cell were measured with ion chromatography. The experimental methods, chemical analyses and uncertainty analyses of the through-diffusion tests are described in thorough detail in Benning & Barnes (2009).
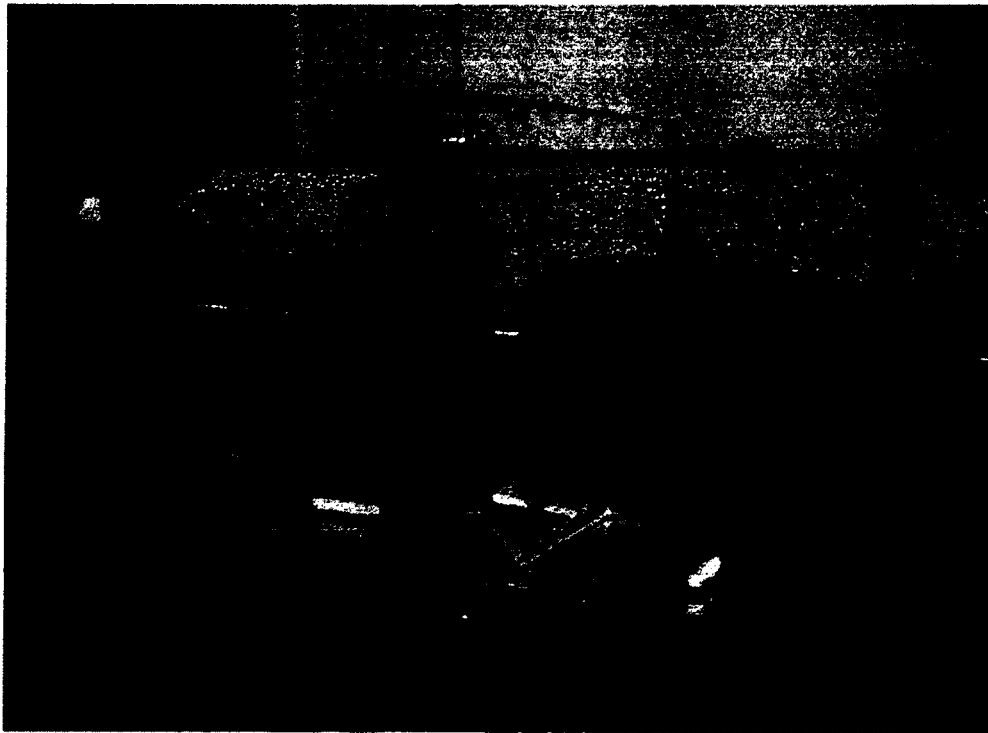
Figure 3.31: Experimental setup for the through-diffusion tests on the consolidated porous media.

3.5 Experimental Parameters Summary

3.5.1 Hydraulic Conductivity

The soil used in the study was a coarse sand with a mean particle diameter of 0.55 mm and the scans were conducted at resolutions varying from 2.3 to 4.3 μm. In order to determine at which resampling resolution to conduct the experiments, a mesh resolution study was done. Four separate samples were analyzed at decreasing resolutions and were all resampled from an original 3.88 μm scan. A summary is shown in Figure 3.32 and the tabular form is given as reference in Table 3.5. The matrix plot shows the pixel size, sample cube side length (thus an indication of total sample size) and the porosity. The axes are defined by the labels and units on the diagonal. Thus in the upper left hand graph the y-axis is Pixel size (tick marks from 0 to 40) and the x-axis is the Cube side length (tick marks 0.2 to 0.4). The other axes are similarly appointed.
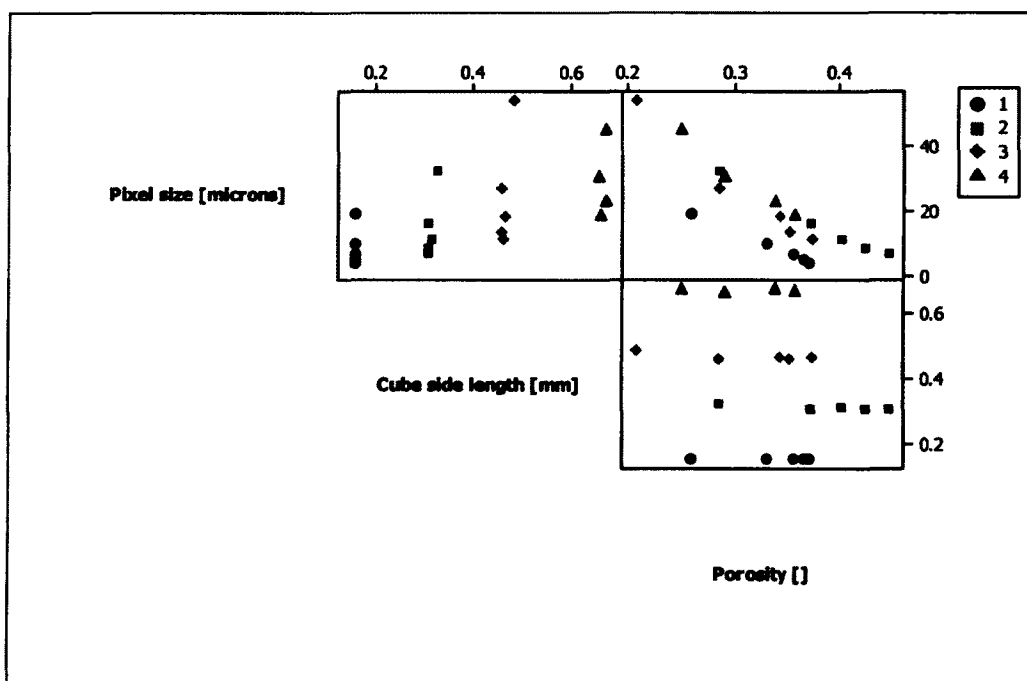
Figure 3.32: Matrix plot of mesh resolution study.

Table 3.5: Data to determine the optimum resampling resolution.

	Resampling	Pixel size	Hydraulic conductivity	Side Length	Porosity
		um	cm/s	mm	
Sample 1	100%	3.88	0.0118	0.155	0.372
Unresampled	80%	4.85	0.0126	0.155	0.366
	60%	6.47	0.0126	0.155	0.356
	40%	9.70	0.0120	0.155	0.329
	20%	19.40	0.0076	0.155	0.258
Sample 2	100%	6.47	0.0375	0.307	0.445
New baseline 60%	80%	8.08	0.0348	0.307	0.424
	60%	10.78	0.0356	0.313	0.403
	40%	16.17	0.0347	0.307	0.373
	20%	32.33	0.0191	0.323	0.286
Sample 3	100%	10.78	0.0246	0.464	0.374
New baseline 60x60%	80%	13.47	0.0234	0.459	0.354
	60%	17.96	0.0277	0.468	0.342
	40%	26.94	0.0217	0.459	0.285
	20%	53.89	0.0361	0.486	0.209
Sample 4	100%	17.96	0.0268	0.665	0.358
New baseline 60x60x60%	80%	22.45	0.0269	0.674	0.337
	60%	29.94	0.0165	0.659	0.291
	40%	44.91	0.0109	0.674	0.250

Four samples were generated from the original scan at 3.88 microns. Each consecutive sample was resampled at 60% of the preceding resolution, which enabled a larger sample

size. Thus sample 2's baseline was at 6.47 microns, which was 60% of the original 3.88 microns. This enabled a larger sample of 0.307 x 0.307 x 0.307 mm^3 vs. the original 0.155 x 0.155 x 0.155 mm^3. The same analogy applies to samples 3 and 4. The laboratory measured hydraulic conductivity was 0.028 cm/s and the porosity was 0.36. The resampling should therefore not deviate from these actual values. Sample 1, the black dots, has a very small volume and is probably not representative. This can be seen by the very low hydraulic conductivity. Sample 2, the red squares, has a very large porosity and a high hydraulic conductivity. This sample was deemed to be an outlier due to these anomalies. Sample three, the green diamonds, has a hydraulic conductivity and a porosity in the right range, but deviates below a resampling of 17.96 um. Sample 4, the blue triangles, also has a hydraulic conductivity and porosity in the right range, but deviates when resampled beyond 22.45 um. A general observation from the matrix plot is that the porosity decreases as the pixel size increases. This is expected as at a lower resolution there is more averaging and loss of data. All four samples overlap in the region where the porosity is 0.34 – 0.38 which is in the same region as the measured porosity value of 0.36. The corresponding pixel size is between 6.5 and 17.9 μm. At larger pixel sizes the porosity seems to be adversely affected and hence it was decided to limit the resampling in the study to 17.9 μm. It may be argued that scanning at a high resolution of sub 5 μm and resampling to 17.9 μm defeats the purpose and unnecessarily introduces long processing times. The following will explain why it is necessary to scan the highest resolution possible. Figure 3.33 shows the modeled hydraulic conductivity as a function of the initial scanning resolution.
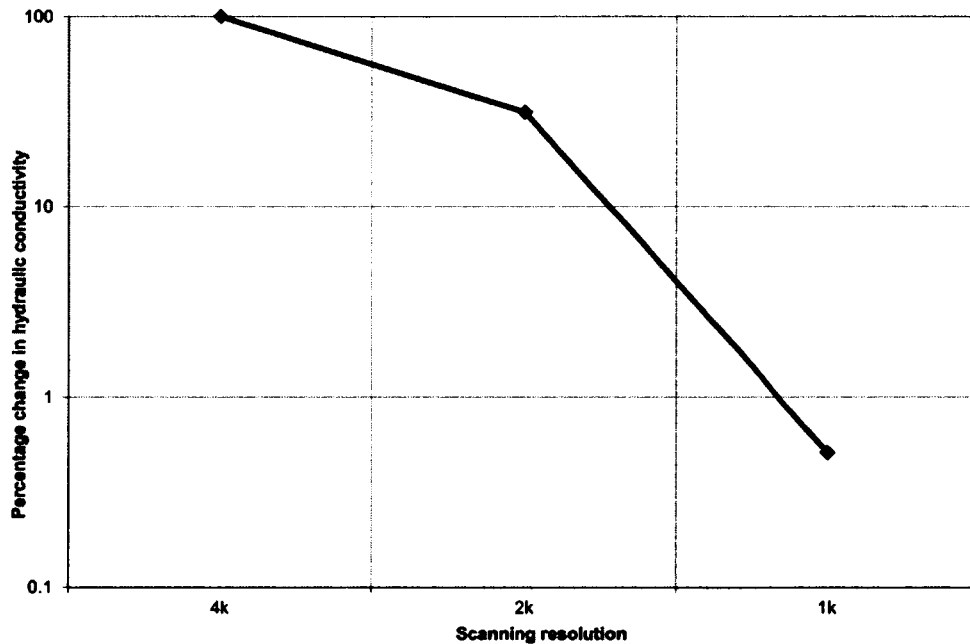
Figure 3.33: Percentage change in hydraulic conductivity as a function of the scanning resolution.

In constructing the data for Figure 3.33, the sample was scanned at 4k (3.45 μm), 2k (6.9 μm) and 1k (13.8 μm) settings and segmented under the exact same conditions. This resulted in dramatic decreases in predicted hydraulic conductivity in the 2k and 1k analyses. When a high resolution scan is resampled, the mask that delineates the pore space is resampled together with the background image. In this way the total volume of the pore space is largely retained. In a low resolution scan, the grey values of the pixels are affected by the low resolution (the partial volume effect) and which negatively impacts on the calculated void volume.

Ten separate samples were analyzed, with an average size of 0.32 mm^3. A typical cross section of the sample is shown in Figure 3.34, the image is approximately 1mm across.
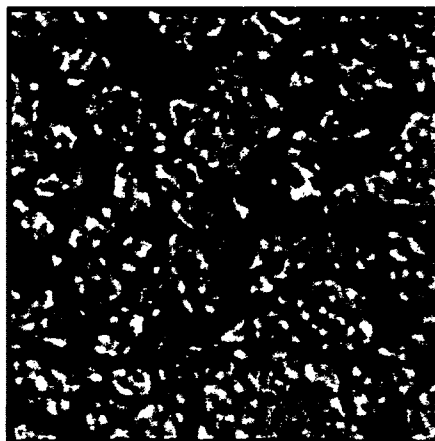
Figure 3.34: Typical cross section of the coarse sand used in the study. The image is approximately 1 mm across. Lighter areas show particles and darker areas the void space.

The available void space and the soil particles were found by applying a floodfill thresholding operation to the background images. The pore space derived from the resampled particles was then converted into a finite element volume mesh with ScanIP and imported into Comsol. The models had between 200,000 and 300,000 elements.

In Comsol, the Incompressible Navier-Stokes equations were used to model the fluid flow through the pore space. The density and viscosity of water were used to describe the fluid and a pressure gradient of 0.1 Pa/sample length was established as the boundary condition in the direction of fluid flow. The other fluid boundaries were specified as symmetry boundaries and the sand grain surfaces were specified as a wall (no-slip condition). Once a stationary solution was calculated the fluid flow was integrated across the in- and outflow boundaries and substituted into the Darcy equation to determine the hydraulic conductivity.

3.5.2 Diffusion

Three different porous media were selected for the study. Two of the media were manufactured ceramic disks (sourced by Refractron Technologies Corporation) and one was natural sandstone (translucent Novaculite). The material was scanned at a resolution of 2 μm with a SkyScan 1172 x-ray CT scanner and reconstructed with the proprietary software provided by the vendor. Typical reconstructed cross sections of the plates are shown in Figure 3.35. The scanned resolution is at least an order of magnitude higher than the mean pore diameter (Table 4.6). If a normal cumulative distribution function (CDF) is constructed with the same mean and standard deviation of each of the pore size distributions (Figure 4.9), the 2 micron resolution limit of the scanner intersects the CDF at 0.6% for the ceramic discs and 1.2% for the sandstone. This indicates that only 0.6% and 1.2% of the pore space in the respective discs could not be resolved by the scanner. The accuracy of the method is therefore very high.

(a)   (b)   (c)
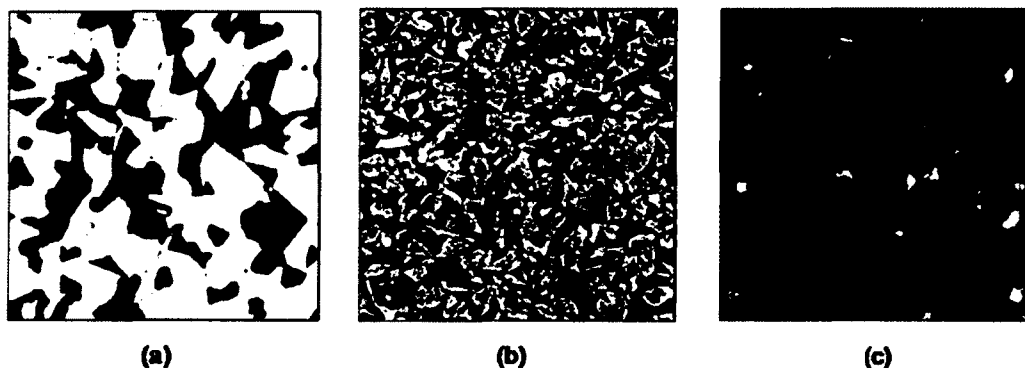
Figure 3.35: The three porous media selected for the experiment. (a) and (b) are the manufactured ceramic disks and (c) is the sandstone. The cross sections are all about 1mm wide. The lighter colors indicate a higher x-ray absorption and is therefore interpreted as the grains. The darker colors represent the pore space.

The reconstructed slices were rendered into a three dimensional object through a floodfill algorithm (provided by Simpleware). The floodfill algorithm seeds within the

advective/diffusive pore space and only allocates voxels into the three dimensional model that are adjacent to existing voxels. In this manner only the pore space that effectively contributes to advection or diffusion is incorporated into the model. Hence when the porosity is calculated from the volume of this model, it represents the effective porosity, φ_e, and not the total porosity. The reconstructed volumes varied from 0.02 mm^2 to 0.27 mm^2. Subsequently, the three-dimensional reconstructed representation of the void space was discritized into a finite element mesh and imported into Comsol. Between 300,000 and 600,000 elements were used for each model.

The hydraulic tortuosity was estimated by applying a pressure gradient across the void space and the fluid flow was solved with the Navier-Stokes equations. The diffusive tortuosity was estimated by applying Fick's Law and a concentration gradient across the void space. In both cases, a particle trace operation with the same seed points was used to calculate the tortuosity, through equation (2.3). An average of 49 seed points was used per sample to determine the tortuosity. The pore size distribution for each of the samples was calculated through a sphere-packing algorithm, and the connectivity of the pore space was assessed by calculating the fragmentation index of the void space (Hahn et al., 1992; SkyScan, 2008). The porosity of each porous material was measured both by the water saturation method on the bulk samples prior to conducting the through-diffusion experiments and through the CT reconstruction method described previously.

The through-diffusion tests were conducted on the three porous plates using iodide as a conservative tracer. All of the porous plates samples used were 10 cm in diameter and varied between 6.6 mm and 12.7 mm in thickness. The source cell was initiated with between 200 and 500 mg/l of KI and the receiving cell was balanced with an equal density of KNO$_3$. The water temperatures were kept constant at 25°C and both the source and receiving cells were constantly stirred using magnetic stir bars. The iodide concentrations were measured via ion chromatography, with calibration checks using internal and external standards performed routinely. The method detection limit for

iodide was 0.5 mg/L. Approximately 10% of the total samples were collected in replicate and when sample concentrations were above the linear calibration range, dilutions were performed in triplicate. The experimental methods, chemical analyses and uncertainty analyses of the through-diffusion tests are described in thorough detail in Benning & Barnes (2009).

4 Results and Discussion

4.1 Hydraulic Conductivity

The results of this study have been partially published (Fourie et al., 2007). These results have been referenced several times, including the exact modeling approach and parameters (Koivu et al., 2009; Narsilio et al., 2009; Piller et al., 2009; Koivu, 2010; Narsilio et al., 2010a; Narsilio et al., 2010b; Ovaysi & Piri, 2010; Smolarkiewicz & Winter, 2010).

Table 4.1 shows the hydraulic conductivities calculated from the Comsol models and the value obtained by conducting permeability tests in the laboratory (ASTM, 2006).

Table 4.1: Results summary of the hydraulic conductivities through simulation and in the laboratory.

	Hydraulic conductivity [cm/s]	
	Mean	Standard Deviation
Comsol model	0.028	0.006
Laboratory test	0.025	0.0008

The modeling results show a hydraulic conductivity that is approximately equal to the laboratory test results, thus indicating that the results from Darcy's Law in a coarse grained medium can be obtained by modeling with the Navier-Stokes equations. The small difference between the results can be attributed to a number of experimental errors

such as entrapped air in the permeameter, or a slight difference in packing density between the permeameter and the scanned sample. These results compare well against the results of Elliot et al. (2010), where CT generated results and laboratory results differed by more than an order of magnitude. Elliot scanned soil cores which contained clay sized particles at 20 µm resolution. As explained in Section 2.2, this may have negatively affected his results.

A sensitivity analysis with regards to the pressure difference of the boundary conditions was carried out. Figure 4.1 shows that the boundary conditions have very little influence on the calculated hydraulic conductivity. Five orders of magnitude change in the pressure at the boundary only changes the hydraulic conductivity at the fourth significant figure.
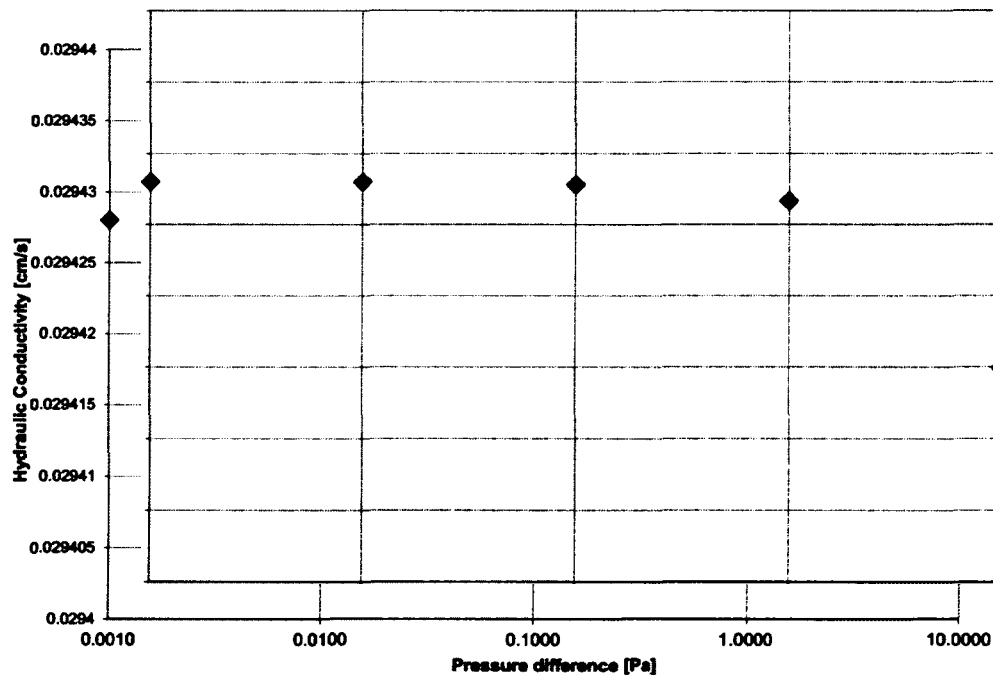
Figure 4.1: Hydraulic conductivity as a function of the boundary condition.

Figure 4.2 shows the effect of a change in boundary condition on the Reynolds number. As expected a linear relationship exists within the laminar flow range.
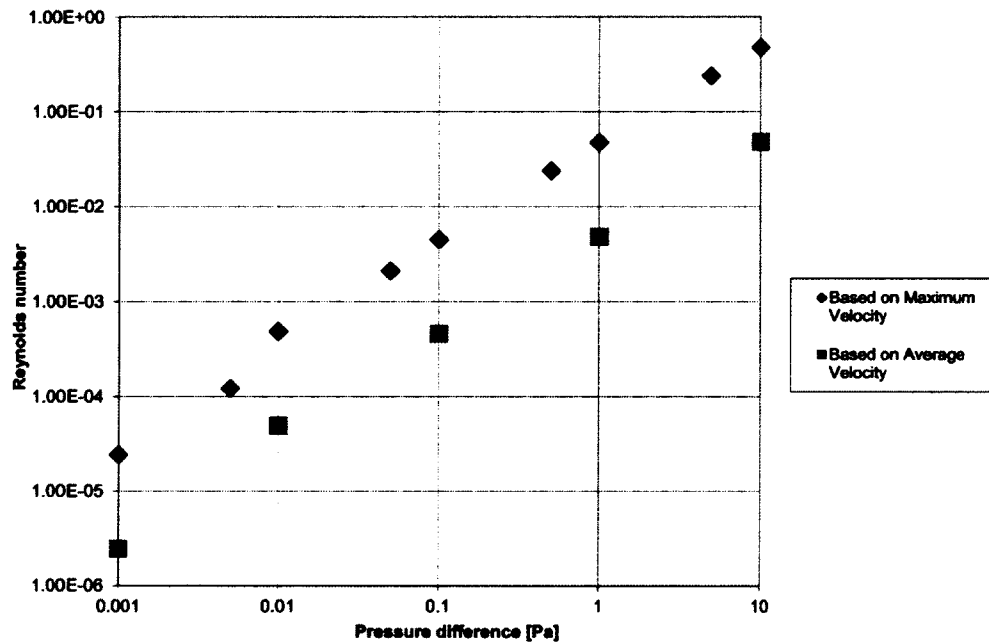
Figure 4.2: Linear relationship of the Reynolds number on the pressure difference imposed on the boundaries.

Figure 4.3 shows a probability plot of the specific surface area of the samples.
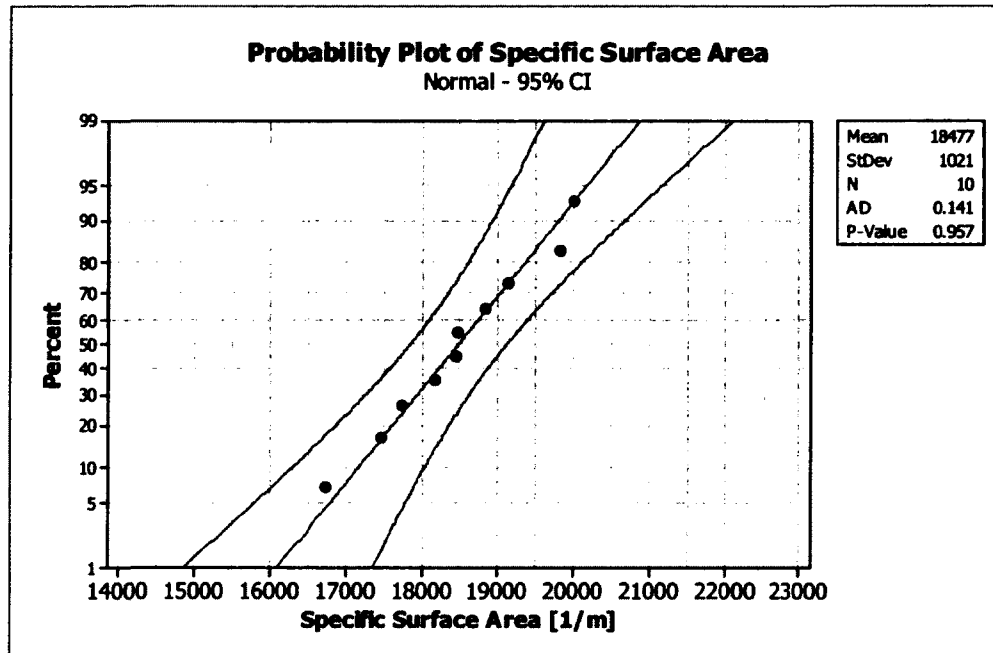
Figure 4.3: A probability plot of the specific surface areas of the samples. The data points lie within the 95% confidence limits, and therefore the distribution is normal.

The samples have a mean of 18,477 m^{-1} with a standard deviation of 1,021 m^{-1}. The data points lie within the 95% confidence limits and the p-value is > 0.05, which indicates that this is a normal distribution. This is a good indication that the data set contains samples representative of the whole. If the sample volumes were too small, the specific surface area could have changed dramatically from one sample to the other. For example, in the mesh resolution study described in Section 3.5.1, 'Sample 1' analyzed volumes of around 0.0037 m^3, which is two orders of magnitude less than those calculated for the final results. The average specific surface values calculated from these samples were 35,042 m^{-1}, which is a lot higher than the mean.

4.1.1 Kozeny-Carman equation

A structural explanation of Darcy's Law was first introduced by Kozeny in 1927 and was followed by numerous other explanations of varying complexity (e.g. Fair & Hatch, 1933; Hoffmann & Hoffman, 1992; Sperry & Peirce, 1995; Barr, 2001; Vervoort & Cattle, 2003). The Kozeny-Carman equation is still used ubiquitously to determine the hydraulic conductivity due to its ease of use, though several parameters have to be estimated. It is interesting to see whether this almost century-old approximation to calculate a soil's hydraulic conductivity holds true, now that the technology is available to directly calculate the parameters that previously had to be estimated. The Kozeny-Carman equation is given in Section 2.2.2 equation (2.7), which is based on Poiseuille's law and takes into account the wetted perimeter, or hydraulic radius (Carman, 1937):

$$k = c_o \frac{\phi_e^3}{\tau_h^2 M_s^2 (1 - \phi_e)^2}$$

Note that M_s is the specific surface area in relation to the solid volume, not the porous media volume (as shown in Figure 4.3). The Kozeny constant, c_0, is ill defined in the literature, but accounts for the geometrical shape of the pore channels and varies from 0.5 – 0.667. In this study a value of 0.5 was assumed. The porosity and specific surface area can be directly calculated from the three dimensional representation of the void space and the tortuosity is calculated from a particle trace operation. For these samples both the tortuosity and the porosity show a normal distribution, as shown in Figure 4.4 and Figure 4.5. The results of the Kozeny-Carman equation are shown in Figure 4.6 and parameters are shown in Table 4.2.
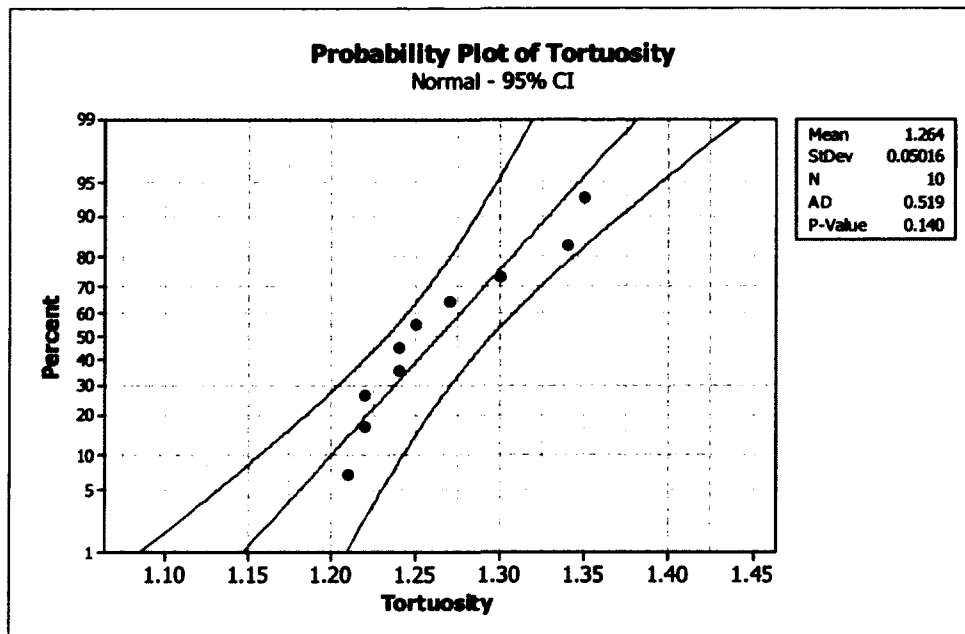
Figure 4.4: Probability plot of the tortuosity, showing a normal distribution.
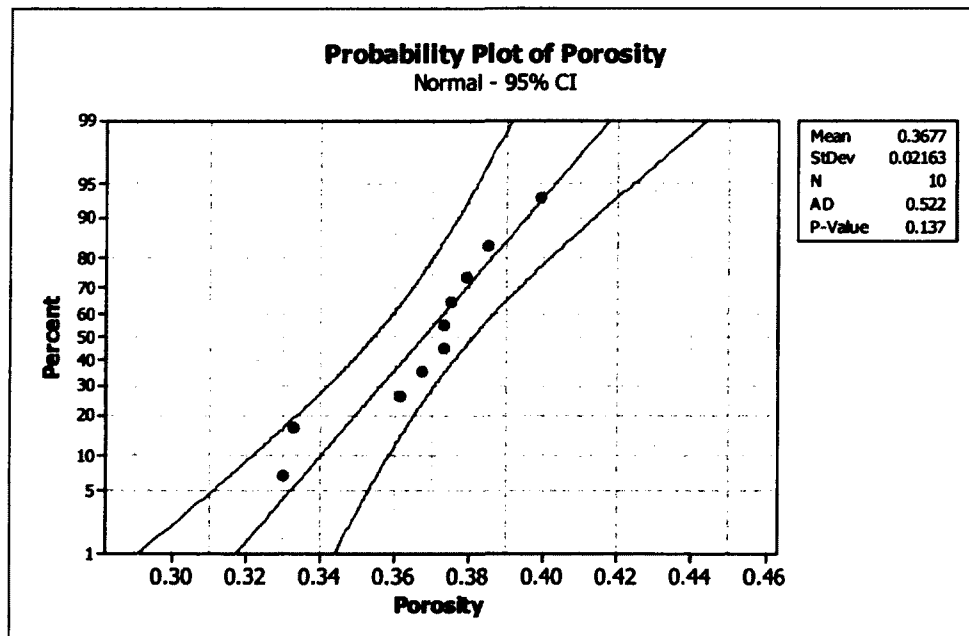
Figure 4.5: Probability plot of the porosity, showing a normal distribution.
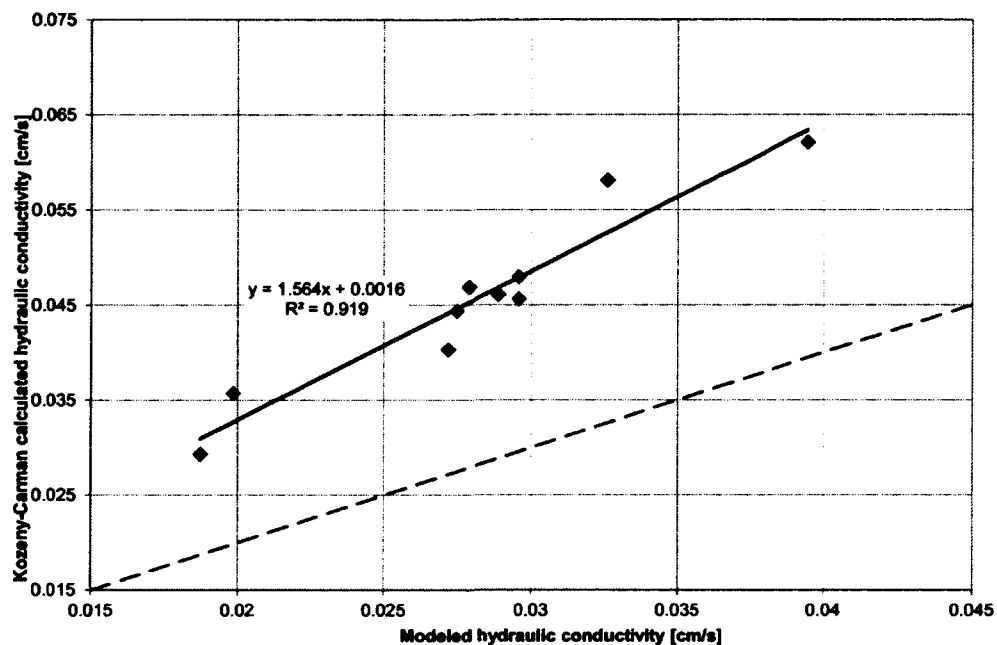
Figure 4.6: A comparison of the hydraulic conductivities calculated by the Kozeny-Carman equation and those calculated in Comsol.

The results are highly correlated with each other, with the Kozeny-Carman equation slightly over predicting the modeling results with 12.5%.

Kozeny's approximation neglects the velocity components normal to the general direction of flow (Bear, 1972). However as can be seen in Figure 4.7, even in this small sample the convergence and divergence of flow occurs, which decreases the hydraulic conductivity of the soil. Hence is it is logical that the Kozeny-Carman equation over predicts the hydraulic conductivity.
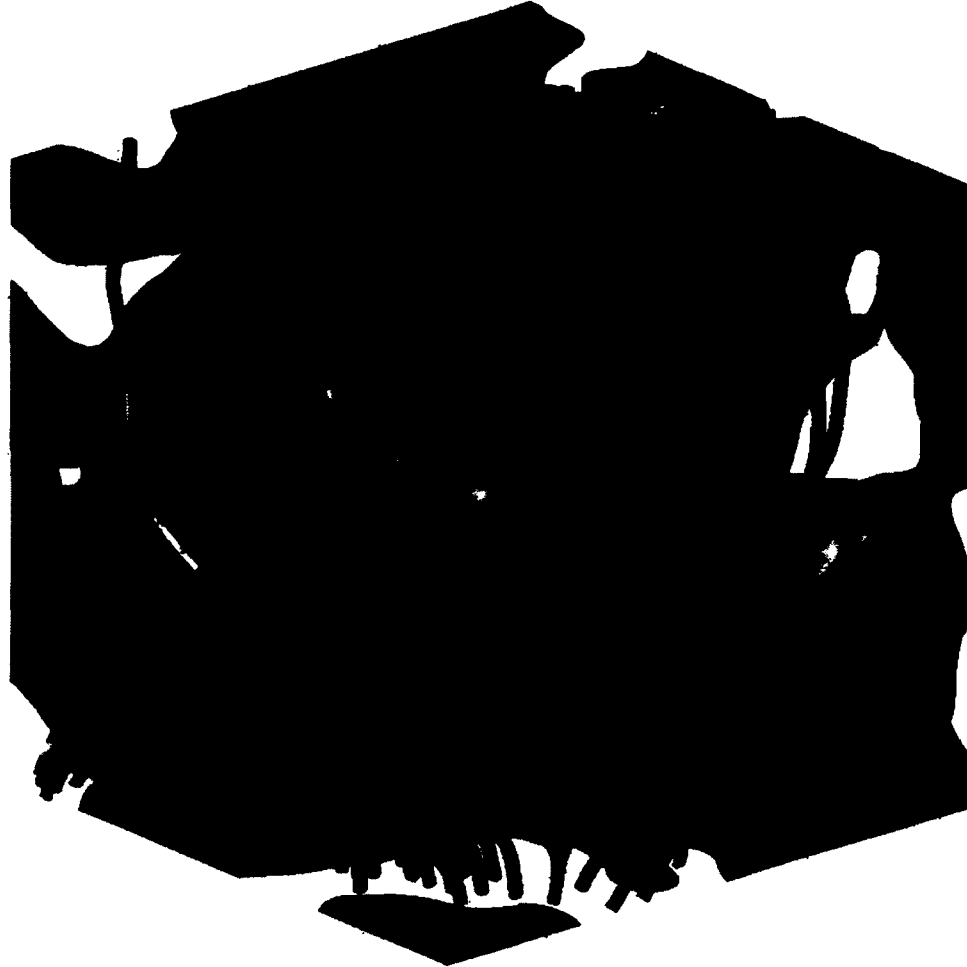
Figure 4.7: A particle trace plot super imposed on the soil sample. Warmer colors indicate longer travel times. The convergence and divergence of stream lines are apparent.

4.1.2 Parameter Analysis

An analysis of the individual parameters of the Kozeny-Carman equation is shown in Table 4.2.

Table 4.2: Parameter analysis of the Kozeny-Carman equation

	Average	Standard Deviation	SD Average%	Correlation coefficient against % Difference
Porosity	0.368	0.021	5.6	0.985
Tortuosity	1.26	0.048	3.8	0.014
Specific surface area	29256	1874	6.4	0.031
$\dfrac{\phi^3}{(1-\phi)^2}$	0.127	0.028	21.7	0.749
$\dfrac{1}{\tau^2}$	0.63	0.046	7.2	0.007
$\dfrac{1}{M_s^2}$	1.18×10^{-9}	1.5×10^{-10}	12.5	0.014
Kozeny-Carman Hydraulic Conductivity	0.0456	0.0061	20	
Comsol Hydraulic Conductivity	0.0281	0.0056	19.8	
% Difference between Kozeny-Carman and Comsol	62.46			

From Table 4.2 the following observations can be made:

  o The Kozeny-Carman equation predicts the hydraulic conductivity at 62% higher than the Comsol model.

o Of the individual parameters, (Porosity, Tortuosity and the Specific surface area), the Specific surface area shows the largest individual variation, with a Coefficient of Variation of 6.4. Note that this does not mean that it necessarily contributes the most to the variation in the hydraulic conductivity.

o Due to the formulation of the Kozeny-Carman equation, the porosity term, ($\frac{\phi^3}{(1-\phi)^2}$), has the largest individual variation, with a Coefficient of Variation of 21.7.

o In the last column it shows the correlation coefficient, (p-value), of each term as analyzed in a regression against the percentage difference between the two predictive methods. The tortuosity shows the highest correlation and the specific surface area is also significant. There is no correlation between the porosity and the difference between the two models, with a p value >> 0.05.

4.1.2.1 Tortuosity

The tortuosity term, which shows the highest correlation in the difference between the two models, is an important part of the prediction and it is appropriate to analyze previous approximations of the tortuosity. Table 4.3 shows empirical predictions of the tortuosity and their comparison to the Comsol generated results.

Table 4.3: Comparison between tortuosities calculated by the Navier-Stokes simulation and empirical predictions.

	Equation	Tortuosity	% Difference
Comsol		1.26	-
Carman (1937)	$\tau = \sqrt{2}$	1.41	11.55
Millington & Quirk (1961)	$\tau = \dfrac{1}{\phi^{1/3}}$	1.4	10.43
Mota et al. (2001)	$\tau = \dfrac{1}{\phi^{0.4}}$	1.47	18.05
Weissberg (1963)	$\tau = 1 + 0.5(1 - \phi)$	1.32	4.13
Boving & Grathwohl (2001)	$\tau = \dfrac{1}{\phi^{0.2}}$	1.22	-3.36
Dias et al. (2008)	$\tau = \dfrac{1}{\phi^{0.5}}$	1.65	30.47

In this case the approximation by Boving and Grathwohl provided the closest answer to the calculation derived from the Navier-Stokes model. It does however have to be noted that the use and derivation of the tortuosities showed in Table 4.3 do not strictly adhere to the definition of hydraulic tortuosity (see Section 2.2.2). For example, Dias et al. (2008), whose work concerns fluid flow, references Weissberg (1963), who was concerned with diffusion, who in turn references the Maxwell equations, which was concerned with electrical conductivity!

4.1.2.2 Specific Surface Area

Aubertin et al. (2005) describes the "fundamental equation" for hydraulic conductivity as a function of three factors:

$$K = f_f f_v f_s \tag{4.1}$$

where f_f is a function of the fluid properties, f_v is a function of the void space, and f_s is a function of the solid grain surface characteristics. In the Kozeny-Carman equation, f_s is described by the specific surface area of the media. Incorporation of the specific surface area in the prediction of the hydraulic conductivity has been attempted by several authors, apart from Carman, e.g. Barr (2001), Chapuis & Aubertin (2003) and Carrier (2003), though invariably some simplifying assumption is made about the shape of the particle (mostly spherical). The other option for f_s is to include a function that describes the particles themselves, such as with the Hazen equation (1911)

$$k = c d_{10} \tag{4.2}$$

where c is either a constant dependent on soil type (Shepherd, 1989), or a function of the fluid and void properties (Mbonimpa et al., 2002). The parameter d_{10} is the 10 percent passing diameter on the grain size distribution curve. The Kozeny-Carman can also be adapted into this form (Bear, 1972)

$$k = \frac{d_{50}^2}{180} \frac{\phi^3}{(1-\phi)^2} \tag{4.3}$$

Note that in Equation (4.3) the terms associated with the tortuosity and the specific surface area have been lumped together. If this equation is used to estimate the hydraulic conductivity, an answer of 0.21 cm/s is found, which is almost an order of magnitude beyond the Comsol and laboratory results.

The physical understanding of including the specific surface area in the Kozeny-Carman equation is that retardation of the fluid occurs at the particle boundary due to shear forces. The coefficient of variation of the specific surface area (shown in Table 4.2) is the largest of the three parameters, but does not necessarily mean that it is the cause of the largest variation in the hydraulic conductivity. The cause of variability in the hydraulic conductivity can be assessed by Monte Carlo analysis or by Numerical Differentiation.

4.1.2.3 Monte Carlo Analysis

Monte Carlo analysis involves the random variation of input variables and discerning the output variation as a function of the input variation. In practice this can be implemented in a spreadsheet through the following steps:

1. Create a column of normally distributed random numbers for the first variable (in this case the porosity), with the average and standard deviation of the actual data. For this simulation 5,000 lines were used.

2. Keep the other variables (Specific Surface Area and Tortuosity) at the average values and calculate the hydraulic conductivity for each combination of Porosity, Specific Surface Area and Tortuosity.

3. Take the absolute difference between consecutive values of the porosity and divide by consecutive values of the difference in hydraulic conductivity. This gives the ratio of the input and output variation.

4. Find the maximum ratio.

5. Do steps 1-3 for the other variables.

6. Compare the ratios.

The maximum ratios found are summarized in Table 4.4.

Table 4.4: Comparison of ratios of change in hydraulic conductivity as a function of a change in the input variable, as well as their comparative ratios.

	Porosity	Tortuosity	Specific Surface Area
Maximum ratio	0.854	0.101	5.23×10^{-6}
Porosity /	1	8.45	163,289
Tortuosity /	0.12	1	19,312
Specific Surface Area /	6.16×10^{-6}	5.18×10^{-5}	1

From Table 4.4 it is apparent that the porosity has the largest influence on the magnitude of the hydraulic conductivity as calculated by the Kozeny-Carman equation. It is interesting to note that the Specific Surface Area has almost no influence in this regard. This is unexpected as it defies the physical understanding of hydraulic conductivity and, on inspection of the Kozeny-Carman equation; it is raised to the same power as the Tortuosity.

The result can however be explained as follows:

o In the value range of the Tortuosity (~1.26), the change in the function value of $1/x^2$ is much higher that in the range of the Specific Surface Area (~29,256). Figure 4.8 shows this graphically.
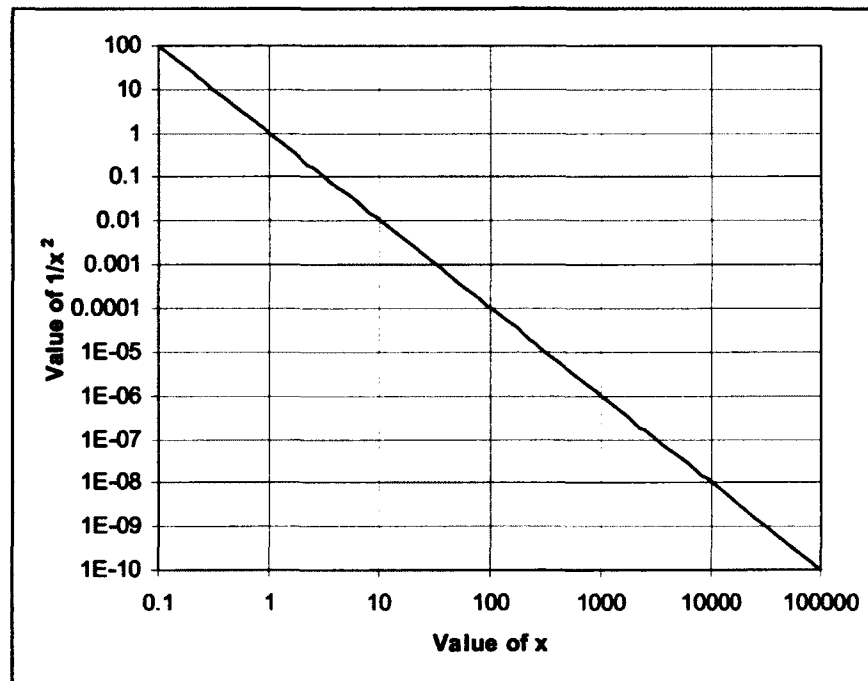
Figure 4.8: The output of Tortuosity and Specific Surface Area formulation as a function of the input.

o   The experiments were conducted on only one type of medium, a coarse sand. This leads to a narrow specific surface area distribution, as shown in Figure 4.3. If more types of media were tested, the result may have been different, since the variation in specific surface area may have been a lot larger.

4.1.2.4   Numerical Differentiation

The result obtained in Section 4.1.2.3 can also be checked via numerical partial differentiation of the Kozeny-Carman equation. The following procedure is followed:

1.   Create a three-dimensional grid containing the three variables, one in each principle vector direction, ranging from the smallest to largest value found in the Comsol model. Each variable is divided into 30 steps. Calculate the hydraulic

conductivity for each of the coordinates. This gives a three-dimensional structure of 27,000 data points.

2. Vary the porosity by an arbitrary small value, δ, and keep the tortuosity and specific surface at their original value. Calculate the hydraulic conductivity from this adjusted three dimensional grid, and compare it to the original value through

$$\frac{f(\phi,\tau,M_s)-f(\phi+\delta,\tau,M_s)}{\delta}$$

3. Repeat step 2 for the Specific Surface Area and Tortuosity. This gives three sets of 27,000 data points.

4. Find the maximum value in each of the data sets.

Table 4.5 shows the result of the numerical differentiation

Table 4.5: Results of the numerical partial differentiation showing the maximum values obtained, as well as their comparative ratios.

	Porosity	Tortuosity	Specific Surface Area
Maximum ratio	0.907	0.138	6.30×10^{-6}
Porosity /	1	6.56	144,135
Tortuosity /	0.15	1	21,957
Specific Surface Area /	6.94×10^{-6}	4.55×10^{-5}	1

The results of the numerical differentiation closely mirror the results of the Monte Carlo simulation. The small difference can be attributed to the difference in the discretization of the two studies. The maximum values are found where the porosity is at is maximum value, and the tortuosity and specific surface area are at their minimum. This is also in accordance with the physical understanding of hydraulic conductivity.

4.1.2.5 Parameter Summary

In summary, it can be concluded that although the porosity of the sample has the biggest influence on the magnitude of the hydraulic conductivity as calculated by the Kozeny-Carman equation, it is the tortuosity and the specific surface area that determine the accuracy of the hydraulic conductivity, as compared to the answer derived by the Navier-Stokes simulation and the laboratory result. There is also a large difference between the values directly calculated for the tortuosity and those estimated by empirical equations found in literature.

4.2 Diffusion

4.2.1 Analysis of Porous Media

For each of the media, at least three different finite element simulations were conducted to assess the tortuosities and all of the other measured parameters were calculated from at least two different sub samples from each of the porous media. A summary of the average values of these measurements are shown in Table 4.6. The mean pore diameter was calculated from the pore size distribution illustrated in Figure 4.9. The constrictivity is treated in the literature as the idealized ratio between the pore body cross sectional area and the pore constriction cross sectional area (e.g. Petersen, 1958). However, in real life there is a range of pore body sizes, and the pore constrictions tend to zero, as can be seen in Figure 4.9. Thus there is no regular pore body and pore constriction of which the ratio can be taken. The numbers for the constrictivity in Table 4.6 were calculated by taking the 95th percentile at the large pore range and dividing it by the 5th percentile at the small pore range. This would give a quantitative relationship to the range of pore sizes and the calculated values also fall within the theoretical range (1 to 5) that was explored by Petersen.

Hahn et al. (1992) developed a methodology to quantify the connectivity of trabecular bone, by relating the amount of convex to concave surfaces within the three dimensional geometry. A lot of concave surfaces indicate a large connectivity and a lot of convex surfaces indicate a poorly connected lattice. This is measured by taking the ratio of the area and perimeter before and after a morphological dilation operation. This methodology is applied to the study media and is summarized in Table 4.6 where a larger connectivity value indicates a more disconnected pore space in the porous medium. It is important to note at this stage, that the connectivity is not included in the analysis to rule out those pores which will not add to transport, as the disconnected pores have already been accounted for in the model preparation. Pores that are completely disconnected from the main pore body were eliminated in the creation of the three dimensional model through the floodfill algorithm, as explained previously. Thus, connectivity in this sense relates to how the pore structure deviates from the capillary bundle theory and is an indication of how the "bundles" inter-connect, or converge and diverge. Figure 4.10 shows an example of a typical result of the particle trace operation, and how these diffusion paths interconnect.

Table 4.6: Mean pore scale values derived from the CT scans and calculated by the FEA models. The values in brackets are the standard deviation.

	Ceramic Disk (Small Pores)	Ceramic Disk (Large Pores)	Sandstone
Porosity	0.37	0.41	0.16
Hydraulic Tortuosity	1.54 (0.28)	1.47 (0.24)	1.85 (0.64)
Diffusive Tortuosity	1.43 (0.17)	1.28 (0.18)	1.68 (0.37)
Mean Pore Diameter [μm]	29	61	21
Constrictivity	3.48	4.64	4.44
Connectivity	0.0050	0.0096	0.060
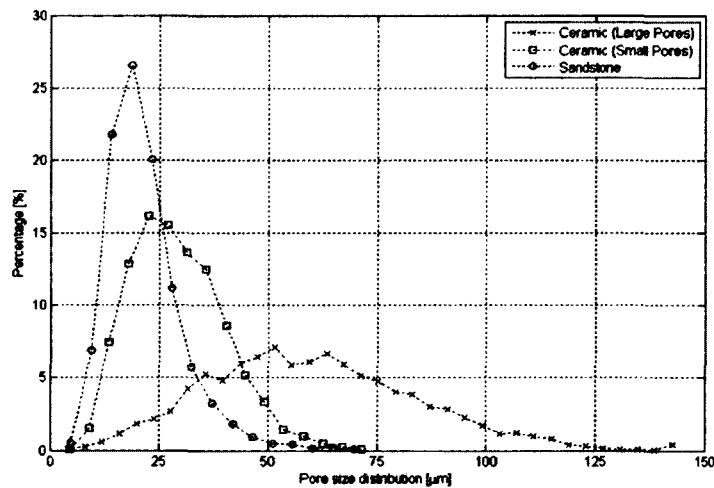
Figure 4.9: Pore size distribution of the three media as calculated by a sphere packing algorithm. The minimum pore size is the minimum resolution of the scan conducted on the porous media.
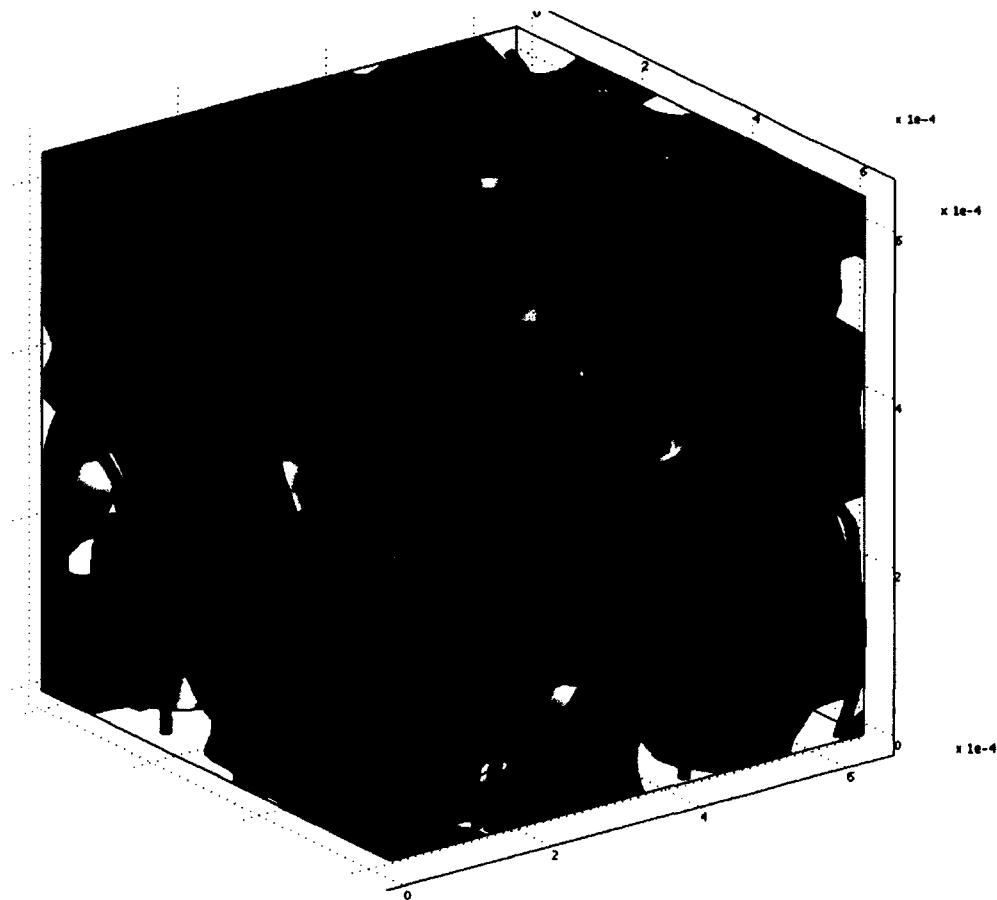
Figure 4.10: Particle trace through the large pored ceramic disk. The gray area is the consolidated particles and the blue tubes represent the diffusional paths as calculated through a particle trace operation.

4.2.2 Comparison to Through-diffusion Experiments

A semi-analytical solution, as presented by Moridis (1999), was applied to the conditions of the through-diffusion experiments for the comparison of the experimental data to the predictions based on the parameters measured by the CT methods. Four cases were modeled for each porous media to allow comparisons of the various theoretical applications of the tortuosity: each calculated tortuosity, the diffusive and the

hydrodynamic (as shown in Table 4.6), was applied to the first and second power, as in equations (2.2) and (2.5). A temperature-corrected molecular diffusion coefficient was used for iodide (Benning & Barnes, 2009). The CT-measured porosity was included in the semi-analytical solution model for predicted diffusive transport. No explicit allowance was made for the constrictivity, since, by nature, the inclusion of this term in literature has been empirical, rather than principle-based. The modeled solutions for these four different cases for each of the porous media is compared to the through-diffusion experimental data, as illustrated in Figure 4.11 through Figure 4.13. The residual sum of squares (RSS) between the calculated results of the four models and the experimental data are shown in Table 4.7.
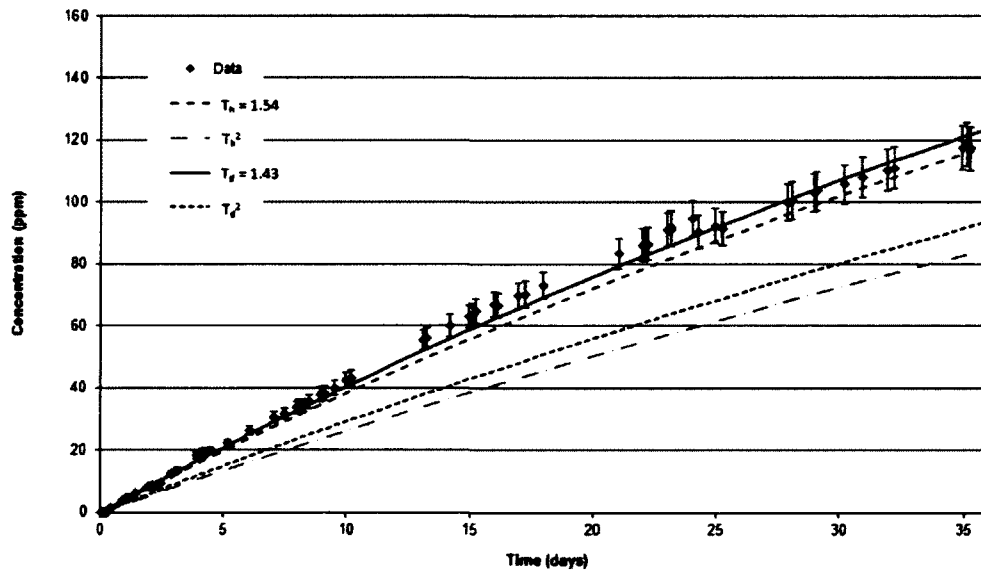
Figure 4.11: Through-diffusion results for the ceramic disk (small pores). The experimental data is plotted against the semi-analytical solution for the four different interpretations of tortuosity.
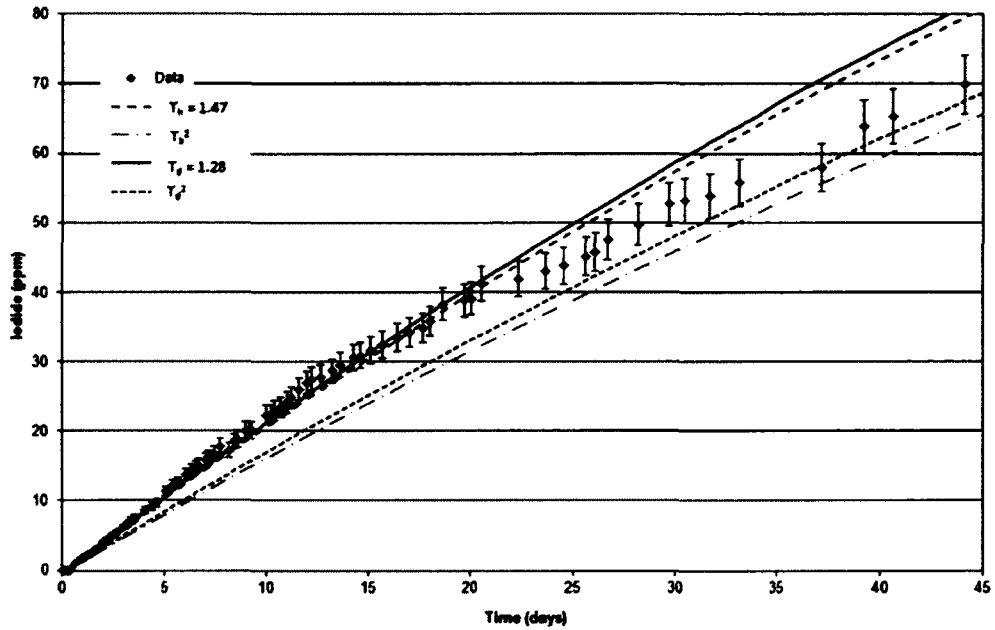
Figure 4.12: Through-diffusion results for the ceramic disk (large pores). The experimental data is plotted against the semi-analytical solution for the four different interpretations of tortuosity.
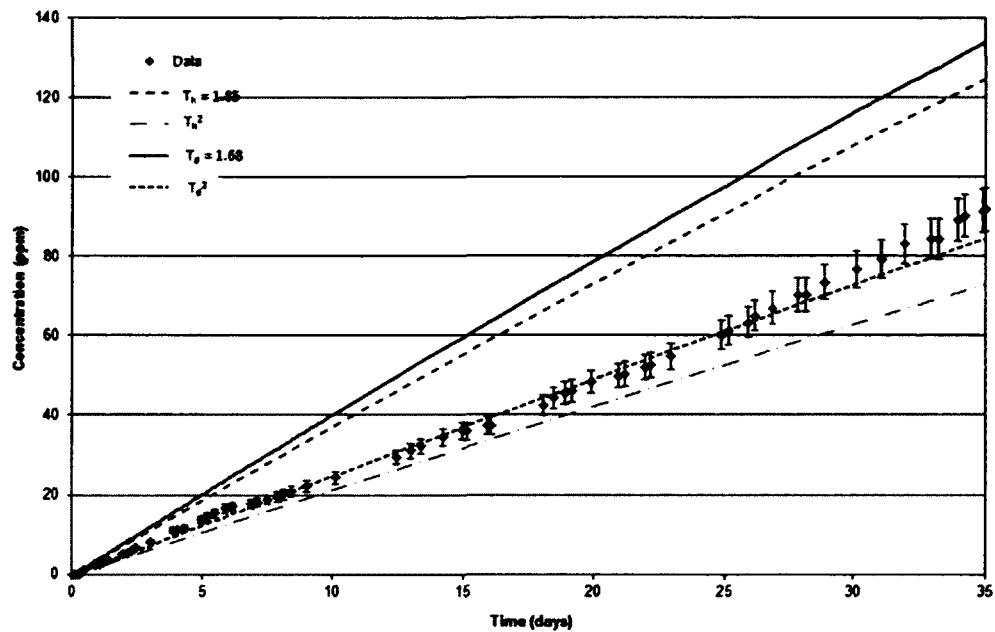
Figure 4.13: Through-diffusion results for the sandstone. The experimental data is plotted against the semi-analytical solution for the four different interpretations of tortuosity.

Table 4.7: The residual sum of squares calculated from the experimental results and the predicted receiving cell concentration. The smallest value in each column is highlighted in bold.

Intrinsic Diffusion Coefficient Used	Ceramic Disk (Small Pores)	Ceramic Disk (Large Pores)	Sandstone
$D_i = D_m \dfrac{\theta_e}{\tau_d}$	**1.189 x 10⁻³**	**3.523 x 10⁻³**	1.067 x 10⁻²
$D_i = D_m \dfrac{\theta_e}{\tau_d^2}$	5.402 x 10⁻³	6.25 x 10⁻²	**9.997 x 10⁻⁵**
$D_i = D_m \dfrac{\theta_e}{\tau_h}$	3.758 x 10⁻³	8.399 x 10⁻³	6.913 x 10⁻³
$D_i = D_m \dfrac{\theta_e}{\tau_h^2}$	8.656 x 10⁻²	2.66 x 10⁻²	9.885 x 10⁻⁴

The semi-analytical model, with parameters obtained from x-ray CT, adequately predicted the experimental results obtained from the through diffusion tests, as can be seen in Figures 3 through 5. For the most part, the predicted values fall within the expected experimental error, as determined in Benning & Barnes (2009).

Referring to Table 4.6, the particle trace operations, as calculated by Fick's Law and the Navier-Stokes equations, show hydrodynamic and diffusional tortuosities that differ between 5 and 13%. In all cases, the hydrodynamic tortuosity is larger than the diffusional tortuosity. This result is in accordance with Clennell's conceptual explanation of the difference between these tortuosities (Clennell, 1997). Also, the use of the diffusional tortuosity in the intrinsic diffusion coefficient always gives a lower residual sum of squares (RSS) than its corresponding intrinsic diffusion coefficient calculated with the hydrodynamic tortuosity. This result provides a strong indication that, not only

do the diffusional and hydrodynamic tortuosities differ in magnitude, but that they should not be used interchangeably. Thus, when Fick's Law is applied, the diffusional tortuosity should be used and when the Navier Stokes equations and its derivates (such as Darcy's Law) are applied, the hydrodynamic tortuosity should be used. Prior to these investigations, Clennell's theoretical approach had not been experimentally validated.

For both of the ceramic disks, the RSS's indicate that the model fit to experimental data is better if tortuosity enters the equation to the first power, rather than squared. In contrast, a comparison of the model fit to experimental data for the sandstone indicates an improved fit when the tortuosity enters the diffusion equation to the second power. On examination of the porous media characteristics in Table 4.6, it is found that the small-grained ceramic disk and the sandstone physically resemble one another, to a reasonable degree, with regards to the tortuosity, mean pore diameter and constrictivity. However, the porosities and connectivities of these two media differ greatly. In the derivation of the intrinsic diffusion coefficient, the most common building block is to assume that the porous medium is a bundle of unconnected capillary tubes (e.g. Kozeny, 1927). However, as can be seen in Figure 4.14 there is divergence and convergence of the imaginary capillary tubes. Bear (1972), for example, acknowledges this fact and points out that it is one of the pit falls of the current application of Kozeny's original theorem. In the sandstone, the relatively large number for the connectivity indicates that the pore space is significantly less connected than the two other samples, thus more closely approximating Kozeny's capillary bundle theorem. In contrast, the small pored ceramic disk has a connectivity value an order of magnitude smaller than the sandstone, which indicates that it is highly connected. This large degree of divergence and convergence invalidates e.g. Epstein's argument (1989) that the tortuosity should always enter the equation squared. For the ceramic disks, the application of the tortuosity to the first power to the predicted intrinsic diffusion coefficient showed a better fit to the experimental data (Equation 4), while for the sandstone sample, the application of the tortuosity squared in the equation for the intrinsic diffusion coefficient provided a better fit (Equation 1).

The large-grained ceramic disk has a connectivity value between that of the sandstone and the small-grained ceramic disk, and as shown in Table 4.6, the experimental data at longer times deviates towards the tortuosity-squared model line. Though this may be due to unexamined influences, it may be entirely possible that a family of applicable curves exist between the τ and τ^2 lines, as supported by Winsauer et al.'s experimental results (1952) where he found a best fit with $\tau^{1.67}$. One explanation for this could be that at short times, the highly connected pore space in the medium need to obtain a concentration equilibrium between the larger and smaller pores. Once this time-dependent equilibrium has been established, the larger pores will preferentially diffuse all the molecules and hence these pores will become less connected and the porous medium will approach the ideal capillary bundle theorem. As the current implementation of the intrinsic diffusion coefficient is built on the assumption that there is no divergence and convergence of diffusional pathlines, it seems logical that the connectivity, which in these measurements reflects the relative degree of convergence/divergence in the media, has a significant effect on the power to which the tortuosity is raised.
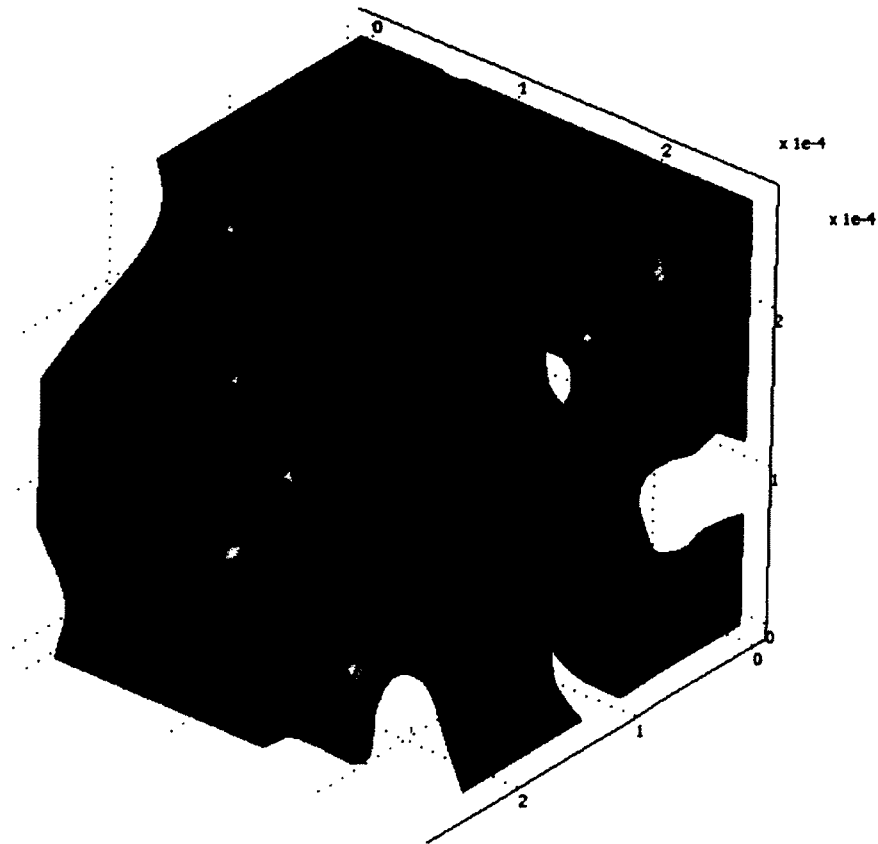
Figure 4.14: A subsection of the porous medium shown in Figure 4.10, with three diffusional paths superimposed on the internal medium structure. The convergence and divergence of the diffusional paths are apparent.

As previously mentioned, no specific allowance was made for the constrictivity in the calculation of the intrinsic diffusion coefficient. The accurate prediction of the experimental results suggests that the constrictivity, at least for the case in the relatively coarse-grained porous media examined, does not play a significant role in diffusion. For the small-grained media, in which the size of the pore spaces is closer to the size of the diffusing molecules, a diffuse double-layer effect may however increase the importance of the constrictivity on the intrinsic diffusion coefficient (Appelo & Wersin, 2007). It is

noted, however, that the calculation of the constrictivity here is also somewhat arbitrary; it could just as well have been determined as the ratio of the 90th percentile to the 10th percentile. However, it does give a quantitative measurement of the conceptual understanding of constrictivity and allows a comparison of the three porous media.

5 Conclusions and Recommendations

Broadly speaking, the results from this study show that the micro scale analysis of porous media allows the calculation of macro scale parameters in coarse porous media. The recent advent of micro computed tomography allows the digitization and non-destructive examination of samples. This visualization determines the internal geometry of a sample, and the digitization there of, that other methods, such as serial sectioning, does not allow. However, the mere visualization of in the internal geometry, all though insightful, does not promote a higher level of understanding of the macro scale behavior of the sample. It is only when the geometry is converted into a finite element mesh, and analyzed mathematically, that conclusions can be drawn with respect to the sample's macro scale behavior.

X-ray computed tomography was used to visualize the internal geometry of the unconsolidated coarse porous media. Important variables that had to be controlled, were the

- o Particle density
- o Particle size distribution
- o Particle vibration

Coarse silica sand gave good adsorption and contrast, and the particle size distribution was of such a nature that the error induced by scanning at <10 micron resolution was minimal. The vibration of the particles was minimized by introducing water at residual amounts. A floodfill algorithm insured that only the connected pore space was segmented, and smoothing and resampling kept the model to a manageable size.

The pore space of the coarse grained media was analyzed with finite element analysis, using the Comsol software package and it's built in Navier-Stokes application mode. The quality of the mesh proved to be most important factor to obtain a model that could be solved. Third party software by Simpleware was used for this purpose. Mesh statistics such as the Minimum Element Quality and the Element Volume Ratio, was superior to

the importation of surface models, and allowed much larger volumes to be analyzed. Flow was induced through a pressure difference at the boundaries. A mesh resolution study showed that the scans should be conducted at the highest resolution possible, and may then be resampled to 17.9 µm without negatively affecting the modeling results. The imposed boundary condition to induce flow, the pressure, could be varied over 5 orders of magnitude without negatively affecting the modeling results.

The hydraulic conductivity measured by the Navier-Stokes equations was only 12.5% higher than that calculated by laboratory-scale tests. Analysis of the parameters of the Kozeny-Carman equation delivered the following results:

- o The hydraulic conductivity estimated by the Kozeny-Carman equation was 62% higher than the prediction from the Navier-Stokes model.

- o When the Kozeny-Carman is expressed in terms of the mean particle diameter, (substituting the tortuosity and the specific surface area with an assumed constant), the equation over-predicts the hydraulic conductivity with 740%.

- o The tortuosity and the specific surface area determine the accuracy of the hydraulic conductivity as calculated by the Kozeny-Carman equation, when compared to the answer derived by the Navier-Stokes simulation and the laboratory result.

- o Monte Carlo simulation and numerical derivation show that the porosity has the largest influence in determining the magnitude of the hydraulic conductivity as calculated by the Kozeny-Carman equation. The specific surface shows almost no influence on the magnitude of the hydraulic conductivity and this may be because only one sample material was used. For future work, it is recommended that more sample materials are tested to determine the influence of the specific surface area, as this more suits the physical understanding of flow retardation in porous media.

- o Several empirical models are available to predict the tortuosity as a function of the porosity. Of these models, the equation by Boving and Grathwohl came the closest to the answer generated by the Navier-Stokes simulation.

X-ray computed tomography was also used to image the consolidated porous media. The consolidated porous media was easier to visualize than the unconsolidated porous media, and sandstone (translucent novaculite) and a sintered aluminum oxide showed good adsorption and contrast. The mean pore space size was also large enough to result in a very small error during the reconstruction.

As with the consolidated media, finite element analysis was used to impose Fick's law on the pore space geometry, and the same methodology was followed to maximize the mesh quality while minimizing the number of elements required. A concentration gradient was induced by a constant concentration at one boundary, and a constant flux at the opposite boundary. This mimicked the actual conditions in the laboratory cell. The parameters necessary to calculate the intrinsic diffusion coefficient was also measured:

- o Porosity
- o Tortuosity
- o Constrictivity
- o Connectivity

The intrinsic diffusion coefficient was determined as per literature based on the values determined from x-ray computed tomography and finite element analysis. The semi-analytical solution of Fick's law was then compared to the laboratory results and good comparisons were found with 6% error up to 35 days for the sandstone and the small grained ceramic disk. The large grained ceramic disk started to show a deviation from the modeled result at 20 days.

The results from the study indicate that the diffusional tortuosity and the hydrodynamic tortuosity differ in magnitude, and that they can not be used interchangeably, since:

o The ceramic disks showed the closest prediction to the laboratory results when the diffusional tortuosity is used, rather than the hydrodynamic tortuosity, and when it enters the equation to the first power.

o The sandstone showed the closest prediction to the laboratory results when the diffusional tortuosity is used, and when it enters the equation to the second power.

The results can be explained by observing that the connectivity between the ceramic disks vary greatly, in that the ceramic disks have a high pore connectivity, while the sandstone show a low pore connectivity. The sandstone therefore more closely conform to the idealized derivation of the intrinsic diffusion coefficient based on the capillary bundle theorem.

6 References

Agyare, W.A., Park, S.J. and Vlek, P.L.G., (2007). Artificial neural network estimation of saturated hydraulic conductivity, *Vadose Zone Journal*, 6, (2), 423-431.

Appelo, C.A.J. and Wersin, P., (2007), Multicomponent diffusion modelling in clay systems with application to the diffusion of tritium, iodide and sodium in opalinus clay, *Environmental Science and Technology*, 41, (14), 5002-5007.

ASTM D2434-68, (2006), Standard Test Method for Permeability of Granular Soils.

Aubertin, M., Chapuis, R.P., Mbonimpa, M. and Barr, D.W., (2005), Discussion of "Goodbye, Hazen; Hello, Kozeny-Carman", by W. David Carrier III, *Journal of Geotechnical and Geoenvironmental Enigneering*, 131, (8), 1054-1058.

Barr, D.W., (2001), Coefficient of permeability determined by measurable parameters, *Groundwater*, 39, (3) 356-361.

Bear, J., (1972), *Dynamics of Fluid in Porous Media*. New York: American Elsevier Publishing Company.

Benning, J.L. and Barnes, D.L., (2009), Comparison of modelling methods for the determination of effective porosities and diffusion coefficients in through-diffusion tests, *Water Resources Research*, 45, (9), 1-11.

Boving, T.B. and Grathwohl, P., (2001), Tracer diffusion coefficients in sedimentary rocks: correlation to porosity and hydraulic conductivity, *Journal of Contaminant Hydrology*, 53, 85-100.

Bradbury, M.H. and Green, A., (1985), Measurement of important parameters determining aqueous phase difusion rates through crystalline rock matrices, *Journal of Hydrology*, 82, 39-55.

Brooks, A.N. and Hughes, T.J.R., (1982), Streamline upwind/Petrov-Galerkin formulations for convection dominated flows with particular emphasis on the incompressible Navier-Stokes equations, *Computer Methods in Applied Mechanics and Engineering*, 32, 199-259.

Brooks, R.A. and Chiro, G., (1976), Beam hardening in x-ray reconstructive tomography, *Physics in Medicine and Biology*, 21 (3), 390-398.

Carlson, W.D., Denison, C., Ketcham, R.A., (1999), High-Resolution X-ray computed tomography as a tool for visualization and quantitative analysis of igneous textures in three dimensions, *Electronic Geosciences*, 4, 3, 1-14

Carman, P.C., (1937), Fluid flow through granular beds, *Transactions of the Institute of Chemical Engineers*, 15, 150-156.

Carman, P.C., (1956), *Flow of Gasses Through Porous Media*. Butterworths Scientific Publications: London.

Carrier III, W.D., (2003), Goodbye, Hazen; Hello Kozeny-Carman, *Journal of Geotechnical and Geoenvironmental Engineering*, November, 1054-1056.

Chakraborty, D., Chakraborty, A., Santra, P., Tomar, R.K., Garg, R.N., Sahoo, R.N., Choudhury, S.G., Bhavanarayana, M., and Kalra, N., (2006), Prediction of hydraulic conductivity of soils from particle-size distribution, *Current Science*, 90, (11), 1526-1531.

Chapuis, R.P. and Aubertin, M., (2003), On the use of the Kozeny-Carman equation to predict the hydraulic conductivity of soils, *Canadian Geotechnical Journal*, 40, 616-628.

Chapuis, R.P., (2004), Predicting the saturated hydraulic conductivity of sand and gravel using effective diameter and void ratio, *Canadian Geotechnical Journal*, 41, 787-795.

Charbeneau, R.J., (1990), *Groundwater Hydraulics and Pollutant Transport*, Upper Saddle River: Prentice Hall.

Chiang, M.Y.M., Wang, X, Landis, F.A., Landis, F.A., Dunkers, J. and Snyder, C.R., (2006), Quantifying the directional parameters of structural anisotropy in porous media, *Tissue Engineering*, 12, (6), 1597-1606.

Chock, D.P., (1978), An advection-diffusion model for pollutant dispersion near roadways, *Journal of Applied Meteorology*, 17, July, 976-989.

Clennell, M.B., (1997), *Tortuosity: A Guide Through the Maze (Special Publication)*, 122, 299-344. London: Geographical Society.

Clough, R., (1965), The finite element method in structural mechanics, In: Stress Analysis, Chapter 7, edited by O.C. Zienkiewicz and G.S. Holister, John Wiley and Sons, Ltd., pp. 85-87, 1965.

Clough, R.W, (1990), Original formulation of the finite element method, *Finite Elements in Analysis and Design*, 7, 89-101.

Courant, R., (1943), Variational methods for the solution of problems of equilibrium and vibrations, *Bulletin of the American Mathematical Society*, 49, 1-43.

Cowin, S.C. and Mehrabadi, M.M., (1989), Identification of the elastic symmetry of bone and other materials, *Journal of Biomechanics*, 22, (6/7), 503-515.

Cronican, A.E. and Gribb, M.M., (2004), Hydraulic conductivity for sandy soils, *Groundwater*, 42, (3), 459-464.

Darcy, H., (1856), Les Fontaines Publiques de la Ville de Dijon, Victor Dalmont.

De Vries, G. and Norrie, D.H., (1971), The application of the finite-element technique to potential flow problems, *Journal of Applied Mechanics*, 38, (4), 798-802.

DeHoff, R.T., Aigeltinger, E.H. and Craig, K.R., (1972), Experimental determination of the topological properties of three-dimensional microstructures, *Microscopy*, 95, (1), 69-91.

Diamond, S., (1970), Pore size distributions in clays, *Clays and Clay Minerals*, 18, 7-23.

Dias, R.P., Fernandes, C.S., Teixeira, J.A., Mota, M. and Yelshin, A., (2008), Permeability analysis in bisized porous media: Wall effect between particles of different size, *Journal of Hydrology*, 349, 470-474.

Diersch, H.J., (1988), Finite element modeling of recirculating density-driven saltwater intrusion processes in groundwater, *Advances in Water Resources*, 11, 25-43.

Douglas, J. Jr. and Russell, T.F., (1982), Numerical Methods for Convection-Dominated Diffusion Problems Based on Combining the Method of Characteristics with Finite Element or Finite Difference Procedures, *SIAM Journal on Numerical Analysis*, Vol. 19, (5), 871-885.

Elliot, T.R., Reynolds, W.D., and Heck, R.J., (2010), Use of existing pore models and X-ray computed tomography to predict saturated soil hydraulic conductivity, *Geoderma*, 156, 133-142.

Ene, H.I., (1990), Application of the homogenization method to transport in porous media. In *Dynamics of Fluids in Hierarchical Porous Media*, ed. J.H. Cushman, 223-241. San Diego: Academia Press.

Epstein, N., (1989), On tortuosity and the tortuosity factor in flow and diffusion through porous media. *Chemical engineering Science*, 44, (3), 777-779.

Fair, G.M. and Hatch, L.P., (1933), Fundamental factors governing the streamline flow of water through sand, *Journal fo the American Water Works Association*, 25, (11), 1551-1565.

Fetter, C.W., (2001), *Applied Hydrogeology*, 4th Ed. Upper Saddle River: Prentice Hall.

Fitts, C.R., (2002), *Groundwater Science*. San Diego: Academic Press.

Fogler, H.S., (2005), *Elements of Chemical Reaction Engineering*, 4th Ed. Upper Saddle River: Prentice Hall.

Fourie, W.J., Said, R., Young, P. and Barnes, D.L., (2007), The simulation of pore scale fluid flow with real world geometries obtained from x-ray computed tomography, *Proceedings of the Comsol Conference*. Boston.

Garrels, R.M., Dreyer, R.M. and Howland, A.L., (1949), Diffusion of ions through intergranular space in water-saturated rocks, *Bulletin of the Geological Society of America*, 60, 1809-1828.

Gherboudj, I.A., Bernier, M., Hicks, F. and Leconte, R., (2007), Physical Characterization of Air Inclusions in River Ice, *Journal of Cold Regions Science and Technology*, 49, (3), 179-194.

Goldstein, L., Prasher, S. and Ghoshal, S., (2007), Three-dimensional visualization and quantification of non-aqeuous phase liquid volumes in natural porous media using a medical x-ray computed tomography scanner, *Journal of Contaminant Hydrology*, 93, 96-110.

Hahn, M., Vogel, M., Pompesius-Kempa, M. and Delling, G., (1992), Trabecular bone pattern factor – a new parameter for simple quantification of bone microarchitecture, *Bone*, 13, 327-330.

Hainsworth, J.M. and Aylmore, L.A.G., (1983), The use of computer-assisted tomography to determine spatial distribution of soil water content, *Australian Journal of Soil Research*, 21, (4), 435-443.

Hauke, G. and Hughes, T.J.R., (1994), A unified approach to compressible and incompressible flows Computer Methods in Applied Mechanics and Engineering, 113, 389-395.

Hazen, A., (1911), Discussion of "Dams on sand formations" by A.C. Koenig, *Transactions of the American Society of Civil Engineers,* (73), 199-203.

Heinrich, J.C., Huyakorn, P.S., Zienkiewicz, O.C. and Mitchell, A.R., (1977), An 'upwind' finite element scheme for two-dimensional convective transport equation, *International Journal for Numerical Methods in Engineering,* 11, 131-143.

Hoffmann, J.R. and Hoffman, P.A., (1992), Darcy's Law and structural explanation in hydrology, *Proceeding of the 1992 biennial meeting of the philosophy of science association,* 1, 22-35.

Hounsfield, G.N., (1973), Computerized transverse axial scanning (tomography). Part 1: Description of system, *British Journal of Radiology,* 46, 1013-1022.

Hrennikoff, A., (1941), Solution of problems of elasticity by the framework method, *Journal of Applied Mechanics,* December, 169-175.

Joschko, M., Müller, P.C., Kotzke, K., Döhring, W. and Larink, O., (1993), Earthworm burrow system development assessed by means of x-ray computed tomography, *Geoderma,* 56, 209-221.

Ketcham, R.A. and Iturrino, G.J., (2005), Nondestructive high-resolution visualization and measurement of anisotropic effective porosity in complex lithologies using high-resolution x-ray computed tomography, *Journal of Hydrology,* 302, 92-106.

Koivu, V., (2010). Analysis of fluid flow through porous media based on X-ray micro-tomographic reconstructions, Doctorial Thesis.

Koivu, V., Decain, M., Geindreau, C., Mattila, K., Bloch, J. and Kataja, M., (2009), Transport properties of heterogeneous materials. Combining computerized X-ray micro-tomography and direct numerical simulations, *International Journal of Computational Fluid Dynamics*, 23, (10), 713-721.

Kozeny, J., (1927), Über kapillare Leiting des Wassers in Boden, *Sitzungsberichte der Akademie der Wissenschaften, Wien*, 136, 271-306.

Landis, E.N., Nagy, E.N., Keane, D.T. and Nagy, G., (1999), A technique to measure three-dimensional work-of-fracture of concrete in compression, *Journal of Engineering Mechanics*, 125, 599-605.

Landis, E.N., Petrell, A.L., Lu, S., Nagy, E.N., (2000), Examination of pore structure using three-dimensional image analysis of microtomographic data, *Concrete Science and Engineering*, 2, 162–169.

Macdonald, I., Kaufmann, P. and Dullien, F., (1986), Quantitative image analysis of finite porous media II. Development of genus and pore map software, *Journal of Microscopy*, 144, (3), 277-296.

Mbonimpa, M., Aubertin, M., Chapuis, R.P. and Bussière, B, (2002), Practical pedotransfer functions for estimating the saturated hydraulic conductivity, *Geotechnical and Geological Engineering*, 20, 235-259.

McBroom, R.J., Hayes, W.C., Edwards, W.T., Goldberg, R.P. and White, A.A., (1985), Prediction of vertebral body compressive fracture suing quantitative computed tomography, *The Journal of Bone and Joint Surgery*, 67, 1206-1214.

Millington, R.J. and Quirk, J.P., (1961), Permeability of porous solids, *Transactions of the Faraday Society*, 57, 1200-1207.

Mooney, S.J. and Morris, C., (2004), Quantification of preferential flow in undisturbed soil columns using dye tracers and image analysis, *SuperSoil 2004: 3rd Australian New Zealand Soils Conference*, 1-7.

Moran, C.J., (1994), Image processing and soil micromorphology, In *Soil Micromophology: Studies in Management and Genesis*, ed. Rinrose-Voase, A. & Humpreys, G., Proceedings of the IX Internatiol Working Meeting on Soil Micromorphology, 459-482. Townsville: Australia.

Moridis, G.J., (1999), Semianalytical solutions for parameter estimation in diffusion cell experiments, *Water Resources Research*, 35, (6), 1729-1740.

Mota, M., Teixeira, J.A. Bowen, W.R. and Yelshin, A., (2001), Binary spherical particle mixed beds: porosity and permeability relationship measurement, *Transcations of the Filtration Society*, 1, (4), 101-106.

Narsilio, G.A., Buzzi, O., Fityus, S., Yun, T.S. and Smith, D.W., (2009), Upscaling of Navier-Stokes equations in porous media: Theoretical, numerical and experimental approach, *Computers and Geotechnics*, 36, 1200-1206.

Narsilio, G.A., Kress, J. and Yun, T.S., (2010a), Characterisation of conduction phenomena in soils at the particle scale: Finite element analyses in conduction with synthetic 3D imaging, *Computers and Geotechnics*, 37, 828-836.

Narsilio, G.A., Yun, T.S., Kress, J. and Evans, T.M., (2010b), Hydraulic and thermal conduction phenomena in soils at the particle-scale: Towards realistic FEM simulations, *IOP Conference Series: Materials Science and Engineering*, 10, 1-10.

Odgaard, A., (1997), Three-dimensional methods for quantification of cancellous bone architecture, *Bone*, 20, (4), 315-328.

Ovaysi, S. and Piri, M., (2010), Direct pore-level modeling of incompressible fluid flow in porous media, *Journal of Computational Physics*, 229, 7456-7476.

Petersen, E.E., (1958), Diffusion in a pore of varying cross section, *American Institute of Chemical Engineers Journal*, 4, (3), 343-345.

Petrovic, A.M., Siebert, J.E. and Rieke, P.E., (1982), Soil bulk density analysis in three dimensions by computed tomographic scanning, *Soil Science Society of America Journal*, 46, 445-450.

Pierret, A., Capowiez, Y., Belzunces, L. and Moran, C.J., (2002), 3D reconstruction and quantification of macropores using x-ray computed tomography and image analysis, *Geoderma*, 106, 24-271.

Piller, M., Schena, G., Nolich, M., Favretto, S., Radaelli, F. and Rossi, E., (2009), Analysis of hydraulic permeability in porous media: From high resolution X-ray tomography to direct numerical simulation, *Transport in Porous Media*, 80, 57-78.

Regalado, C.M. and Muñoz-Carpena, R., (2004), Estimating the saturated hydraulic conductvity in a spatially variable soil with different permeameters: a stochastic Kozeny-Carman relation, *Soil and Tillage Research*, 77, 189-202.

Ringrose-Voase, A.J., (1996), Measuremnet of soil macropore geometry by image analysis of sections through impregnated soil, *Plant and Soil*, 183, 27-47.

Rosenberg, E., Ferreira De Pavia, R., Gue'roult, P., Lynch, J., (1999), Micro tomography applications in rock analysis and related fields, *Computerized Tomography for Industrial Applications and Image Processing in Radiology*, Berlin, Germany, DGZfP-Proc. BB 67-CD.

Rüegsegger, P., Medici, T.C. and Anliker, M., (1983), Corticosteroid-induced bone loss. A longitudinal study of alternate day therapy in patients with bronchial asthma using

quantitative computed tomography, *European Journal of Clinical Pharmacology*, 25, 615-620.

Saripalli, K.P., Serne, R.J., Meyer, P.D. and McGraill, B.P., (2002), Prediction of Diffusion Coefficients in Porous Media Using Tortuosity factors Based on Interfacial Areas, *Groundwater*, 40, (4), 346-352.

Satterfield, C.N., (1970), *Mass transfer in heterogeneous catalysis*. Cambridge, MA: MIT Press.

Shefelbine, S.J., Simon, U., Claes, L., Gold, A., Gabet, Y., Bab, I., Müller, R. and Augat, P., (2005), Prediction of fracture callus mechanical properties using micro-CT images and voxel-based finite element analysis, *Bone*, 36, (3), Pages 480-488.

Shepherd, R.G., (1989), Correlations of permeability and grain size, *Groundwater*, 27, (5), 633-638.

Šimůnek, J., Vogel, T., and van Genuchten, M.T., (1992), The SWMS_2D code for simulating water flow and solute transport in two-dimensional variably saturated media, Version 1.1, *Research Report No. 126*, U. S. Salinity Laboratory, USDA, ARS, Riverside, CA.

Skagius, K. and Neretnieks, I., (1986), Porosities and Diffusivities of Some Nonsorbing Species in Crystalline Rocks, *Water Resources Research*, 22, (3), 389-398.

SkyScan, (2008), *Structural Parameters Measured by the SkyScan CT – Analyser Software*. SkyScan: Belgium.

Smith, S.L. and Brebbia, C.A., (1975), Finite-Element Solution of Navier-Stokes Equations for Transient Two-Dimensional Incompressible Flow, *Journal of computational physics*, 17, 235-245.

Smolarkiewicz, P.K. and Winter, C.L., (2010), Pores resolving simulation of Darcy flows, *Journal of Computational Physics,* 229, 3121-3133.

Sperry, J.M. and Peirce, J.J., (1995), A model for estimating the hydraulic conductivity of granular material based on grain shape, grain size and porosity, *Groundwater,* 33, (6), 89-898.

Takada, H., Abe, S., Tamatsu, Y., Mitarashi, S., Saka, H. and Ide, Y., (2006), Three-dimensional bone microstructures of the mandibular angle using micro-CT and finite element analysis: relationship between partially impacted mandibular third molars and angle fractures, *Dental Traumatology,* 22, 18-24.

Taylor, C. and Hood, P., (1973), A numerical solution of the Navier-Stokes equations using the finite element technique, *Computers & Fluids,* Vol. 1, pp. 73-100.

Turner, M., Clough, R.W., Martin, H.C. and Topp, L.J., (1956), Stiffness and deflection analysis of complex structures, *Journal of Aeronautical Science,* 23, (9), 805-823.

Ulrich, D., van Rietbergen, B., Laib, A. and Rüegsegger, P., (1999), The ability of three-dimensional structural indices to reflect mechanical aspects of trabecular bone, *Bone,* 25, (1), 55-60.

Van Brakel, J and Heertjes, P.M., (1974), Analysis of diffusion in macroporous media in terms of porosity, a tortuosity and a constrictivity factor, *Journal of Heat Mass Transfer,* 17, 1093-1103.

Vervoort, R.W. and Cattle, S.R., (2003), Linking hydraulic conductivity and tortuosity parameters to pore space geometry and pore-size distribution, *Journal of Hydrology,* 272, 36-49.

Vogel, H.J., (1997), Morphological determination of pore connectivity as a function of pore size using serial section, *European Journal of Soil Science,* 48, 365-377.

Voss, C.I., (1984), A finite-element simulation model for saturated-unsaturated, fluid-density-dependent ground-water flow with energy transport or chemically- reactive single-species solute transport prepared in cooperation with U.S. Air Force Engineering and Services Center. U.S. Dept. of the Interior, Geological Survey, U.S. Geological Survey, Open-File Services Section, Western Distribution Branch in Reston, Va, Denver, Colorado.

Wang, W.Y., Ayral, S., Castellana, F.S. and Gryte, C.C., (1984), Reconstruction of oil saturation distribution histories during immiscible liquid-liquid displacement by computer-assisted tomography, *AIChE Journal*, 30, (4), 642-646.

Warner, G.S, Nieber, J.L., Moore, I.D. and Geise, R.A., (1989), Characterizing macropores in soil by computed tomography, *Soil Science Society of America Journal*, 53, 653-660.

Weissberg, H.L., (1963), Effective diffusion coefficient in porous media, Flow Research Laboratory, Oak Rdige, Tennessee, Defense Documentation Centre.

Wellington, S.L. and Vinegar, H.J., (1987), X-ray computerized tomography, *Journal of Petroleum Technology*, 39, 885–898.

Wheeler, A., (1955), Reaction rates and slsectivity in catalyst pores, In *Catalysis*, Ed. Emmett, P.H., Vol. 2, Reinhold, New York.

Winsauer, W.O., Shearin, H., Masson, P. and Williams, M., (1952), Resistivity of brine-saturated sands in relation to pore geometry, *Bulletin of the American Association of Petroleum Geologists*, 36, (2), 253-277.

Withjack, E.M., (1988), Computerised tomography for rock property determination and fluid flow visualization, *SPE Formation Evaluation*, 3, (4), 696–704.

Zienkiewicz, O.C., and Cheung, Y.K. , (1965) , Finite Elements in the Solution of Field Problems, *The Engineer*, September, 507-510.